

AD-A017 612

SATELLITE IMAGE QUALITY SIMULATION STUDY

Bruce M. Boyce, et al

Perkin-Elmer Corporation

Prepared for:

Defense Advanced Research Projects Agency  
Rome Air Development Center

August 1975

DISTRIBUTED BY:

**NTIS**

National Technical Information Service  
U. S. DEPARTMENT OF COMMERCE

332069

RADC-TR-75-214  
Final Technical Report  
August 1975

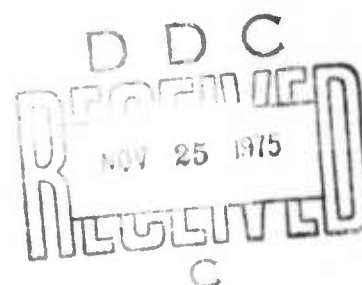


SATELLITE IMAGE QUALITY SIMULATION STUDY

The Perkin-Elmer Corporation

Sponsored by  
Defense Advanced Research Projects Agency  
ARPA Order No. 2646

Approved for public release;  
distribution unlimited.



The views and conclusions contained in this document are those of the authors and should not be interpreted as necessarily representing the official policies, either expressed or implied, of the Defense Advanced Research Projects Agency or the U. S. Government.

Rome Air Development Center  
Air Force Systems Command  
Griffiss Air Force Base, New York 13441

Reproduced by  
NATIONAL TECHNICAL  
INFORMATION SERVICE  
U S Department of Commerce  
Springfield VA 22151

ADA017612

This report has been reviewed by the RADC Information Office (OI) and is releasable to the National Technical Information Service (NTIS). At NTIS it will be releasable to the general public including foreign nations.

This report has been reviewed and is approved for publication.

APPROVED:

*Edward C. Mahen, Jr.*  
EDWARD C. MAHEN, Jr.  
CAPT, USAF  
Project Engineer

ACCESSION for	
NTIS	Write Section <input checked="" type="checkbox"/>
DDC	Buff Section <input type="checkbox"/>
UNANNOUNCED	<input type="checkbox"/>
JUSTIFICATION	<input type="checkbox"/>
BY _____	
DISTRIBUTION/AVAILABILITY	
Dist.	AVAIL. DATE
A	

Do not return this copy. Retain or destroy.

SATELLITE IMAGE QUALITY SIMULATION STUDY

Bruce M. Boyce  
Bob J. Knoll

Contractor: The Perkin-Elmer Corporation  
Contract Number: F30602-74-C-0209  
Effective Date of Contract: 1 April 1974  
Contract Expiration Date: 31 March 1975  
Amount of Contract: \$50,000.00  
Program Code Number: 5E20  
Period of work covered: Apr 74 - Mar 75

Principal Investigator: Bruce M. Boyce  
Phone: 203 762-6879

Project Engineer: Capt Edward C. Mahen, Jr.  
Phone: 315 330-3145

Approved for public release;  
distribution unlimited.

This research was supported by the Defense  
Advanced Research Projects Agency of the  
Department of Defense and was monitored by  
Capt Edward C. Mahen, Jr., RADC (OCSE),  
Griffiss AFB NY 13441.



UNCLASSIFIED

SECURITY CLASSIFICATION OF THIS PAGE (When Date Entered)

REPORT DOCUMENTATION PAGE		READ INSTRUCTIONS BEFORE COMPLETING FORM
1. REPORT NUMBER RADC-TR-75-214	2. GOVT ACCESSION NO.	3. RECIPIENT'S CATALOG NUMBER
4. TITLE (and Subtitle) SATELLITE IMAGE QUALITY SIMULATION STUDY	5. TYPE OF REPORT & PERIOD COVERED Final Technical Report April 1974 - March 1975	
7. AUTHOR(s) Bruce M. Boyce Bob J. Knoll		6. PERFORMING ORG. REPORT NUMBER 12471
9. PERFORMING ORGANIZATION NAME AND ADDRESS The Perkin-Elmer Corporation Norwalk CT 06856		8. CONTRACT OR GRANT NUMBER(s) F30602-74-C-0209
11. CONTROLLING OFFICE NAME AND ADDRESS Defense Advanced Research Projects Agency 1400 Wilson Blvd Arlington VA 22209		10. PROGRAM ELEMENT, PROJECT, TASK AREA & WORK UNIT NUMBERS 62301E 26460404
14. MONITORING AGENCY NAME & ADDRESS (if different from Controlling Office) Rome Air Development Center (OCSE) Griffiss AFB NY 13441		12. REPORT DATE August 1975
		13. NUMBER OF PAGES 128
		15. SECURITY CLASS. (of this report) UNCLASSIFIED
		15a. DECLASSIFICATION/DOWNGRADING SCHEDULE N/A
16. DISTRIBUTION STATEMENT (of this Report) Approved for public release; distribution unlimited.		
17. DISTRIBUTION STATEMENT (of the abstract entered in Block 20, if different from Report) Same		
18. SUPPLEMENTARY NOTES RADC Project Engineer: Capt Edward C. Mahen, Jr.		
19. KEY WORDS (Continue on reverse side if necessary and identify by block number) Image Processing Atmospheric Simulation Image Analysis		
20. ABSTRACT (Continue on reverse side if necessary and identify by block number) The purpose of the Satellite Image Quality Simulation was to develop a quantitative model for the relationship between the subjective quality of images of satellites obtained through a turbulent atmosphere from large ground based telescopes, and quantitative measures of the optical transfer function and noise characteristics of the image formation process. To determine this relationship, a series of images of satellites was generated in the study, in which the effects of various OTF and noise degradations were simulated. The (Cont'd)		

DD FORM 1473

1 JAN 73

EDITION OF 1 NOV 65 IS OBSOLETE

ia

UNCLASSIFIED

SECURITY CLASSIFICATION OF THIS PAGE (When Date Entered)

UNCLASSIFIED

SECURITY CLASSIFICATION OF THIS PAGE(When Data Entered)

images were viewed by a group of human observers, who were asked to estimate the subjective quality of the images, relative to a set of reference images of the same satellite having known resolution characteristics. The results of these viewing and interpretation experiments were then compared to the predictions of several image quality models; one model was found to produce a very good fit to the observed data.

UNCLASSIFIED

SECURITY CLASSIFICATION OF THIS PAGE(When Data Entered)

## TABLE OF CONTENTS

<u>Section</u>	<u>Title</u>	<u>Page</u>
I	INTRODUCTION	1
	1.1 Purpose	1
	1.2 Summary of Experiments	2
II	IMAGE SIMULATION	5
	2.1 Image Generation	5
	2.2 Optical Transfer Function Simulation	6
	2.3 Noise Simulation	22
	2.4 Post-Detection Compensation Simulation	30
III	VIEWING AND INTERPRETATION EXPERIMENTS	39
	3.1 Viewing and Interpretation Experiment Design	39
	3.2 Description of Results of the V and I Experiments	40
IV	ANALYSIS OF RESULTS	48
	4.1 Image Quality Criteria	48
	4.2 Experimental Data Fit to Simple Summary Measure Model	53
	4.3 Experimental Fit to Complete Summary Measure Model	58
	4.4 Use of Model for System Performance Analysis	66
V	CONCLUSIONS, RECOMMENDATIONS AND SUMMARY	68
	5.1 Conclusions Concerning Fit to Simple Model	68
	5.2 Conclusions Concerning Fit to Complete Model	68
	5.3 Recommendations	69
	5.4 Summary	69
	REFERENCES	70
 <b>Appendices</b>		
A	Random Wavefront Generation Using Zernike Polynomials	71
B	Simulation Study Images	86
C	Set by Set Summary of Results of Fitting Simple Model to Simulation Study Images	99
D	Eye Transfer Function	110
E	Estimative Filter Results	112
	GLOSSARY	117

## LIST OF ILLUSTRATIONS

<u>Figure</u>	<u>Title</u>	<u>Page</u>
1	Summary of Experiments	4
2	Long Time Exposure and Short Time Exposure OTF's	8
3	Reference Set Image and OTF Examples	9
4	Optical Transfer Functions Generated From Random Wavefronts	15
5	Short Time Exposure Images and OTF Examples	17
6	Wavefront Autocorrelation Functions and Phase Structure Functions	19
7	Long Time Exposure Transfer Functions	20
8	Long Time Exposure Image and OTF Examples	21
9	Noise Simulation Examples	24
10	Set B. Poisson Noise for Various Diffraction-Limited Apertures	25
11	Set H. Gaussian Noise for Various Diffraction-Limited Apertures	26
12	Set C. Short Time Exposure Atmospheric OTF and Poisson Noise	27
13	Set I. Short Time Exposure Atmospheric OTF and Gaussian Noise	28
14	Set F. Long Time Exposure MTF and Poisson Noise	29
15	Short Time Exposure OTF and Post-Processing (Exact)	32
16	Set D. Short Time Exposure Atmospheric OTF and Poisson Noise and Post-Processing Restoration to Strehl Ratio $\cong 0.8$	33
17	Set K. Short Time Exposure Atmospheric OTF and Gaussian Noise and Post-Processing to Strehl Ratio = 0.80	34
18	Set G. Long Time Exposure MTF and Poisson Noise and Post-Processing Restoration to Strehl Ratio = 0.8	35
19	Short Time Exposure OTF and Post-Processing	37
20	Set J. Short Time Exposure Atmospheric OTF and Poisson Noise and Post-Processing Using Korff Model	38
21	Viewing and Interpretation Experiment	41
22	Cumulative Probability Distributions of Quality Estimates for Three Typical Images	42

LIST OF ILLUSTRATIONS (Continued)

<u>Figure</u>	<u>Title</u>	<u>Page</u>
23	Noiseless Images Fit to Simple Model	55
24	Poisson Noise Images Fit to Simple Model	56
25	Gaussian Image Fit to Simple Model	57
26	Noiseless Images Fit to Full Model	60
27	Gaussian Noise Images Fit to Full Model	64
28	Poisson Noise Images Fit to Full Model	65
29	Isoquality Contours for an Object of Arbitrary Brightness	67

## SECTION I

### INTRODUCTION

This document represents the final report of the Satellite Image Quality Simulation Study, performed for Rome Air Development Center under Contract No. F30602-74-C-0209.

#### 1.1 PURPOSE

The purpose of the study was to develop a quantitative model for the relationship between the quality of images of satellites, obtained through a turbulent atmosphere from large ground-based telescopes, as perceived by human observers, and quantitative measures of the optical transfer function (OTF) and noise characteristics of the image formation process. To determine this relationship, a series of images of satellites was generated in which the effects of various OTF and noise degradations were simulated. These simulations were produced by first digitizing a high-resolution undergraded photograph of a satellite, simulating noise and OTF degradations in a digital computer, and then reconstructing the degraded images on a high-quality image playback device.

The images were then viewed by a group of human observers, who were asked to compare the degraded satellite images, one at a time, to a set of reference images of the same satellite having known resolution characteristics; after each simulated image was viewed by the group of observers, the relative quality of that image (relative to the reference set) was statistically determined by computing the average quality estimate from all observations.

The reference set consisted of a series of images in which the diffraction effects of various aperture diameters ranging from 60 inches to 4 inches were simulated. The observed quality of the simulations, as determined by the observers, is expressed in terms of the equivalent aperture diameter of the member of the reference set to which the observed image was equated.

The results of these viewing and interpretation (V and I) experiments were then compared to the predictions of several image quality models, and the model that produced the best fit to the observed data was selected.

## 1.2 SUMMARY OF EXPERIMENTS

The main goal of the program was to generate images for the purpose of fitting the results to a model, and not to simulate the output of any specific hardware system; therefore, the images were generated with a wide range of noise and OTF degradations, solely to provide as large a base of images as possible. However, the ultimate goal of the Teal Blue Program was kept in mind - i.e., the fabrication of a Compensated Imaging System in which both pre-compensation of the wavefront is performed before the images are recorded, and post-compensation is performed on the images after they are recorded.

With this operational concept in mind, the noise mechanisms and the OTF degradations selected for the simulations were designed to be the generic types of degradations that a compensated imaging system might suffer. For the noise mechanism, both multiplicative noise and additive noise were simulated; for the OTF degradations, two types of transfer functions were generated, one for short time exposure conditions, the other for long time exposure conditions. The relative strengths of the noise and the OTF degradations were varied, and the operation of two types of post-processing restoration operations were also included in the simulations. The first type of restoration filter that was simulated assumed complete knowledge of the degrading atmospheric OTF; for the case of short time exposure conditions, this represents a situation that is probably unachievable in the real world, but it is useful in placing an upper bound on the ability of post-compensation to perform its function, in addition to providing images against which various image quality models can be matched.

The second type of post-compensation processing that was simulated was the use of a post-compensation operator that represents only partial knowledge of the degradation transfer function; this filter was derived on only a statistical knowledge of the degrading OTF, and assumed that the degrading OTF was a smooth transfer function with no phase component. Thus, the post-

compensated images produced by this filter contained the effects of uncorrected modulus and phase errors in the OTF.

Figure 1 illustrates the various combinations of the degradations mentioned above that were used to generate the simulations; Table 1 lists the number of images generated during the study. A total of 121 images were generated and used in the study.

TABLE 1. SUMMARY OF EXPERIMENTS

<u>Set</u>	<u>Experiment</u>	<u>No. of Images</u>
A	Various Diffraction-Limited Apertures	15
B	Diffraction-Limited Apertures and Poisson Noise	12
H	Diffraction-Limited Apertures and Gaussian Noise	12
C	Short Time Exposure OTF and Poisson Noise	24
I	Short Time Exposure OTF and Gaussian Noise	9
D	Short Time Exposure OTF and Poisson Noise and Post-Processing (Exact)	9
K	Short Time Exposure OTF and Gaussian Noise and Post-Processing (Exact)	9
J	Short Time Exposure OTF and Poisson Noise and Post-Processing (Partial)	9
F	Long Time Exposure OTF and Poisson Noise	16
G	Long Time Exposure OTF and Poisson Noise and Post-Processing (Exact)	6



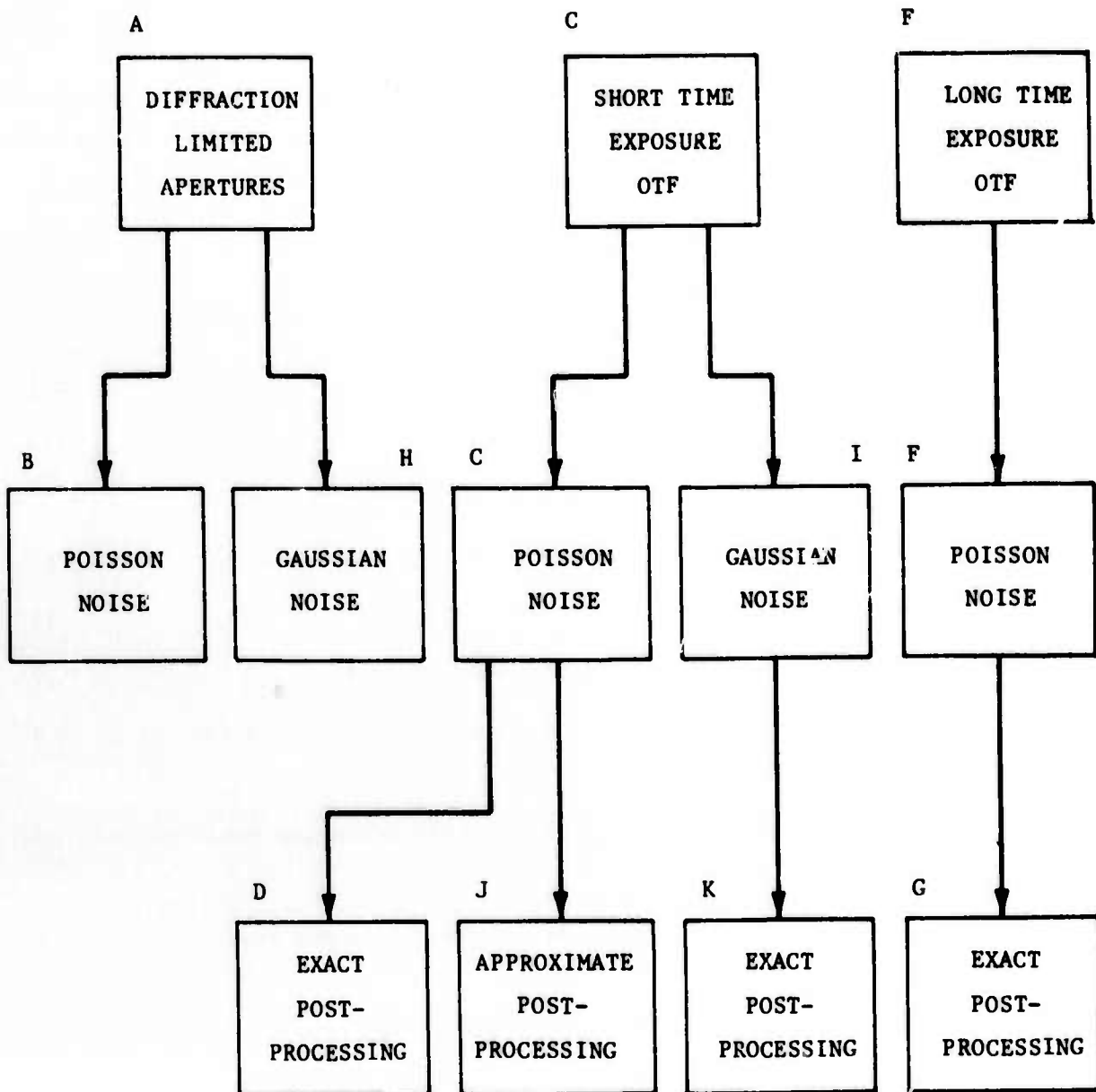


Figure 1. Summary of Experiments

## SECTION II

### IMAGE SIMULATION

In this section, the operations performed in the generation of the images used to perform the viewing and interpretation experiments will be discussed.

#### 2.1 IMAGE GENERATION

The source of all of the images generated during the study was a photograph of a model of the P72-2 satellite that was taken in a solar simulator; the model was produced by Rockwell International Corporation, under Contract No. F30602-74-C-011.

The original negative of the satellite model was used to produce a large-format positive transparency suitable for scanning on Perkin-Elmer's Line Scan Image Generator (LSIG), which was used to digitize the image.

##### 2.1.1 Scanning Parameters

The positive transparency was scanned at a spatial rate that corresponded to the sampling of a 6.5-arc-second satellite at the Nyquist rate for a 60-inch (1.524 meter) telescope operating at a wavelength of 0.5 micrometer. The Nyquist angular sampling frequency  $\Omega_s$  is given by

$$\Omega_s = \frac{2D}{\lambda} \quad (\text{samples/radian}) \quad (1)$$

which corresponds to an angular subtense for each image picture element (pixel) of

$$\theta_s = \frac{1}{\Omega_s} = \frac{\lambda}{2D} \quad (\text{radians/sample}) \quad (2)$$

For the parameters listed above, each pixel subtends  $1.64 \times 10^{-7}$  radians, or 0.034 arc-second. For a 6.5-arc-second object, this corresponds to a total number of 191 pixels across the large dimension of the object. As a result, all of the simulations generated for the study consisted of 256 x 256 images.

### 2.1.2 Intensity Linearization of the Digitized Image

Because of the various nonlinear properties of the two film steps (the exposure and development of the original negative and the positive transparency) and the digitization operation, it was necessary to linearize the digitized information so that the digital values of the sampled image were related in a linear fashion to the original reflectivity of the object itself. Fortunately, the original negative contained an image of a reflective target consisting of 16 chips of known reflectivities. By carrying the image of the test chips through all of the steps (film and digitization), it was a simple matter to determine the net nonlinearity of the combination of the film and digitization operations, and correct for these nonlinearities by digitally implementing a look-up table in the computer that effectively removed the nonlinearities. The same operation was also used to optimally scale the range of digital values so that the output images would use the full available dynamic range of the photographic material used to produce the images that were subsequently used for the viewing and interpretation experiments.

To further assure consistent quality for the images to be used in the experiments, a digital step tablet was played back with each of the images generated. This digital step tablet was used by the photo technician as a standard to determine the optimum exposure for each of the negatives produced on the LSIG in the image playback mode. Thus, the problem of inconsistent photographic processing introducing errors into the experiments was reduced to a minimum.

### 2.2 OPTICAL TRANSFER FUNCTION SIMULATION

For the study, images formed through three types of optical transfer functions were generated; diffraction-limited apertures of various diameters, short time exposure transfer functions, and long time exposure transfer functions. The purpose of simulating the latter two types of transfer functions stems from the desire to simulate different types of transfer functions for the purpose of testing image quality models over widely differing conditions. These two types most likely represent extremes in the kinds of transfer functions to be encountered by a Compensated Imaging System.

Short time exposure images are characterized by the condition that the exposure time for the image is short with respect to the velocity of propagation of the turbulence across the aperture of the system. For this case, the turbulence is essentially "frozen" during the exposure time, and the resulting complex optical transfer function will in general have a significant phase component, and the modulus will be a non-monotonic function of spatial frequency and will have significant irregularities.

If, on the other hand, the exposure time is long enough to permit a significant amount of averaging of the atmospheric turbulence, then the resultant optical transfer function will have a small phase component, and the modulus of the transfer function will be a smooth monotonically decreasing function, with a lower value for the modulus at all frequencies because of the averaging process.

A comparison of these two cases for the condition in which there is a significant amount of wavefront error reveals that the short time exposure image is harder to process from the standpoint of restoration, since knowledge of the shape of the complex OTF at the instant that the image was obtained is needed. On the other hand, the long time exposure image presents a simpler restoration problem, as it will require only a relatively smooth, real (non-complex) frequency domain filter whose shape can be predicted statistically. Figure 2 contains examples of these two types of transfer functions, for two levels of mean square wavefront error. Both of the top transfer functions have Strehl ratios of 0.03, while both bottom transfer functions have Strehl ratios of 0.3. These transfer functions, whose derivations are discussed in the following paragraphs, illustrate the differences between the two types of transfer functions. It should also be noted that the distinction becomes less distinct as the overall system quality improves.

### 2.2.1 Reference Set Generation

The reference set was generated using a fast Fourier transform (FFT) algorithm, for the series of 15 aperture diameters listed in Table 2. Three of the images and optical transfer functions are shown in Figure 3 and nine of the corresponding images are shown in Figure B-1 in Appendix B. For the images in Figure B-1 and all subsequent figures showing images, the three-digit

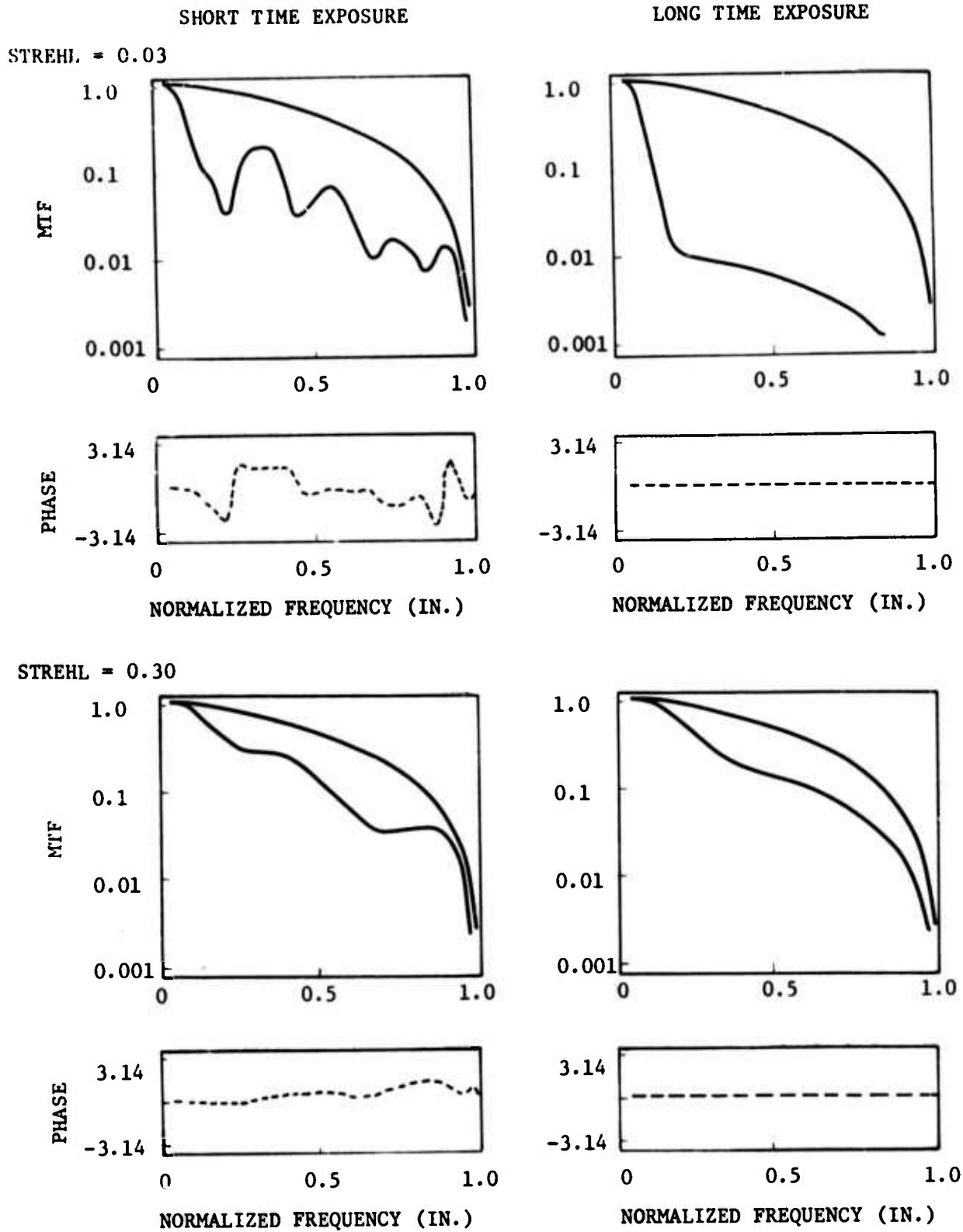
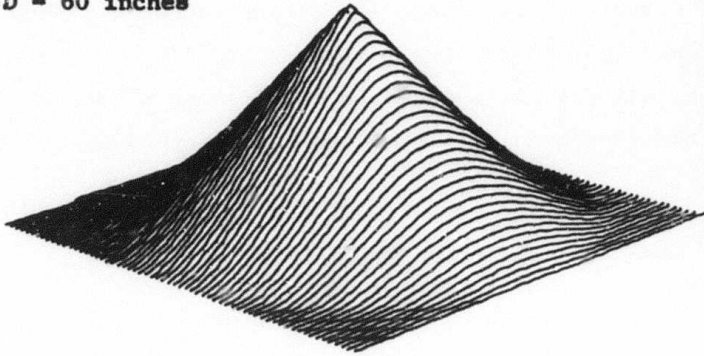


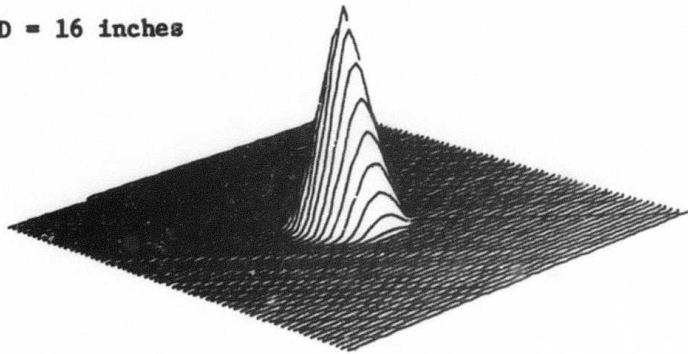
Figure 2. Long Time Exposure and Short Time Exposure OTF's

D = 60 inches



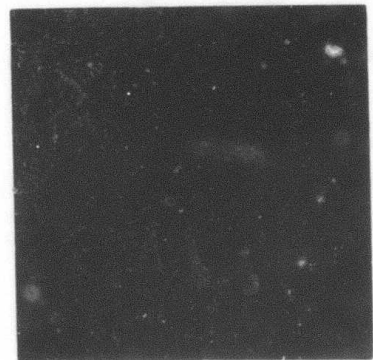
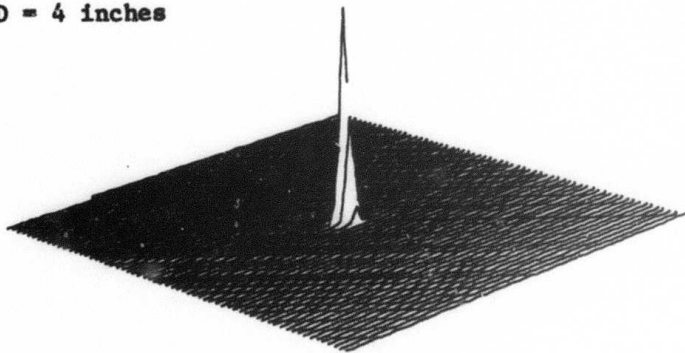
015

D = 16 inches



026

D = 4 inches



031

Figure 3. Reference Set Image and OTF Examples

number below the right-hand corner of each image is a frame number for the image, and is used to reference that image in all figures and tables contained in this report. In addition, all OTF plots shown in this report have the same scale, and have as the maximum frequency displayed the cutoff frequency of a 60-inch aperture.

TABLE 2. REFERENCE SET APERTURE DIAMETERS

<u>Image Number</u>	<u>Aperture Diameter (Inches)</u>	<u>Aperture Diameter (Meters)</u>
015	60	1.52
018	54	1.37
019	48	1.22
020	42	1.07
021	36	0.91
022	32	0.81
023	28	0.71
024	24	0.61
025	20	0.51
026	16	0.41
027	12	0.30
028	10	0.25
029	8	0.20
030	6	0.15
031	4	0.10

In the generation of the reference set and all other images, one additional operation was performed to compensate for the specifics of sampling, filtering, and reconstructing operation. This operation was a reading and writing spot transfer function compensation, in which the Fourier transform of the sampled image was divided by the transform of the combination of the reading and writing spots used to sample and reconstruct the images. For the object images, this reading and writing spot transfer function compensation effectively eliminates the reading and writing spots as sources of modulation transfer function (MTF) degradation.



### 2.2.2 Generation of Short Time Exposure Images

For the generation of the short time exposure transfer functions, random wavefronts were generated whose phase amplitude variations exhibited Kolmogoroff statistics, given by a power spectrum of the form

$$W_{\phi}(k) = 0.023 r_0^{-5/3} k^{-11/3} \quad [\text{radians}^2 / (\text{cycle/meter})^2] \quad (3)$$

where

$$k = \sqrt{k_x^2 + k_y^2}$$

$r_0$  = coherence length of the atmosphere

These wavefronts were then Fourier transformed, to obtain the optical transfer functions (OTF) that were subsequently used to generate the images.

An alternative description of a wavefront exhibiting Kolmogoroff statistics is found by specifying the phase structure function, defined as

$$D(r) = \langle |\phi(r' + r) - \phi(r')|^2 \rangle \quad (4)$$

where

$$r = \sqrt{u^2 + v^2}$$

$\phi(r')$  = phase of wavefront at point  $r'$

$r$  = spatial separation between two points in wavefront

This wave structure function can be written for the case of Kolmogoroff turbulence as

$$D(r) = 6.88 \left( \frac{r}{r_0} \right)^{5/3} \quad (5)$$

where  $r_0$  describes the strength of the atmospheric turbulence. Typical values of the coherence length for typical seeing conditions are in the range of 4 inches (10 centimeters).



2.2.2.1 Wavefront Simulation - There are several methods available for the simulation of wavefronts having phase perturbations exhibiting Kolmogoroff statistics: the method of generating the wavefronts used in this study involves describing the wavefront as a Zernike polynomial expansion given by

$$\phi(u,v) = \sum_{n=1}^{\infty} A_n Z_n(u,v) \quad (6)$$

where

$\phi(u,v)$  = wavefront perturbation (waves)

$Z_n(u,v)$  = nth orthonormal Zernike polynomial

$A_n$  = coefficient of nth Zernike polynomial

Note that any given wavefront is described by the set  $\{A_n\}$  and that for Kolmogoroff turbulence,

$$\langle A_n \rangle = 0.0 \quad (7)$$

and the value of the mean square quantity,  $\langle A_n^2 \rangle$ , can be computed from the Kolmogoroff power spectrum and the Fourier transforms of the Zernike polynomials.

Wavefront simulation was performed by using a random number generator to select a set of coefficients  $\{A_n\}$ , whose mean and variance satisfy the conditions stated above. The advantage of this method over the generation of a wavefront by Fourier series representation lies in the fact that each of the terms in the expansion is explicitly accounted for; there are no errors in the generation of the low spatial frequency terms (low order errors, such as wavefront tilt) resulting from finite sampling in the frequency domain. Appendix A contains a detailed discussion of this wavefront generation method.

Table 3, below, lists expected values of rms wavefront error for various values of coherence length  $r_0$ , for two cases of interest - short and long time exposures. Note that the long time exposure case includes the wavefront error due to the tilt component, while the short time exposure case does not. (In the case of a short time exposure, tilt causes only a displacement of the object, which does not degrade its quality.)

TABLE 3. WAVEFRONT ERRORS FOR 60-INCH APERTURE

r <sub>o</sub> Coherence Length (Meters)	Wavefront Error			
	Short Time Exposure		Long Time Exposure	
	Mean Square Error (Rad <sup>2</sup> )	rms Waves	Mean Square Error (Rad <sup>2</sup> )	rms Waves
1.50	0.13	0.057	1.00	0.16
0.80	0.39	0.099	3.00	0.28
0.40	1.25	0.180	9.61	0.49
0.25	2.74	0.260	21.06	0.73
0.15	6.43	0.40	49.42	1.12
0.10	12.67	0.57	97.39	1.57

2.2.2.2 Optical Transfer Function Generation - Both Fried<sup>1</sup> and Hufnagel<sup>2</sup> predict that the expected value of the short time exposure transfer function T<sub>se</sub>(k) for viewing through a turbulent medium exhibiting Kolmogoroff statistics is given by

$$\langle T_{se}(k) \rangle = T_o(k) e^{-3.44 \left( \frac{\lambda F k}{r_o} \right)^{5/3} \left[ 1 - \left( \frac{\lambda F k}{D_o} \right)^{1/3} \right]} \quad (8)$$

where

- $\langle \rangle$  = denotes an ensemble average
- T<sub>o</sub>(k) = diffraction-limited transfer function
- λ = wavelength
- F = focal length
- D<sub>o</sub> = aperture diameter
- r<sub>o</sub> = coherence diameter

<sup>1</sup>D.L. Fried, "Optical Resolution Through a Randomly Inhomogeneous Medium for Very Long and Very Short Exposures", J. Opt. Soc. Amer., Vol. 56, No. 11, 1372 (1966).

<sup>2</sup>R.E. Hufnagel, "On the Mean Short-Term Blur", Woods Hole Summer Study on Restoration of Atmospherically Degraded Images, Vol. 2, Appendix 4 (July 1966).

However, this MTF is not descriptive of the OTF of a single short time exposure OTF, since the process of performing the ensemble average involves finding the average magnitude  $\langle T(k) \rangle$  of a complex quantity (the OTF) whose phase angle is essentially a random quantity; thus, although the MTF may have a significant average value independent of the phase, the inclusion of the phase portion of the OTF in the averaging process performed in computing  $\langle T_{se}(k) \rangle$  will cause the function to drop to zero rapidly.

Korff<sup>3</sup> has predicted the expected value of the square of the absolute value of the short time exposure transfer function as

$$\langle |T_{se}(k)|^2 \rangle = \frac{T_o^2(k)}{(D_o/r_o)^2} \left[ 0.435 + \frac{0.278}{\left(\frac{D_o k}{r_o}\right)^{1/3}} \right] \quad \text{for } \frac{D_o k}{r_o} \gg 1 \quad (9)$$

where  $k$  = normalized spatial frequency

Since this quantity is computed by ignoring the phase portion of the OTF, it is this quantity that should correspond to the average modulus of simulated OTF's generated from random wavefronts exhibiting Kolmogoroff statistics.

To check the assumption stated above, a series of random wavefronts was generated for an  $r_o$  of 13 centimeters, and used to generate a series of optical transfer functions. Figure 4 illustrates values of the various generated OTF's, along with an evaluation of the Korff expression for the average short time exposure MTF. As shown, the agreement is quite good. This model will be used later for the purpose of deriving post-processing filters based on only a statistical estimate of the degrading transfer function.

### 2.2.3 Image Generation

Using the software described in Appendix A, a series of images containing the simulated effects of various amounts of atmospheric turbulence was generated for the five values of  $r_o$  listed in Table 4. Some of these transfer

<sup>3</sup>D. Korff, "Analysis of a Method for Obtaining Near-Diffraction Limited Information in the Presence of Atmospheric Turbulence", J. Opt. Soc. Amer., Vol. 63, No. 8, 971 (1973).

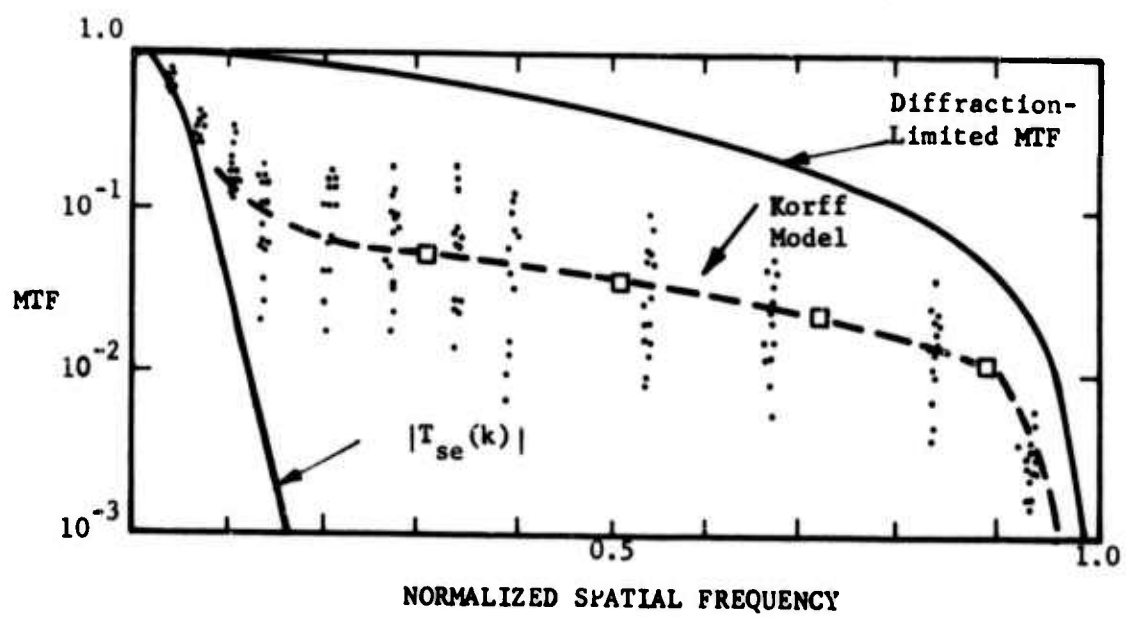


Figure 4. Optical Transfer Functions Generated From Random Wavefronts

transfer functions are shown in Figure 5. Paragraph 2.3 contains a discussion of the production of noisy images, in which various amounts of both Poisson and Gaussian noise are added to these atmospherically degraded images.

TABLE 4. SUMMARY OF NOISELESS SHORT TIME EXPOSURE IMAGES

<u>Image Number</u>	<u><math>r_o</math> (Meters)</u>	<u>Mean Square Wavefront Error (Rad<sup>2</sup>)</u>	<u>Strehl Ratio</u>
015	$\infty$	0.00	1.0000
052	0.80	0.39	0.6900
048	0.40	1.25	0.3400
044	0.25	2.74	0.1300
040	0.15	6.43	0.0320
036	0.10	12.67	0.0044

#### 2.2.4 Generation of Long Time Exposure Images

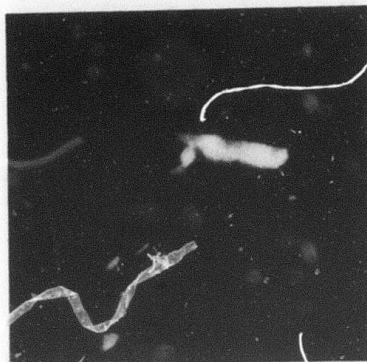
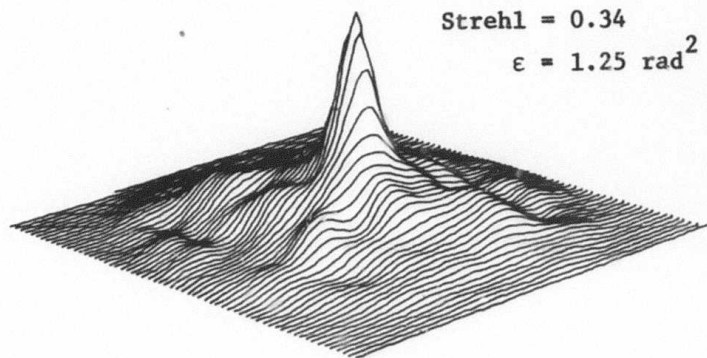
For the generation of long time exposure images, the assumption will be made that the images will be obtained through a pre-compensation system in which a significant amount of wavefront correction is performed before the image is recorded, with the emphasis on the removal of the low spatial frequency wavefront errors.

Huignagel and others have shown that the expected value of the long time exposure MTF, for no wavefront correction, is given by:

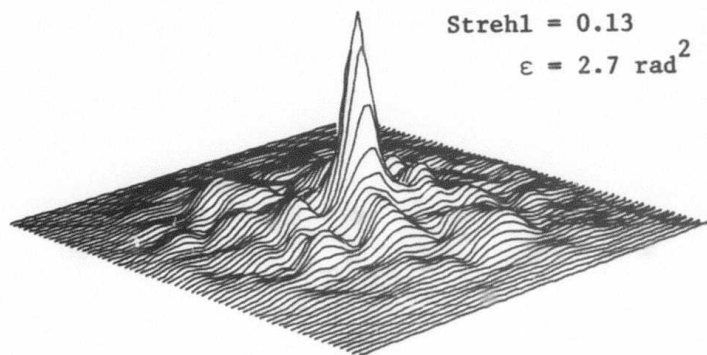
$$\langle T_{le}(k) \rangle = T_o(k) e^{-[C(o) - C(\lambda Fk)]} \quad (10)$$

where  $C(\lambda Fk) = C(r)$  and is the two-dimensional autocorrelation function of the wavefront deformations, in units of radians<sup>2</sup>. The phase structure function,  $D_\phi(r)$ , is given as

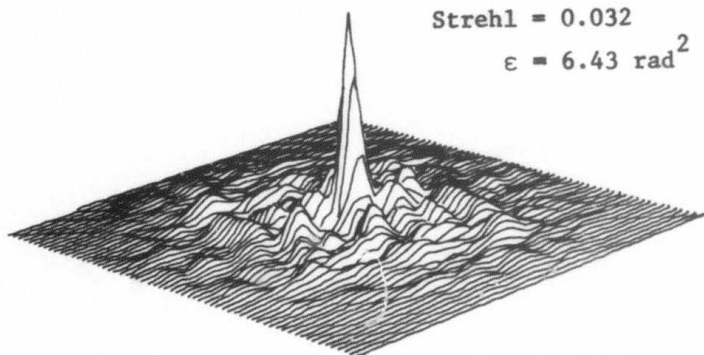
$$D_\phi(r) = \langle |\phi(r + r') - \phi(r)|^2 \rangle \quad (11)$$



048



044



040

Figure 5. Short Time Exposure Images and OTF Examples

Expanding Equation (11) yields

$$D_{\phi}(r) = 2[C(0) - C(r)] \quad (12)$$

Equation (10) becomes, upon substitution of Equations (5) and (12)

$$\langle T_{le}(k) \rangle = T_o(k) e^{-3.44 \left( \frac{(\lambda Fk)}{r_o} \right)^{5/3}} \quad (13)$$

For the case where a significant amount of wavefront correction has been performed such that the low spatial frequency components of the wavefront have been reduced, the autocorrelation function of the wavefront will have a lower value at  $\lambda Fk = 0$ , and will drop faster, resulting in a phase structure function that levels off at large values of  $\lambda Fk$  (see Figure 6). For this case, the long time transfer function becomes approximately

$$\langle T_{le}(k) \rangle \approx T_o(k) e^{-1/2D(\lambda Fk)} \approx T_o(k) e^{-C(o)} \quad (14)$$

where  $C(o)$  is the mean square uncorrected wavefront error.

Figure 7 illustrates a family of four long time exposure transfer functions, computed from Equation (14) for which an approximate shape was assumed for the spatial frequency region near the origin; Table 5 lists the noiseless images generated from these transfer functions; and Figure 8 illustrates three of the noiseless long time exposure images.

TABLE 5. SUMMARY OF LONG TIME EXPOSURE IMAGES

<u>Image Number</u>	<u>Mean Square Wavefront Error (Rad<sup>2</sup>)</u>	<u>Strehl Ratio</u>
089	0.39	0.838
090	1.20	0.391
091	2.74	0.109
092	4.36	0.031



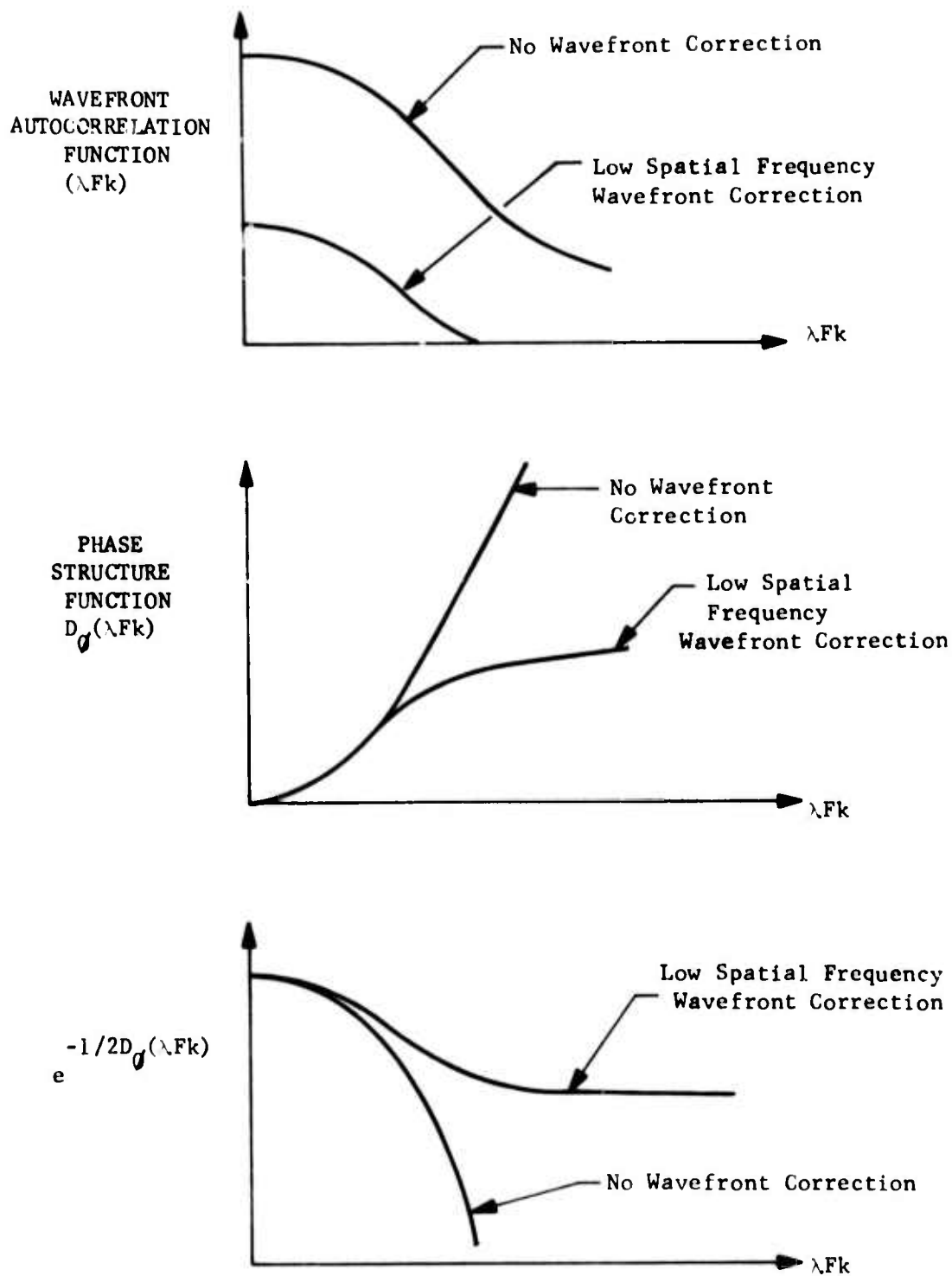


Figure 6. Wavefront Autocorrelation Functions and Phase Structure Functions



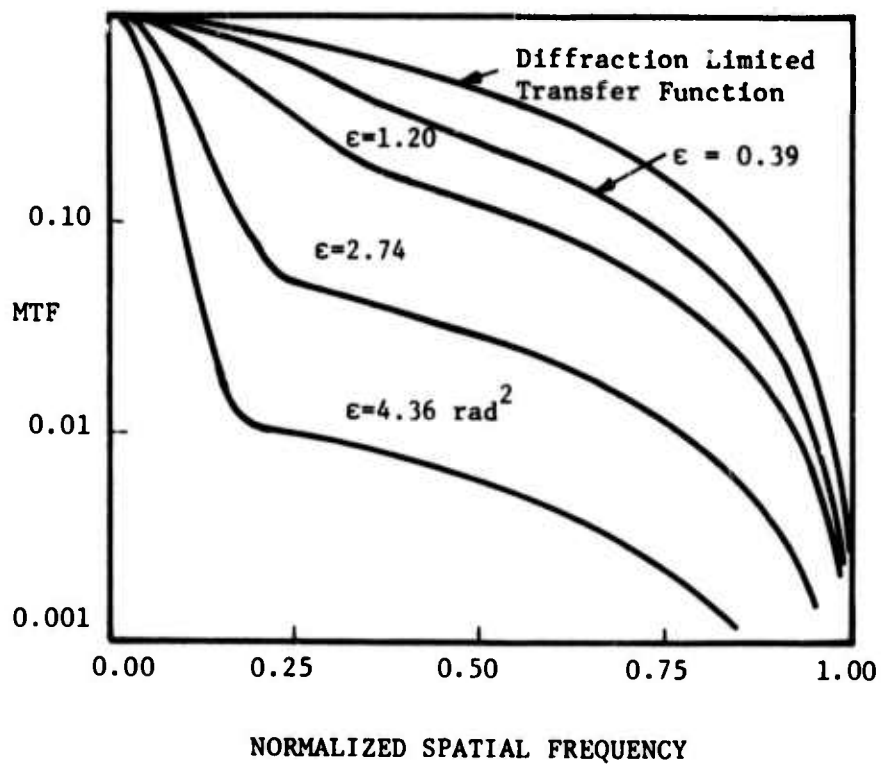
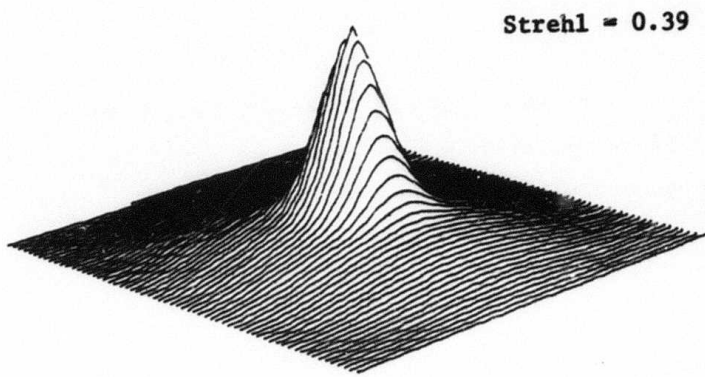
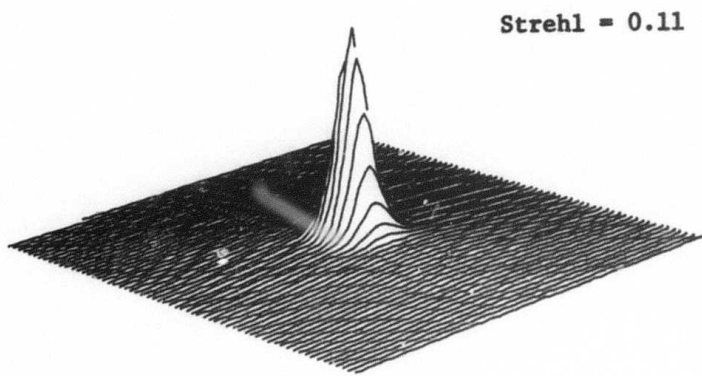


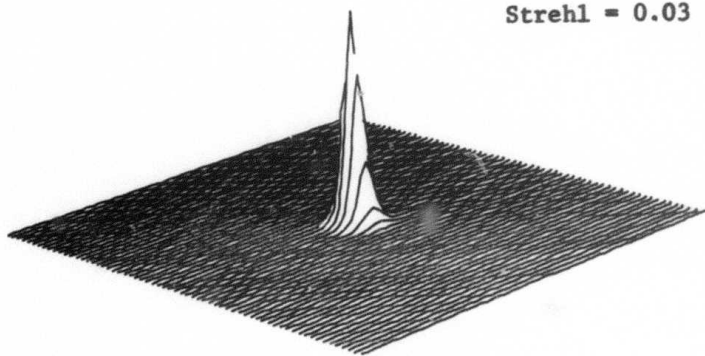
Figure 7. Long Time Exposure Transfer Functions



090



091



092

Figure 8. Long Time Exposure Image and OTF Examples

Note that a direct comparison of short and long time exposure images reveals that the short time exposure images differ from the long time exposure images by having much more fine structure visible, because of the generally higher modulus values and the presence of substantial phase in the OTF.

### 2.3 NOISE SIMULATION

The second important image quality degrading feature of the Compensated Imaging System to be simulated is image noise. There are two basic types of image noise that the Compensated Imaging System may be subject to - signal-dependent (shot) noise arising from the statistics of photon arrival rates, and additive noise. Both of these noise mechanisms have been simulated in the study, as described below.

#### 2.3.1 Poisson (Shot) Noise Simulation

In the image recording process, an image sampling operation is performed, resulting in a sampled image consisting of a series of digital numbers representing the number of photoelectrons collected from each image picture element (pixel) during an exposure (photoelectron integration time). The value of that sampled image data point may be written in terms of the reflectivity of the object and a photometric constant that lumps together all of the optical efficiency, collecting aperture, and object irradiance factors.

$$U_s(x) = A r_s(x) \quad (\text{photoelectrons}) \quad (15)$$

where

$U_s(x)$  = value of sampled image (photoelectrons)

$A$  = photoelectrons per pixel per unit object reflectivity

$r_s(x)$  = object reflectivity

The rms shot noise  $\sigma_n(x)$  resulting from the signal described in Equation (15) can be written as

$$\sigma_n(x) = \sqrt{U_s(x)} \quad n(x) \quad (\text{photoelectrons}) \quad (16)$$

where  $n(x)$  is a random variable exhibiting Poisson statistics, for which

$$\langle n(x) \rangle = 0.0 \quad (17a)$$

$$\langle |n(x)|^2 \rangle = 1.0 \quad (17b)$$

We may now express the rms noise in equivalent reflectivity units by using the constant A

$$\sigma_r(x) = \frac{\sigma_n(x)}{A} = \sqrt{\frac{r_s(x)}{A}} n(x) \quad (\text{reflectivity}) \quad (18)$$

Taking an average over the entire satellite yields

$$\bar{\sigma}_r = \sqrt{\frac{r_s}{A}} \quad (\text{reflectivity}) \quad (19)$$

For the simulation of Poisson noise, Equation (18) was used in conjunction with an algorithm that permits rapid generation of values of the Poisson random variable defined by  $n(x)$ .<sup>4</sup> Values of A used ranged from 16 photoelectrons per pixel per unit reflectivity to 2000 photoelectrons per unit reflectivity. This range of values of A resulted in a range of average rms reflectivity values from 0.0112 reflectivity unit to 0.125 reflectivity unit, based on an average reflectivity of 25 percent.

### 2.3.2 Poisson and Gaussian Noise Image Generation

Five sets of noisy images were generated for the study, as summarized in Figure 1. The first two sets (B and H), consisting of noise images obtained through diffraction-limited apertures of 60-, 48-, 32-, and 16-inch diameters, were generated to provide images against which various image quality models could be measured. The other three sets were generated to provide the type of noisy imagery that a Compensated Imaging System might be expected to produce, for the case of pre-compensation only (the case of post-compensation is discussed in paragraph 2.4). See Figure 9 for example.

Figures 10 through 14 illustrate the selection of the OTF and noise parameters for each of the simulations; the three-digit numbers in each of the rectangles refers to the frame number of that specific simulation.

<sup>4</sup>R.E. Hufnagel and E.L. Kerr, "A Simple Algorithm for Fast Real-Time Generation of Pseudorandom Poisson Integers with Rapidly Varying Means", Proc. IEEE, Vol. 57, No. 11, 2088 (1969)

POISSON  
NOISE

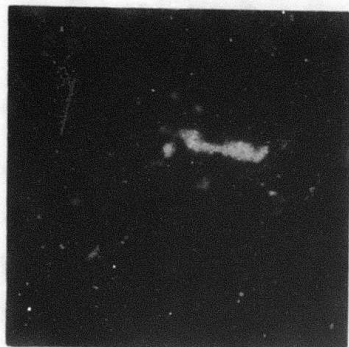


035

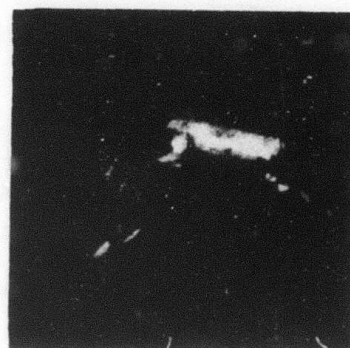


034

GAUSSIAN  
NOISE



115



116

$a = 80$

$\sigma_r = 0.056$

$a = 16$

$\sigma_r = 0.125$

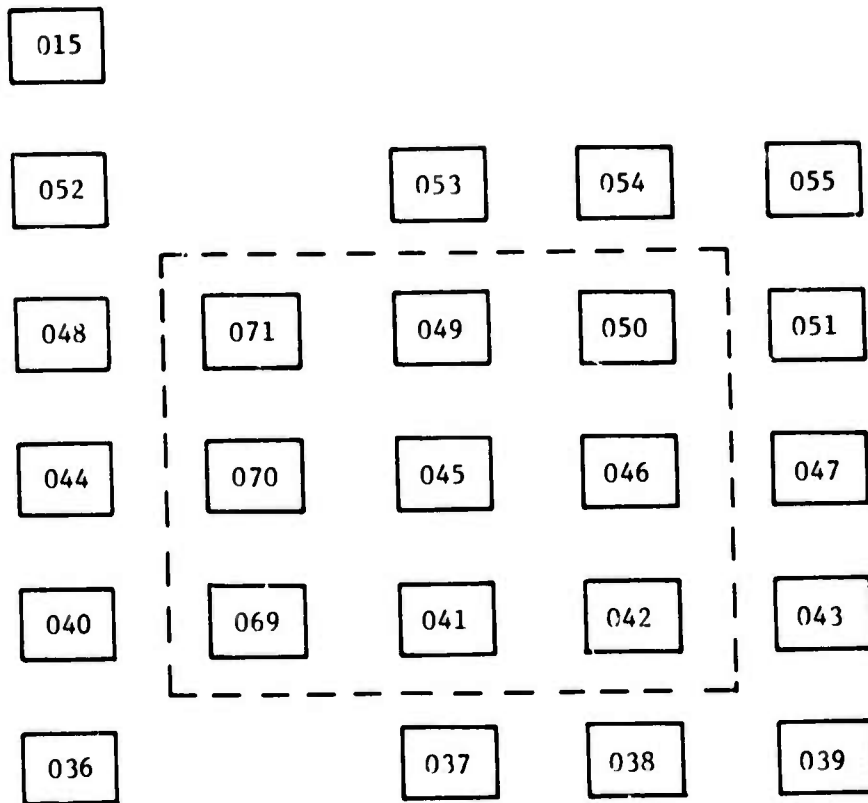
Figure 9. Noise Simulation Examples

60 INCHES	033	035	034
48 INCHES	059	060	061
32 INCHES	062	063	064
16 INCHES	065	066	067
$a$	= 400	80	16
$\sigma_r$	= 0.025	0.056	0.125

Figure 10. Set B. Poisson Noise for Various Diffraction-Limited Apertures

60 INCHES	114	115	116
48 INCHES	117	118	119
32 INCHES	120	121	122
16 INCHES	123	124	125
a	= 400	80	16
$\sigma_r$	= 0.025	0.056	0.125

Figure 11. Set H. Gaussian Noise for Various Diffraction-Limited Apertures



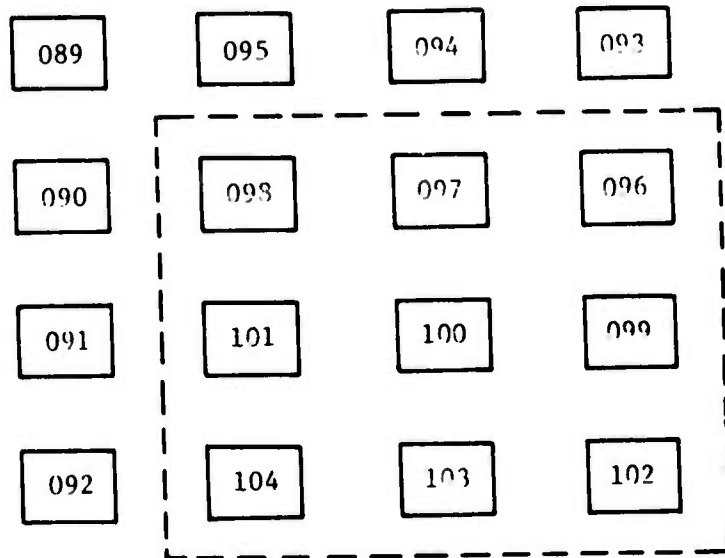
a	=	$\infty$	2000	400	80	16
$\sigma_r$	=	0.0	0.0112	0.025	0.056	0.125

Figure 12. Set C. Short Time Exposure Atmospheric OTF and Poisson Noise



$r_o = 0.40$	126	127	128
$r_o = 0.25$	129	130	131
$r_o = 0.15$	132	133	134
$a$	= 2000	400	80
$\sigma_r$	= 0.0112	0.025	0.056

Figure 13. Set I. Short Time Exposure Atmospheric OTF and Gaussian Noise



$a$	=	$\infty$	2000	400	80
$\sigma_r$	=	0.0	0.0112	0.025	0.056

Figure 14. Set F. Long Time Exposure MTF and Poisson Noise

Appendix B contains nine sample images from each of the five sets summarized in Figures 10 through 14.

## 2.4 POST-DETECTION COMPENSATION SIMULATION

One of the basic features of the Compensated Imaging System concept is the use of post-detection image processing to perform additional image restoration, after the pre-detection compensation adaptive optics has done as much as possible to correct the wavefront to that of a diffraction-limited system.

If image restoration is accepted as the prime goal of the system, then the post-detection compensation operation has as its goal the restoration of the system transfer function to that of a diffraction-limited aperture having the same aperture diameter as the system itself. Because of the presence of noise in the images being restored, the restoration goal may not yield the most desirable post-detection compensated image in all cases; however, this goal of restoring the transfer function is the most straightforward, and is likely to provide the basis for most of the operations to be performed on imagery having good signal-to-noise ratios in any operational system. In addition, for cases where the system is not noise limited, the results of such post-detection transfer function compensation will appear to be equal to images obtained from a diffraction-limited system, which is the basic goal of the system concept.

There are two considerations to be made in the simulation of the post-detection compensation function; first, what is the effect of imperfect knowledge of the degrading transfer function and second, what is the effect on the subjective quality of the changed spectrum of the image noise due to the effects of application of post-detection compensation, compared to the application of the same general level of compensation applied before image detection.

### 2.4.1 Exact Transfer Function Restoration

If the exact optical transfer function through which an image is obtained is known, the post-detection compensation operation can take the form of a direct inverse frequency domain filter, as described below, where the filter

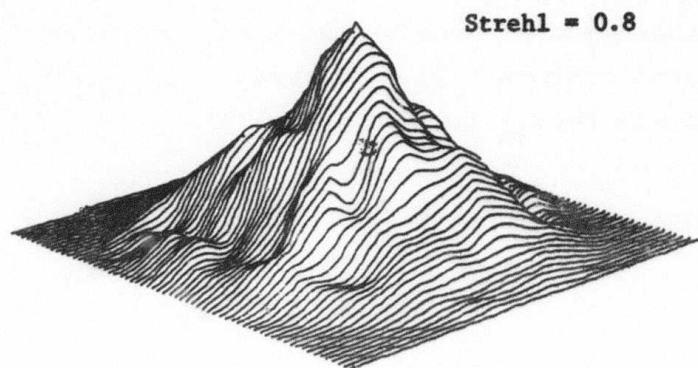
$F_e(k)$  is derived from the known degrading transfer function  $T_{kn}(k)$ , and the diffraction-limited transfer function  $T_{dl}(k)$ . (The values of  $E_{max}$  and  $\beta$  serve to avoid singularities in the  $T_{kn}$  function.)

$$F_e(k) = \begin{cases} 0 & T_{kn}(k) < \beta \\ \frac{T_{dl}(k)}{T_{kn}(k)} & \frac{T_{dl}(k)}{E_{max}} > T_{kn}(k) > \beta \\ E_{max} & T_{kn}(k) < \frac{T_{dl}(k)}{E_{max}} \end{cases} \quad (20)$$

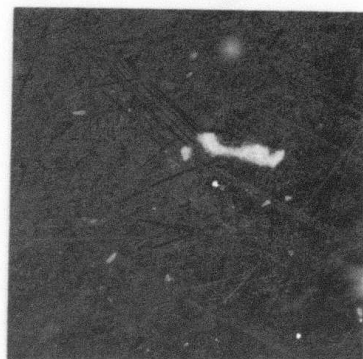
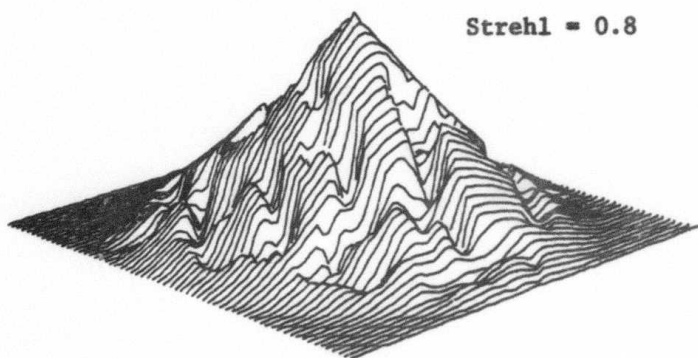
For this simple type of restoration operation, the parameter  $E_{max}$  can be varied to produce different post-processing Strehl ratios. For the images contained in sets D, K, and G, which represent the application of this type of restoration filter to the short and long term exposure image sets C, I, and F, the value of  $E_{max}$  for each of the post-detection filters was set to produce a Strehl ratio for the post-processed images of 0.8. Figure 15 illustrates the three post-processed transfer functions and corresponding images, for the post-detection compensation of the short time exposure images. The examples shown are the Poisson noise images. Figures 16 and 17 illustrate the combination of parameters for which the exact restoration filters illustrated in Figure 15 have been applied to the Poisson and Gaussian noise degraded short time exposure images; Figure 18 illustrates the parameters for the analogous operation applied to the long time exposure images, for the case of Poisson noise degradation.

#### 2.4.2 Approximate Transfer Function Restoration

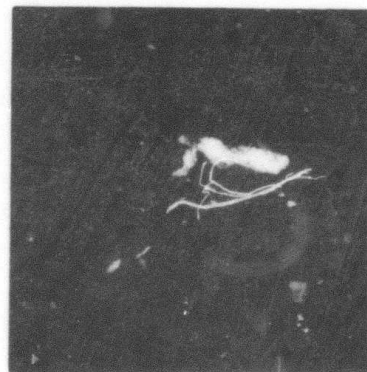
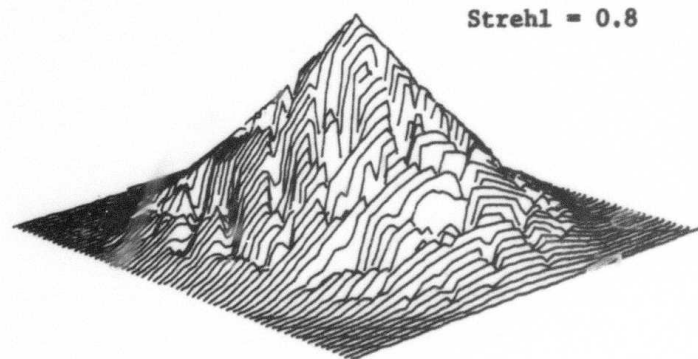
In addition to the exact restoration filter discussed above, a second type of restoration filter can be used, one based on a statistical knowledge of the transfer function, rather than on exact knowledge. The Korff formulation for the average modulus of a short time exposure transfer function was discussed above; if that formulation is used as the basis for deriving an inverse filter, as described below, the result of applying that filter to a short time exposure image will be a post-processing transfer function in which some residual modulus and phase error will remain



076



073



072

Figure 15. Short Time Exposure OTF and Post-Processing (Exact)

$r_o = 0.40$	076	081	082
$r_o = 0.25$	073	079	080
$r_o = 0.15$	072	077	078
$a$	= 2000	400	80
$\sigma_r$	= 0.0112	0.025	0.056

Figure 16. Set D. Short Time Exposure Atmospheric OTF and Poisson Noise and Post-Processing Restoration to Strehl Ratio  $\cong 0.8$

$r_o = 0.40$	144	145	146
$r_o = 0.25$	147	148	149
$r_o = 0.15$	150	151	152
$a$	= 2000	400	80
$\sigma_r$	= 0.0112	0.025	0.056

Figure 17. Set K. Short Time Exposure Atmospheric OTF and Gaussian Noise and Post-Processing to Strehl Ratio = 0.80

$r_o = 0.40$	107	106	105
$r_o = 0.25$	110	109	108
$r_o = 0.20$	113*	112*	111*
$a$	= 2000	400	80
$\sigma_r$	= 0.0112	0.025	0.056

\* Badly degraded - not V and I reduced

Figure 18. Set G. Long Time Exposure MTF and Poisson Noise and Post-Processing Restoration to Strehl Ratio = 0.8



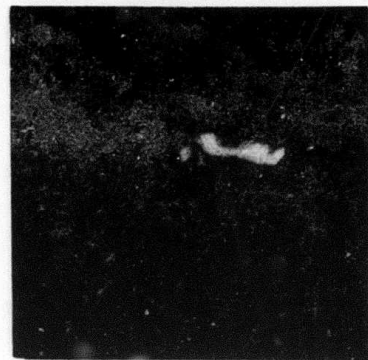
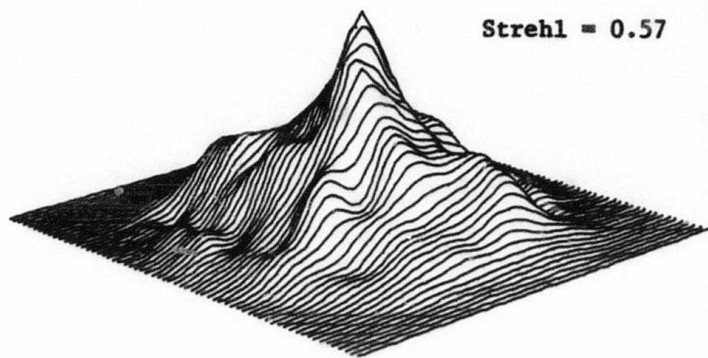
$$F_a(k) = \frac{T_{dl}(k)}{\sqrt{\langle |T_{se}(k)|^2 \rangle}} \quad (21)$$

See Figure 19 for three examples; Figure 20 summarizes the images generated. As shown in Table 6, which lists the pertinent parameters for all of the post-processed images, the application of the approximate filter results in Strehl ratios that fall considerably short of the Strehl ratio for the post-processed images processed using exact knowledge of the degrading transfer function.

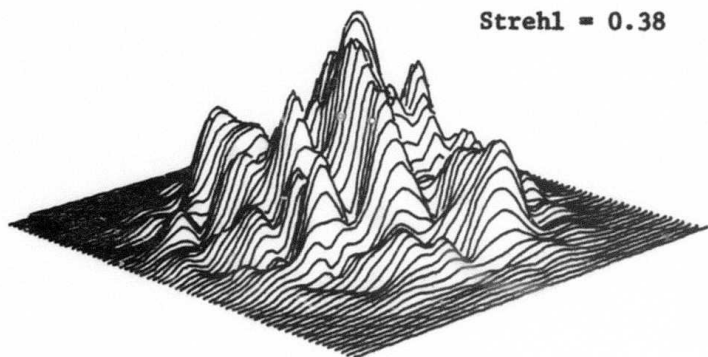
TABLE 6. SUMMARY OF POST-PROCESSED TRANSFER FUNCTION

Set	Image Numbers	Noise Type	OTF * Type	Filter Type	Post-Processing Strehl Ratio
D	076, 081, 082	P	Short Te	Exact	0.8
	073, 079, 080				0.8
	072, 077, 078				0.8
K	144, 145, 146	G	Short Te	Exact	0.8
	147, 148, 149				0.8
	150, 151, 152				0.8
G	107, 106, 105	P	Long Te	Exact	0.8
	110, 109, 108				0.8
	113, 112, 111				0.8
J	135, 138, 141	P	Short Te	Approx.	0.57
	136, 139, 142				0.38
	137, 140, 143				0.17

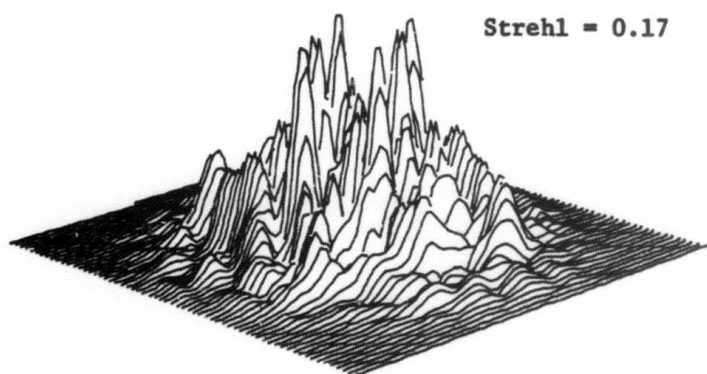
\* Te = Time exposure



135



136



137

Figure 19. Short Time Exposure OTF and Post-Processing (Approximate)

$r_o = 0.40$	135	138	141
$r_o = 0.25$	136	139	142
$r_o = 0.15$	137	140	143
$a$	= 2000	400	80
$\sigma_r$	= 0.0112	0.025	0.056

Figure 20. Set J. Short Time Exposure Atmospheric OTF and Poisson Noise and Post-Processing Using Korff Model

## SECTION III

### VIEWING AND INTERPRETATION EXPERIMENTS

In Section I, the main purpose of the study described in this report was stated to be a derivation of a mathematical model relating the subjective quality of satellite imagery, as determined by human observers, to various quantitative measures of system transfer function and noise characteristics. In this section, the determination of the subjective image quality of the images by human observers will be discussed.

#### 3.1 VIEWING AND INTERPRETATION EXPERIMENT DESIGN

The most direct method of determining the relationship between the subjective image quality and the degradations present in the satellite imagery is to perform viewing and interpretation experiments. In these experiments, a group of human observers is asked to rank each of the degraded images against a reference set of standard images having known resolution characteristics. If the observer decides that a degraded image is subjectively equal to one of the standard set, then the degraded image is said to have an image quality equal to the quality of the standard image to which it was equated (it is also permissible for the observer to rate an image between two members of the reference set). Previous studies have shown a high correlation between the subjective quality judgements of a group of observers, and the actual performance of professional photo-interpreters measured by the amount of quantitative information correctly recovered in a controlled experiment.<sup>5</sup>

For the experiments performed in this study, the resolution of the image, as determined by the average relative ranking of that image against the reference set, is expressed in terms of equivalent aperture diameter. Thus, an

---

<sup>5</sup>F. Scott, "The Search for a Summary Measure of Image Quality", Photo. Sc. & Eng., Vol 12, 154 (1968)

image that was generated as a noisy, atmospherically degraded image from a 60-inch-aperture system may well have the resolution, or equivalent quality, of a diffraction-limited image obtained from a 4-inch-aperture system. As will be seen in Section IV, these units for expressing image quality are compatible with several image quality measures of interest.

All of the simulations performed for atmospherically degraded transfer functions were generated for a 60-inch-aperture system; only sets A, B, and H contained images generated for apertures smaller than 60 inches.

### 3.2 DESCRIPTION OF RESULTS OF THE V AND I EXPERIMENTS

The 106 images produced for the study were separated into seven separate groups, and each group of images was viewed by an average of 13 observers. Each observer was asked to rank each of the images against the reference set of 15 images (see Figure 21).

For each image, the geometrical mean of the quality estimates was determined, along with the standard deviation factor for the set of estimates. The distribution of the estimates for any single image was found to be approximately a log normally distributed Gaussian random variable; therefore, the geometrical mean should give the truest estimate of the average perceived quality for each of the images. Figure 22 illustrates typical cumulative probability plots of the individual quality estimates for three of the images viewed.

Tables 7 through 9 list the resultant estimates of subjective image quality determined for each of the 106 images. Table 7 lists the perceived quality for each of the 10 short and long term exposure noiseless images; Table 8 lists the results for all of the Poisson noise images; and Table 9 lists the results for all of the Gaussian noise images. For the tables shown, the column headings have the following meaning:

IMAGE	-	image frame number
DIA	-	aperture diameter in inches

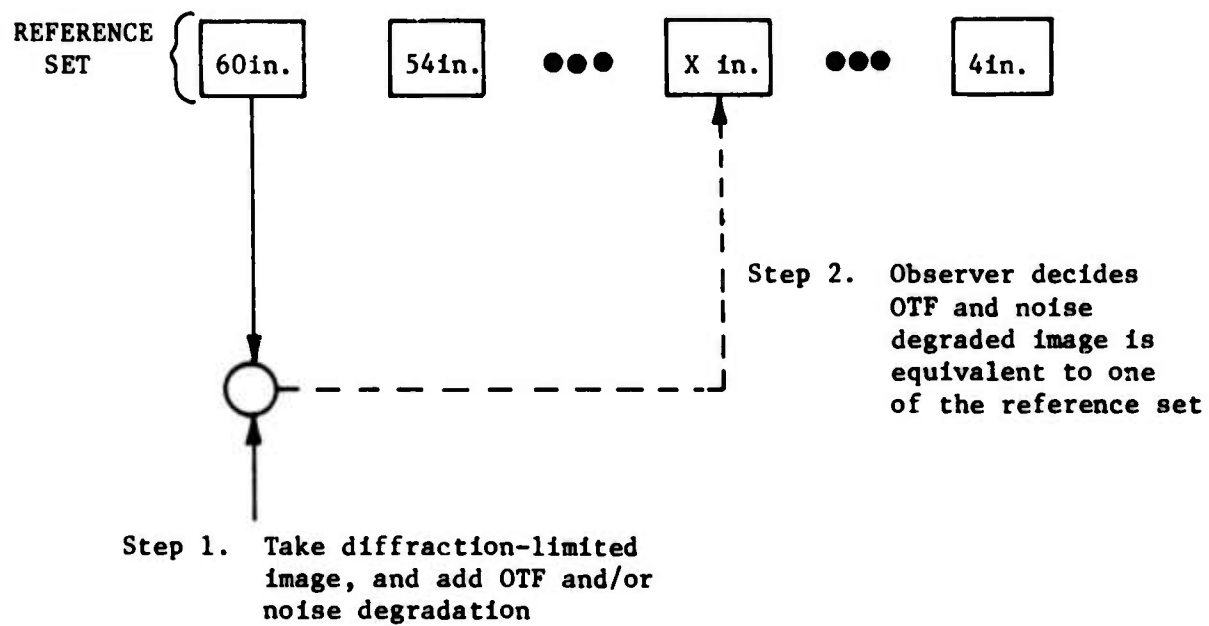


Figure 21. Viewing and Interpretation Experiment

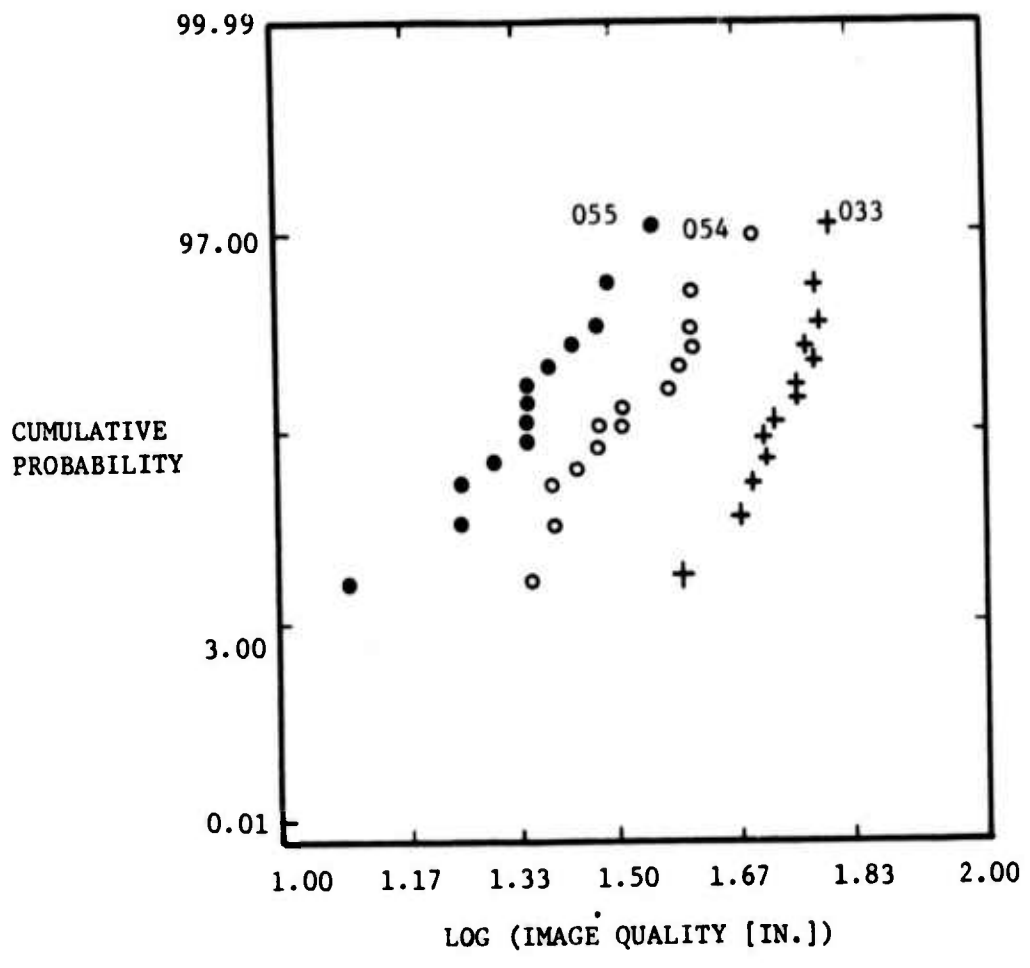


Figure 22. Cumulative Probability Distributions of Quality Estimates for Three Typical Images

TABLE 7. NOISELESS IMAGE V AND I RESULTS

SFT W ALL 10 NOISELESS SHORT AND LONG TE UT'S

P-HAT = SIG\*GNI

RMS QUAL ERROR = 2.4

IMAGE	DIA	GNI	STREML	A	SIG	DOBS	FALG	
1	15	60.	1.0	1.0000	0	0.0	57.6	1.00
2	52	60.	1.0	0.6920	0	0.0	49.3	1.14
3	48	60.	1.0	0.3370	0	0.0	35.9	1.22
4	44	60.	1.0	0.1280	0	0.0	22.0	1.25
5	40	60.	1.0	0.0320	0	0.0	9.1	1.19
6	36	60.	1.0	0.0044	0	0.0	3.4	1.41
7	89	60.	1.0	0.8380	0	0.0	52.6	1.07
8	90	60.	1.0	0.3920	0	0.0	32.0	1.16
9	91	60.	1.0	0.1090	0	0.0	10.0	1.20
A	92	60.	1.0	0.0310	0	0.0	7.7	1.19





TABLE 8. POISSON NOISE IMAGE V AND I RESULTS

SET A ALL 60 POISSON NOISE IMAGES

P-HAT = SIG\*GNI

RMS QUAL ERROR = 3.5

IMAGE	DIA	GNI	STREML	n	SIG	DDDS	FACD	
1	33	60.	1.0	1.0000	400	0.025	51.1	1.15
2	35	60.	1.0	1.0000	80	0.050	45.6	1.19
3	34	60.	1.0	1.0000	16	0.125	30.8	1.31
4	59	48.	1.0	1.0000	400	0.025	42.5	1.09
5	60	48.	1.0	1.0000	80	0.050	35.7	1.15
6	61	48.	1.0	1.0000	16	0.125	25.1	1.23
7	62	32.	1.0	1.0000	400	0.025	29.5	1.11
8	63	32.	1.0	1.0000	80	0.050	26.3	1.19
9	64	32.	1.0	1.0000	16	0.125	20.8	1.22
A	65	16.	1.0	1.0000	400	0.025	14.9	1.10
B	66	16.	1.0	1.0000	80	0.050	12.8	1.10
C	67	16.	1.0	1.0000	16	0.125	11.0	1.16
D	37	60.	1.0	0.0044	400	0.025	5.0	1.20
E	38	60.	1.0	0.0044	80	0.050	4.9	1.17
F	39	60.	1.0	0.0044	16	0.125	4.5	1.14
G	41	60.	1.0	0.0320	400	0.025	7.5	1.24
H	42	60.	1.0	0.0320	80	0.050	7.4	1.25
I	43	60.	1.0	0.0320	16	0.125	6.7	1.21
J	45	60.	1.0	0.1280	400	0.025	16.0	1.30
K	46	60.	1.0	0.1280	80	0.050	11.4	1.23
L	47	60.	1.0	0.1280	16	0.125	9.4	1.10
M	49	60.	1.0	0.3370	400	0.025	25.2	1.29
N	50	60.	1.0	0.3370	80	0.050	19.3	1.24
O	51	60.	1.0	0.3370	16	0.125	15.1	1.20
P	53	60.	1.0	0.6920	400	0.025	41.4	1.10
Q	54	60.	1.0	0.6920	80	0.050	31.5	1.20
R	55	60.	1.0	0.6920	16	0.125	22.2	1.27
S	69	60.	1.0	0.0320	2000	0.011	8.0	1.29
T	70	60.	1.0	0.1280	2000	0.011	16.9	1.24
U	71	60.	1.0	0.3370	2000	0.011	29.7	1.20
V	72	60.	6.5	0.8100	2000	0.011	22.0	1.20
W	77	60.	6.5	0.8100	400	0.025	14.9	1.17
X	78	60.	6.5	0.8100	80	0.050	7.9	1.33
Y	73	60.	3.5	0.8100	2000	0.011	38.8	1.31
Z	79	60.	3.5	0.8100	400	0.025	24.0	1.30
	80	60.	3.5	0.8100	80	0.050	12.6	1.20
	76	60.	1.5	0.8100	2000	0.011	51.0	1.13
	81	60.	1.5	0.8100	400	0.025	40.5	1.19
	82	60.	1.5	0.8100	80	0.050	22.9	1.35
	93	60.	1.0	0.8380	80	0.050	35.4	1.24
	94	60.	1.0	0.8380	400	0.025	48.4	1.13
	95	60.	1.0	0.8380	2000	0.011	51.4	1.11
	96	60.	1.0	0.3420	80	0.050	21.7	1.21
	97	60.	1.0	0.3420	400	0.025	27.2	1.15

TABLE 8. POISSON NOISE IMAGE V AND I RESULTS (CONTINUED)

SET X ALL 66 POISSON NOISE IMAGES

P-HAT = SIG\*GNI

RMS QUAL ERROR = 3.5

IMAGE	DIA	GNI	STREHL	N	SIG	DOBS	FACG
98	00.	1.0	0.3920	2000	0.011	28.9	1.17
99	00.	1.0	0.1090	80	0.056	10.4	1.12
100	00.	1.0	0.1090	400	0.025	11.5	1.12
101	00.	1.0	0.1090	2000	0.011	13.2	1.15
102	00.	1.0	0.0310	80	0.056	5.8	1.68
103	00.	1.0	0.0310	400	0.025	6.7	1.21
104	00.	1.0	0.0310	2000	0.011	7.6	1.17
105	00.	2.0	0.7900	80	0.056	23.1	1.33
106	00.	2.0	0.7900	400	0.025	35.2	1.27
107	00.	2.0	0.7900	2000	0.011	45.9	1.13
108	00.	9.5	0.8200	80	0.056	7.3	1.56
109	00.	9.5	0.8200	400	0.025	12.9	1.21
110	00.	9.5	0.8200	2000	0.011	23.0	1.32
135	00.	1.3	0.5700	2000	0.011	42.0	1.15
136	00.	2.4	0.3800	2000	0.011	27.7	1.17
137	00.	5.6	0.1700	2000	0.011	10.5	1.27
138	00.	1.3	0.5700	400	0.025	31.3	1.35
139	00.	2.4	0.3800	400	0.025	20.9	1.26
140	00.	5.6	0.1700	400	0.025	9.1	1.18
141	00.	1.3	0.5700	80	0.056	22.2	1.19
142	00.	2.4	0.3800	80	0.056	15.3	1.26
143	00.	5.6	0.1700	80	0.056	6.9	1.22

TABLE 9. GAUSSIAN NOISE IMAGE V AND I RESULTS

SET Y ALL 30 GAUSSIAN NOISE IMAGES

$\hat{P} = \text{SIG} * \text{GNI}$

RMS QUAL ERROR = 3.3

IMAGE	DIA	GNI	STREHL	N	SIG	UBS	FACD	
1	114	60.	1.0	1.0000	400	0.025	48.3	1.16
2	115	60.	1.0	1.0000	80	0.056	36.4	1.20
3	116	60.	1.0	1.0000	16	0.125	16.9	1.45
4	117	60.	1.0	1.0000	400	0.025	42.7	1.18
5	118	48.	1.0	1.0000	80	0.056	30.3	1.20
6	119	48.	1.0	1.0000	16	0.125	16.1	1.33
7	120	32.	1.0	1.0000	400	0.025	31.2	1.08
8	121	32.	1.0	1.0000	80	0.056	23.6	1.21
9	122	32.	1.0	1.0000	16	0.125	12.9	1.35
A	123	16.	1.0	1.0000	400	0.025	13.7	1.18
B	124	16.	1.0	1.0000	80	0.056	10.8	1.18
C	125	16.	1.0	1.0000	16	0.125	8.2	1.15
D	126	60.	1.0	0.3370	2000	0.011	29.8	1.21
E	127	60.	1.0	0.3370	400	0.025	24.3	1.24
F	128	60.	1.0	0.3370	80	0.056	15.5	1.27
G	129	60.	1.0	0.1280	2000	0.011	17.6	1.20
H	130	60.	1.0	0.1280	400	0.025	13.8	1.22
I	131	60.	1.0	0.1280	80	0.056	9.7	1.13
J	132	60.	1.0	0.0320	2000	0.011	8.2	1.18
K	133	60.	1.0	0.0320	400	0.025	7.3	1.18
L	134	60.	1.0	0.0320	80	0.056	6.8	1.14
M	144	60.	1.5	0.8100	2000	0.011	50.1	1.14
N	145	60.	1.5	0.8100	400	0.025	33.2	1.25
O	146	60.	1.5	0.8100	80	0.056	20.4	1.27
P	147	60.	3.8	0.8100	2000	0.011	33.8	1.20
Q	148	60.	3.8	0.8100	400	0.025	20.2	1.27
R	149	60.	3.8	0.8100	80	0.056	10.8	1.30
S	150	60.	6.5	0.8100	2000	0.011	26.2	1.25
T	151	60.	6.5	0.8100	400	0.025	13.3	1.27
U	152	60.	6.5	0.8100	80	0.056	6.3	1.38

- GNI - the factor by which the standard deviation of additive Gaussian noise has been increased by the application of post-detection compensation frequency domain filter
- STREHL - the Strehl ratio for the particular OTF, normalized to the diffraction-limited Strehl ratio for that aperture; for the case of post-detection processed images, the Strehl ratio is the post-processed Strehl ratio
- A - the value of the noise generation parameter (photoelectrons per pixel per unit reflectivity)
- SIG - the value of the rms noise in reflectivity units, before any post-detection processing
- DOBS - the value of the average quality of the image, as determined by the observers (units are inches of equivalent aperture)
- FACG - standard deviation factor for the set of quality estimates

In Section IV, the fitting of this raw data to various image quality measures will be discussed.

## SECTION IV

### ANALYSIS OF RESULTS

#### 4.1 IMAGE QUALITY CRITERIA

There are several classes of image quality criteria that are available, as shown in Table 10; the entries in Table 10 are listed in terms of the information concerning the image formation process that is used in the evaluation of each image quality criteria. It is to be expected that the measures that use the most information will be the ones that describe system performance.

##### 4.1.1 Class A: Strehl Ratio, Edge Sharpness, and Normalized Relative Energy

These measures are all characterized by the fact that each is a function only of the system transfer function. The Strehl ratio describes the value of the point spread function at the centroid, and is given by

$$S = \frac{\int T(k) dk}{\int T_{dl}(k) dk} = p(0,0) \quad (22)$$

$T(k)$  = system optical transfer function

$T_{dl}(k)$  = diffraction-limited transfer function for same size aperture

$p(0,0)$  = value of point spread function at the centroid

The unnormalized Strehl ratio has the units of spatial frequency squared; thus, the square root of the Strehl ratio, unnormalized, has the units of spatial frequency, and represents an effective spatial frequency bandwidth for the system whose transfer function is given by  $T(k)$ . In addition, the square root of the unnormalized Strehl ratio is proportional to the diameter of the aperture of the system; therefore, it lends itself dimensionally, at

TABLE 10. IMAGE QUALITY MEASURES

Type	Image Quality Measure	Information Used			
		Transfer Function	Noise	Object	Display
A	Strehl Ratio Edge Sharpness Normalized Relative Energy	X			
B	Image Sharpness Image-Object Correlation Image Fidelity	X		X	
C	Summary Measure	X	X		X

least, to use as a measure of image quality having the units of equivalent aperture diameter. However, the use of the Strehl ratio as a measure of image quality sometimes breaks down for comparison of images obtained through the transfer functions of widely differing shapes.

The edge response of the system describes the slope of the edge response of the system, and is a measure of how sharply edges are imaged. For systems that contain edges, this measure may be more appropriate than the Strehl ratio, which describes the imaging properties for point objects. The edge response is given by

$$E = \frac{d}{dx} [\ell(x)]_{x=0} = \int_{-\infty}^{\infty} k_x T(k_x, 0) dk_x \quad (23)$$

where

- E = slope of edge response
- $\ell(x)$  = line spread function

The normalized relative energy (NRE) criterion describes the fraction of the total energy contained in the system spread function that is contained within a circle of some diameter centered on the centroid of the point spread function. This criterion, similar to the Strehl ratio, is most suitable for systems in which detectors are used to make photometric measurements. The NRE is given by

$$\text{NRE} = \frac{\int_{A=\pi R^2} p(r) dr}{\int T(k) \frac{J_1(2\pi Rk)}{(2\pi Rk)} dk} \quad (24)$$

#### 4.1.2 Class B: Image Sharpness, Image-Object Correlation, Mean-Square Error

This class of image quality measures, representing two-dimensional generalizations of statistical measures used for evaluating time filters, was introduced by Linfoot<sup>6</sup>, and is discussed by O'Neill<sup>7</sup>.

The image sharpness criterion, which describes the relative structural content of an image, relative to the structural content of the object, is given by

$$T_{is} = \frac{\overline{i^2(r)}}{\overline{o^2(r)}} = \frac{\int |T(k)|^2 \phi(k) dk}{\int \phi(k) dk} \quad (25)$$

where

$i(r)$  = image in two dimensions

$o(r)$  = object

$\phi(k)$  = power spectrum of object

The image-object correlation measure is given below, and measures the alignment of the object and the image:

<sup>6</sup>E.H. Linfoot, J. Opt. Soc. Amer., 46, 740 (1956).

<sup>7</sup>E. O'Neill, Introduction to Statistical Optics, Addison Wesley, 1963, p. 106.

$$Q_{loc} = \frac{\overline{i(r)o(r)}}{o^2(r)} = \frac{\int T(k)\phi(k)dk}{\int \phi(k)dk} \quad (26)$$

The mean-square error between the image and the object is given by

$$D_{mse} = \frac{[\overline{o(r) - i(r)}]^2}{o^2(r)} = \frac{\int [1 - 2T(k) + |T(k)|^2] \phi(k) dk}{\int \phi(k) dk} \quad (27)$$

Like the Strehl ratio, the edge response, and the NRE, these three measures are not in themselves suitable for predicting the quality of images for systems where there is significant image noise.

#### 4.1.3 Class C: Summary Measure of Image Quality

Based on approximately ten years of investigations into the nature of image quality, Dr. R.E. Hufnagel of Perkin-Elmer has formulated a summary measure of image quality that takes into account the system transfer function, the image noise present in the system, the transfer function of the display medium used to present the image to the viewer (or post-process the image), and the transfer function of the eye of the observer.

$$Q(m_{opt}) = c \sqrt{\frac{M M_D \int_0^{k_{Nyq}} dk T(k) T_D(k) T_{eye}(k/m)}{1 + \frac{\alpha M_D^2}{M^2} \int_0^{k_{Nyq}} dk N(k) |T_D(k) T_{eye}(k/m)|^2}} \quad (28)$$



where

- $k = (k_x, k_y)$  measured at the display plane
- $dk = dk_x dk_y$
- $T(k)$  = system OTF up to the point where noise is introduced
- $T_D(k)$  = display OTF including image restoration attempts (after noise introduction) and display spot shape effects
- $k_{Nyq}$  = Nyquist frequency bounds, when the image is spatially quantized. In the absence of sampling  $k_{Nyq} = \infty$ .
- $T_{eye}(k)$  = human visual system MTF for 25-cm viewing distance, with  $k$  in units of cy/mm
- $m$  = magnification of viewing  $\left( = \frac{25 \text{ cm}}{\text{viewing distance for unaided eye}} \right)$
- $N(k)$  = noise Wiener spectral density for additive Gaussian noise. If the noise is not additive Gaussian, the closest equivalent is used (e.g., Poisson noise is evaluated at mean reflectivity). Note that the noise is to be expressed in units of (object reflectivity)<sup>2</sup>/(cy/mm)<sup>2</sup>. Expressing the noise as an apparent fluctuation of object reflectivity circumvents problems of illumination levels, display brightness, camera nonlinearities, etc. The eye-brain system automatically compensates for all these factors. If spatial sampling is used, the folded over noise spectrum is to be used.
- $\alpha$  = noise scaling factor (to be discussed)
- $M$  = pre-noise-introduction, modulation ratio factor to account for change of modulation due to haze or sensor gamma. No change implies  $M = 1$ .
- $M_D$  = post-noise introduction modulation factor including display. It is assumed that neither  $M$  nor  $M_D$  is big enough to cause significant loss of information by nonlinear saturation effects.
- $Q$  = overall image quality in units of spatial frequency
- $c$  = dimensionless scale factor (if this factor is the aperture diameter,  $Q$  has the units of equivalent aperture diameter).

The right-hand portion of the denominator is the mean squared noise as seen with the same magnification. The factor  $\alpha$  is a noise scaling term with the units (object reflectivity)<sup>-2</sup> and should be associated with the mean squared modulation in the object scene. For aerial photographs of ground terrain,  $\alpha = 1600$  has been found to give a best fit to experiments.

#### 4.2 EXPERIMENTAL DATA FIT TO SIMPLE SUMMARY MEASURE MODEL

The summary measure of image quality model contains a factor  $\alpha$ , which has not been determined for imagery of the type being simulated on this study - i.e., high-contrast images of small objects, as opposed to extended images of large low-contrast objects (aerial scenes) for which there is 10 years of data. Thus, it was of interest to take a simple version of the summary measure model, without the eye MTF, and determine the value of  $\alpha$  that best fits the experimental data from the V and I experiments.

Once that value of  $\alpha$  has been determined, then the model can be used to estimate the quality of each of the images viewed in the study; the rms error between the estimates made on the basis of the  $\alpha$  value and the actual observed values will indicate the ability of the model to handle the substantial variation conditions for which the simulations were generated. Once this step is complete, then the full model can be investigated.

Equation (28) describes the model for the case where the eye MTF has been set to unity; as shown, the measure reduces to a simple combination of

$$Q = D_o \sqrt{\frac{\int T(k)T_d(k)dk}{\sqrt{1 + \alpha N_o \int |T_d(k)|^2 dk}}} = \frac{S^{1/2}}{(1 + \alpha \sigma_r^2 N_I^2)^{1/4}} \quad (29)$$

where

$D_o$  = aperture diameter

$\sigma_r^2$  = noise variance (reflectivity<sup>2</sup>)

$N_I$  = additive Gaussian standard deviation increase factor  
( $\neq 1$  when post-processing is performed)

#### 4.2.1 Fit of Noiseless Images to Simple Model

Note that the simple model given in Equation (29) reduces to the square root of the Strehl ratio for the no noise case; Figure 23 illustrates the fit of experimentally determined quality estimates to the predicted quality determined from Equation (29), evaluated for no noise. Each image viewed is plotted with its abscissa coordinate being the predicted quality, and the ordinate being the observed experimentally determined quality, thus a perfect fit of the model to the data would result in all points lying on a straight line. As shown, the data fits the straight line quite well - the rms error between the observed quality and the predicted quality is 2.9 inches of equivalent aperture, for all 10 noiseless images generated for short and long time exposure OTF's.

#### 4.2.2 Fit of Poisson Noise Images to Simple Model

All of the Poisson noise images (67 in number) were taken as a group, and the  $\alpha$  value that minimized the mean square error between the predicted values and the observed values was determined to be a value of 1800. This value of  $\alpha$  was then used to derive predicted values for all of the Poisson noise images, with the resultant fit displayed in Figure 24. For the value of 1800, the root mean square error between the predicted quality and the observed quality is 3.5 inches of equivalent aperture.

Appendix C contains similar plots of the Poisson noise image results, but for each of the basic experiments plotted separately. Close examination of the individual plots reveals systematic deviations from the perfect straight-line match between predicted and observed; some of these deviations, although not large, will be further examined in a later section.

#### 4.2.3 Fit of Gaussian Noise Images to Simple Model

All of the Gaussian noise images (30 in number) were taken as a group, and the  $\alpha$  value that minimized the mean square error between the observed quality and the predicted quality was determined to be a value of 3400. Figure 25 illustrates the degree of fit to be about the same as it was for the Poisson noise images; for the Gaussian images, the rms error between the

SET = ALL IN NOISELESS SHORT AND LONG TE UTFS

P-HAT = SIG\*GNI

RMS QUAL ERROR = 2.9

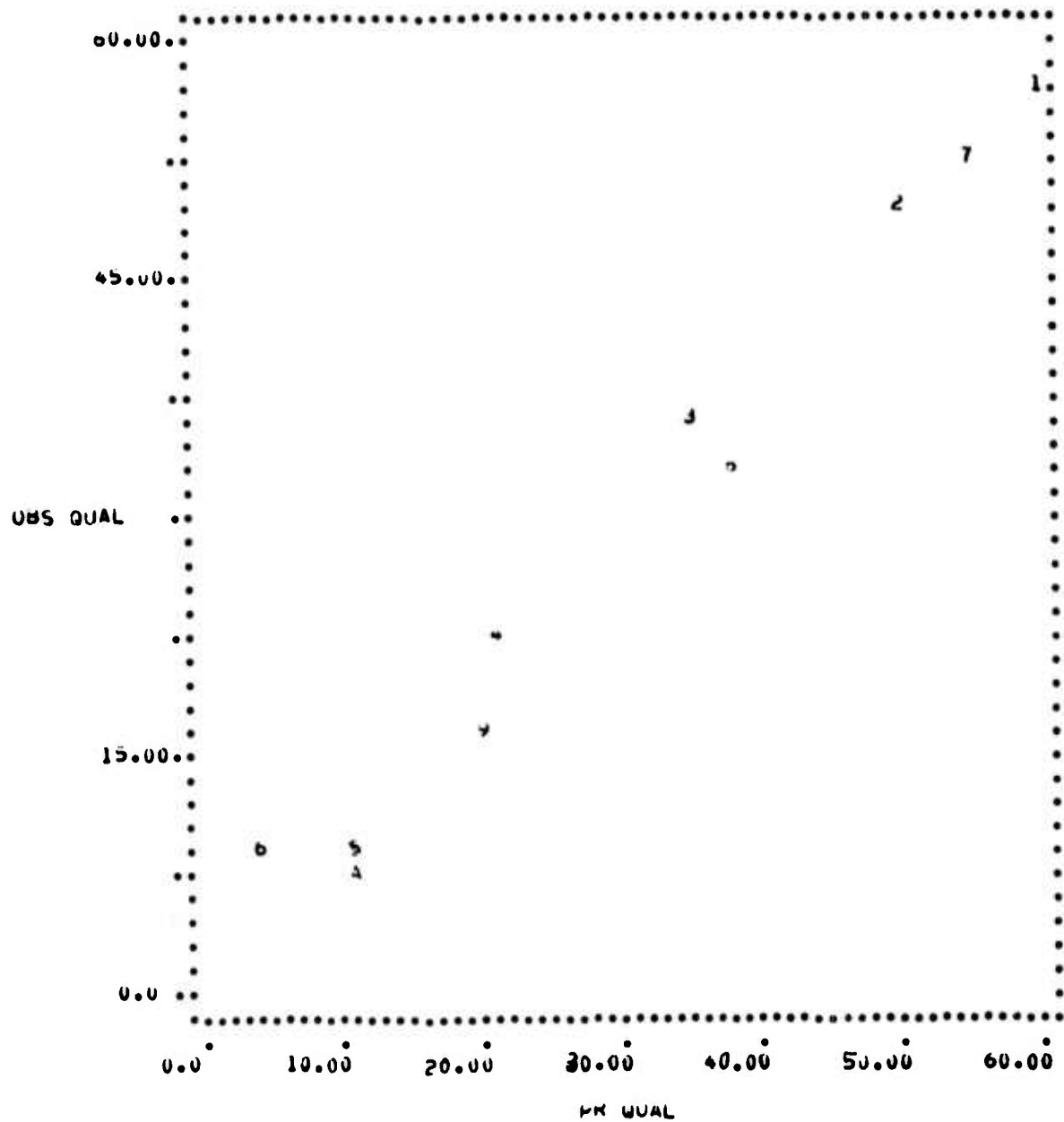


Figure 23. Noiseless Images Fit to Simple Model

FIT A ALL 60 POISSON NOISE IMAGES  
P-HAT = SIGMA^2 INPUT ALPHA = 1800.  
RMS QUAL ERROR = 3.5

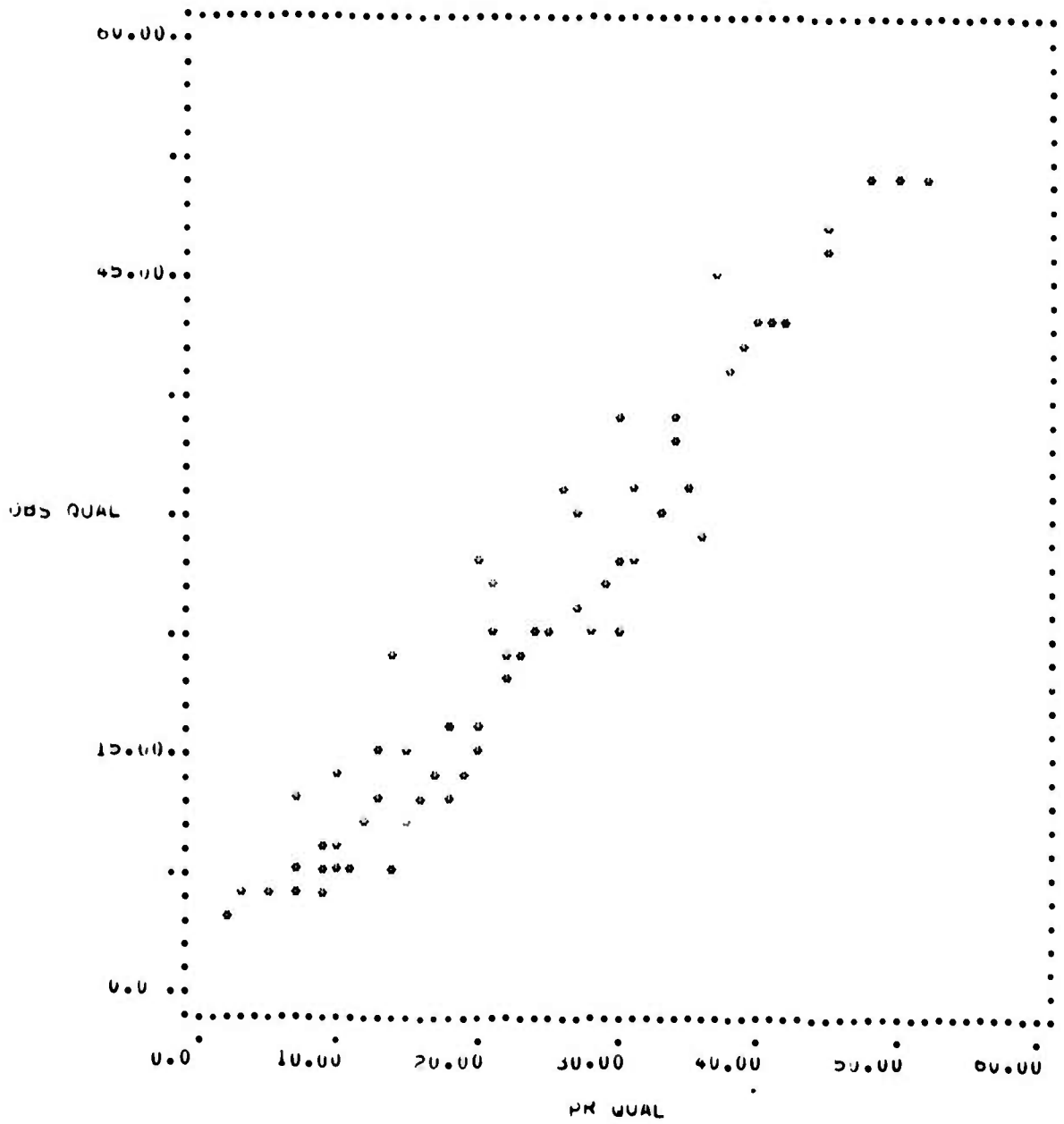


Figure 24. Poisson Noise Images Fit to Simple Model

SET Y ALL 30 GAUSSIAN NOISE IMAGES

P-HAT = SIG\*GNI

INPUT ALPHA = 3400.

RMS QUAL ERROR = 3.3

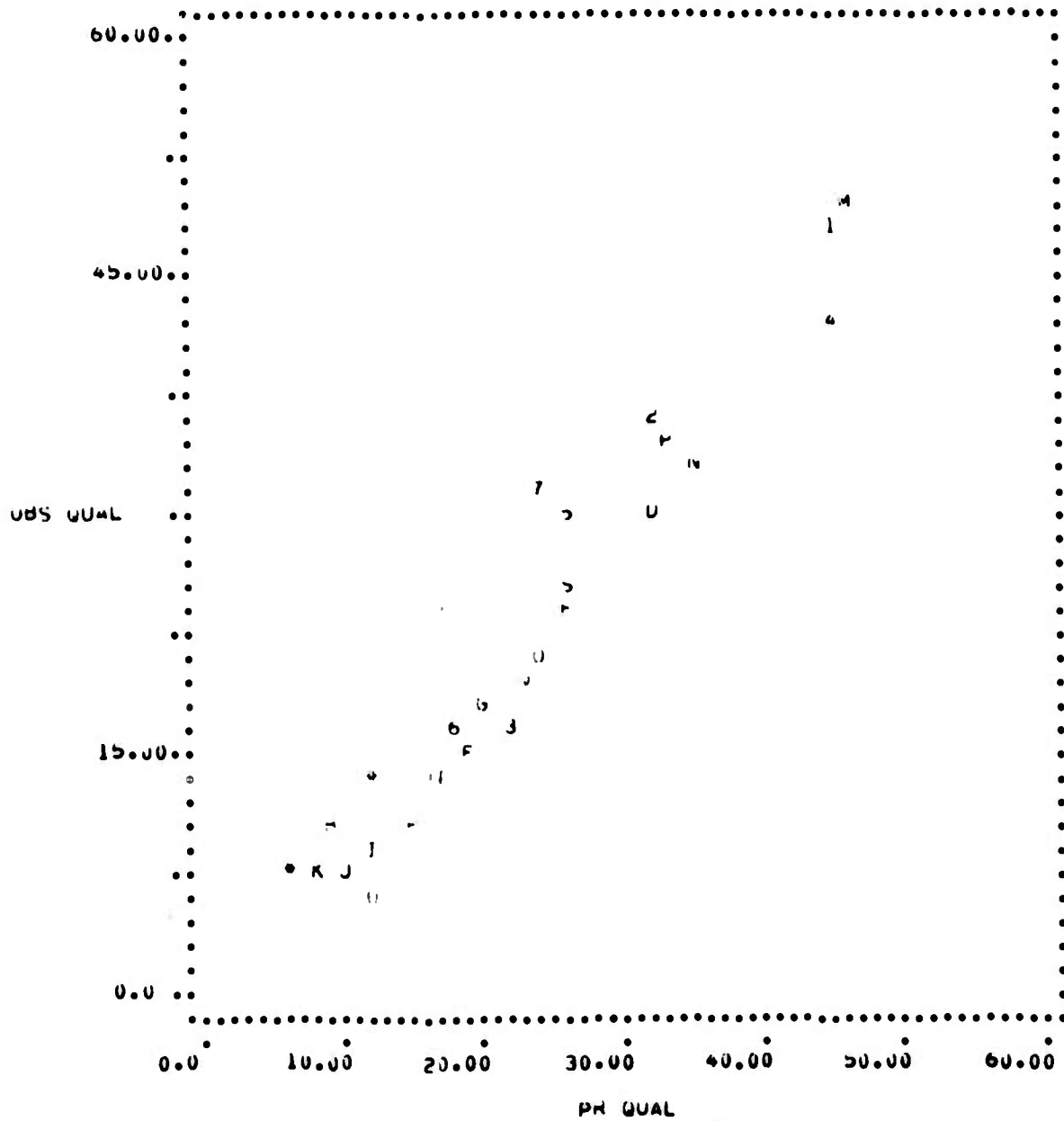


Figure 25. Gaussian Image Fit to Simple Model

predicted and observed is 3.3 inches of equivalent aperture diameter. Appendix C illustrates the plots of the individual experiments performed for the Gaussian noise simulations.

#### 4.2.4 Conclusions Concerning Fit to Simple Model

As a result of the application of the simple model to the total number of 106 images generated on the study, the simple model was found to predict quite well the observed quality of the images, for a wide range of noise and OTF conditions. Therefore, it is concluded that the simple model will serve well as a tool for estimating the quality of satellite images, for the type of generic degradations simulated in this study.

It should also be mentioned that the model has a larger percentage error in the region of poor image quality, and performs on a percentage basis far better for the case of good image quality, which is precisely the region where the tool will be most needed - i.e., for tradeoffs concerning the performance of a compensated imaging system that is producing images not too far from the quality of diffraction-limited images.

#### 4.3 EXPERIMENTAL FIT TO COMPLETE SUMMARY MEASURE MODEL

Once the examination of the ability of the simplified model to fit the data was completed, the evaluation of the full summary measure model including the eye MTF optimization was performed. For this case, Equation (28) becomes

$$Q = \frac{2(0.7845)D_0}{\sqrt{\pi} k_{Nyq}} \sqrt{\frac{\int_0^{k_{Nyq}} dk T(k) T_D(k) T_{eye}(k/m)}{1 + \alpha N_0 \int_0^{k_{Nyq}} dk |T_D(k) T_{eye}(k/m)|^2}} \quad (30)$$

where  $N_0$  = noise spectral density for equivalent Gaussian noise. Note that the scale factor outside the square root normalizes the resultant values of image quality such that for no noise  $Q$  has a value of 60 inches, for a diffraction-limited transfer function  $T(k)$  of a 60-inch aperture (the effect of optimizing the viewing magnification  $m$  for viewing a diffraction-limited transfer function is contained in the 0.7845 factor).

#### 4.3.1 Fit of Noiseless Images to Complete Model

For each of the 10 noiseless images, Equation (30) was used to determine the optimum (maximum) value of Q. The 10 resultant predicted quality values can be compared to the observed values as determined by the V and I experiments, as shown in Figure 26. The rms error for the 10 noiseless images is 2.0 inches.

#### 4.3.2 Fit of Noiseless Images to Various Models

Table 11 illustrates a comparison between four measures of image quality, again for the noiseless images. Shown are estimated quality values based on the full summary measure, the Strehl ratio (equivalent to the simple summary measure model), and two other figures of merit, as defined below).

4.3.2.1 Relative Image Sharpness - In paragraph 4.1, the image sharpness criterion was given as

$$T_{is} = \frac{\overline{i^2(r)}}{o^2(r)} = \frac{\int |T(k)|^2 \phi(k) dk}{\int \phi(k) dk} \quad (31)$$

where

$\phi(k)$  = object power spectrum

If the object spectrum is assumed to be flat, and T is normalized with respect to its value for a diffraction-limited transfer function  $T_{dl}(k)$ , a measure of relative image sharpness t, results

$$t = \frac{\int |T(k)|^2 dk}{\int |T_{dl}(k)|^2 dk} \quad (32)$$

This expression emphasizes the sharpness of the image, as measured by the mean square criterion; there is no explicit requirement that the image look like the object.



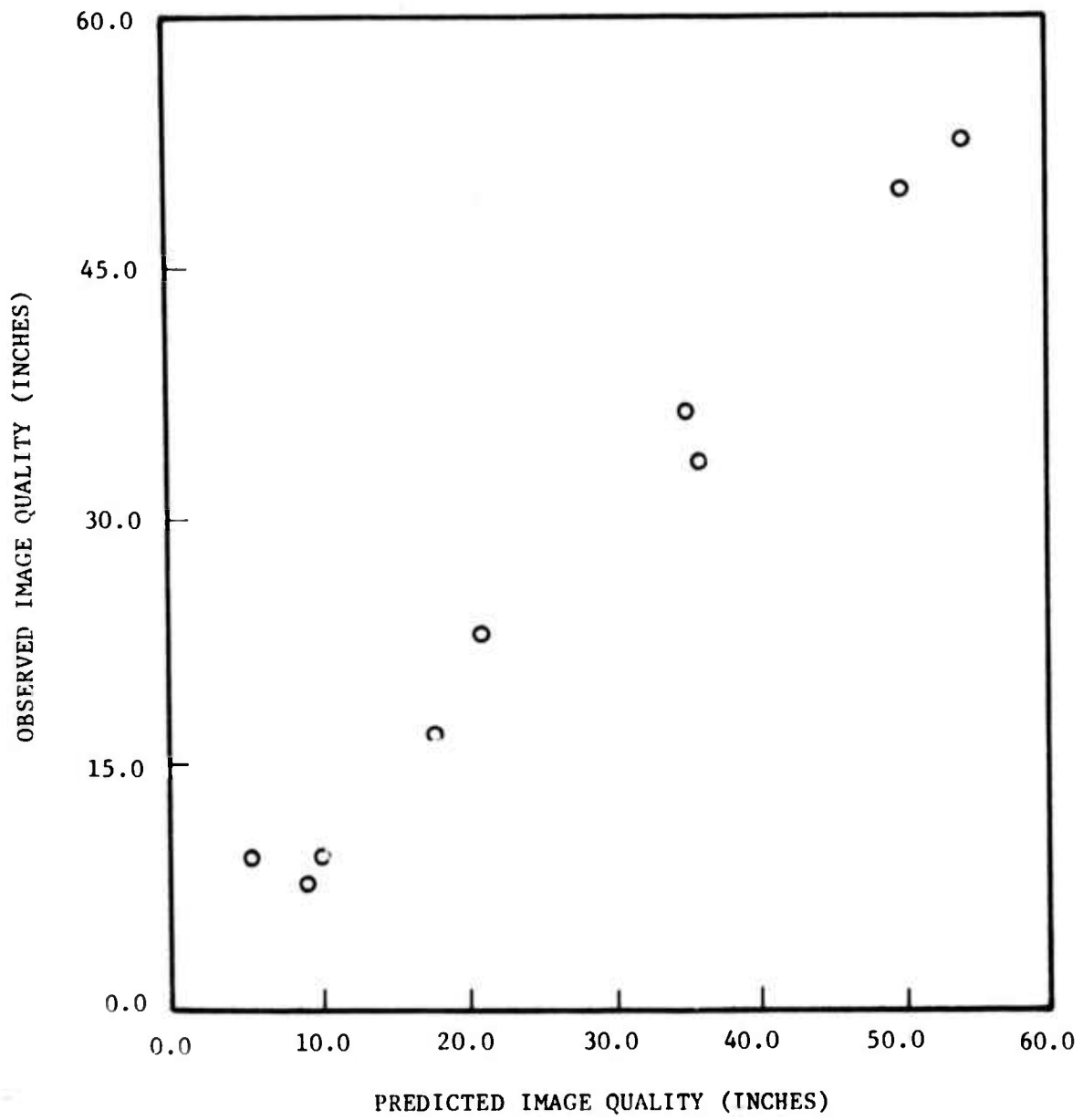


Figure 26. Noiseless Images Fit to Full Model

TABLE 11. COMPARISON OF VARIOUS IMAGE QUALITY CRITERIA FOR NOISELESS IMAGERY

Image	V&I Results	Strehl	Sharpness	Fidelity	Full Summary Measure
015	57.6	60.0	60.0	60.0	60.0
089	52.6	53.9	51.4	54.7	53.9
090	32.6	36.7	28.4	38.9	36.0
091	16.0	19.0	12.3	20.7	18.2
092	7.7	9.8	7.0	10.5	8.9
036	8.4	3.97	6.7	2.7	5.1
040	9.1	10.5	9.1	11.1	9.7
044	22.0	21.4	15.0	23.1	21.1
048	35.9	34.8	26.0	37.1	34.5
052	49.3	49.9	44.0	51.5	49.9
rms error =		2.9	4.7	3.5	2.0

4.3.2.2 Fidelity Defect - The mean square error between the image and the object was described in paragraph 4.1 as

$$D_{\text{mse}} = \frac{|o(r) - i(r)|^2}{o^2(r)} \quad (33)$$

Linfoot suggests that a fidelity criterion  $F$ , given by

$$F_c = 1 - D_{\text{mse}} \quad (34)$$

be used as a measure of system quality (this measure behaves the same way as do the others discussed in this report; i.e., it has a value of unity for no defect). If O'Neill's work is referenced and a flat object spectrum is assumed, the equation can be written as

$$f = \frac{q - \eta t}{1 - \eta} \quad (35)$$

where

$q$  = Strehl ratio (normalized)

$t$  = relative image sharpness

and

$$\eta = \frac{\int |T_{d\ell}(k)|^2 dk}{2 \int |T_{d\ell}(k)| dk} \quad (36)$$

As shown in Table 11, this fidelity criterion performs reasonably well as a measure of image quality; however, the results of the full summary measure yield the best fit to the results of the V and I experiments for noiseless imagery.

#### 4.3.3 Fit of Gaussian Noise Images to Full Summary Measure Model

In order to fit the Gaussian noise images to the full summary model, a double optimization procedure had to be performed. The objective of the procedure was to determine the value of  $\alpha$  that minimized the mean squared error between the predicted values and the observed values for all of the Gaussian noise images, for the case where the eye magnification was optimized for each image and value of  $\alpha$  individually. The results of this procedure, which

has been implemented in a software package, is shown in Figure 27; the rms error between the observed and predicted values of image quality is 3.5 inches rms, which is slightly higher than the 3.3-inch rms error that resulted from the use of the eye MTF independent model described in paragraph 4.2. The value of  $\alpha$  that produced the fit shown in Figure 27 is 2000.

#### 4.3.4 Fit of Poisson Noise Images to Full Summary Measure Model

Figure 28 illustrates the result of applying the same double optimization procedure to the Poisson noise image sets, with the result that the rms error between the predicted and observed quality is minimized at 3.0 inches rms for an  $\alpha$  of 1125; it should be noted that this error is somewhat less than the 3.5-inch rms value found using the eye MTF independent model.

#### 4.3.5 Conclusions Concerning Fit to Complete Summary Measure Model

As shown above, the use of the complete summary measure model yields some improvement over the performance of the eye MTF independent model based on a root mean square error criterion. However, the use of the complete model has resulted in a significant reduction in the average fractional error, as demonstrated by the reduction in the scatter of the results for small values of quality.

If the summary measure model is expressed as

$$Q = \text{DQRF} \cdot Q_0 \quad (37)$$

where

$Q$  = predicted quality

$Q_0$  = quality based on OTF only (no noise)

DQRF = dimensionless quality reduction factor

it can be seen that the dimensionless quality reduction factor (DQRF) has a much smaller error for the case of low quality estimates than does the corresponding DQRF for the simple model.

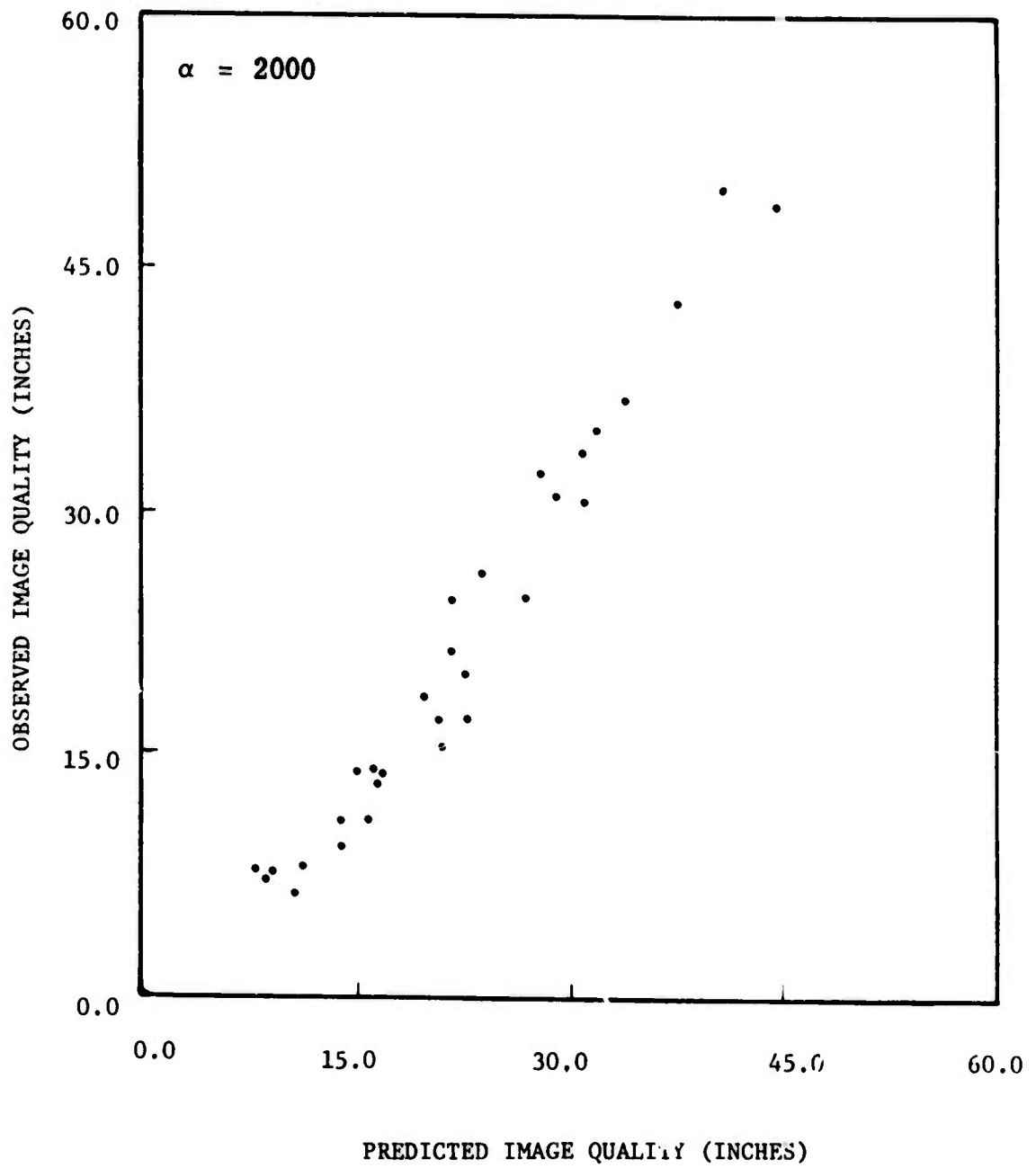


Figure 27. Gaussian Noise Images Fit to Full Model

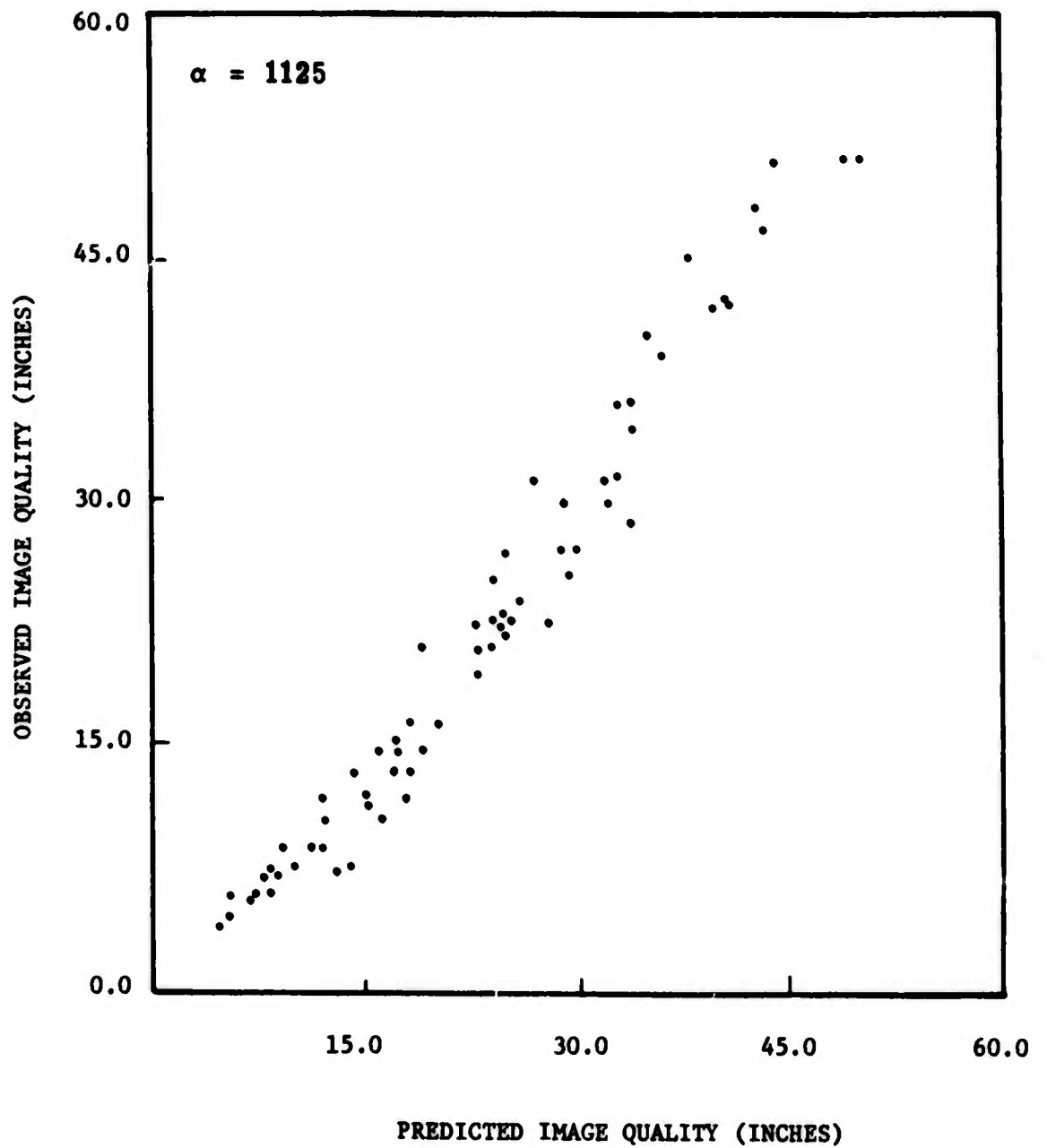


Figure 28. Poisson Noise Images Fit to Full Model

#### 4.4 USE OF MODEL FOR SYSTEM PERFORMANCE ANALYSIS

In the previous paragraphs, it was shown that the simple eye MTF independent summary measure model was sufficient to predict image quality to within an rms error of less than 4 inches; in this paragraph, this model will be used in a sample calculation to investigate the tradeoff between image quality, rms wavefront error, and exposure time.

By use of Equation (29), the resultant image quality for a given set of parameters can be derived; conversely the exposure time for a specified image quality can be derived by rewriting Equation (29) as follows:

$$t_e = \left[ \frac{Q^4}{D_o^4 S^2 - Q^4} \right] \cdot \alpha \sigma_r^2 N_I^2 \quad (38)$$

where

$N_I$  = noise standard deviation increase factor resulting from post-compensation restoration filter

$S$  = normalized Strehl ratio (normalized to 1.0 for diffraction-limited system)

Figure 29 illustrates the use of Equation (38) to derive a set of three isoquality curves, for an arbitrary object, for long time exposure imaging. In Figure 29, each point on an isoquality contour represents a combination of exposure time and pre-compensation system residual error that, when combined with a post-processing operation that yielded a Strehl ratio of 0.8, results in a system image quality of the denoted value. It should be noted that a post-compensation Strehl ratio of 0.8 corresponds to a quality  $Q$  of 54 inches; i.e., noiseless imagery would have the subjective quality of images obtained through a diffraction-limited 54-inch aperture. Also, it should be noted that as the residual wavefront error increases, the exposure time required to yield the same resultant image quality also increases.

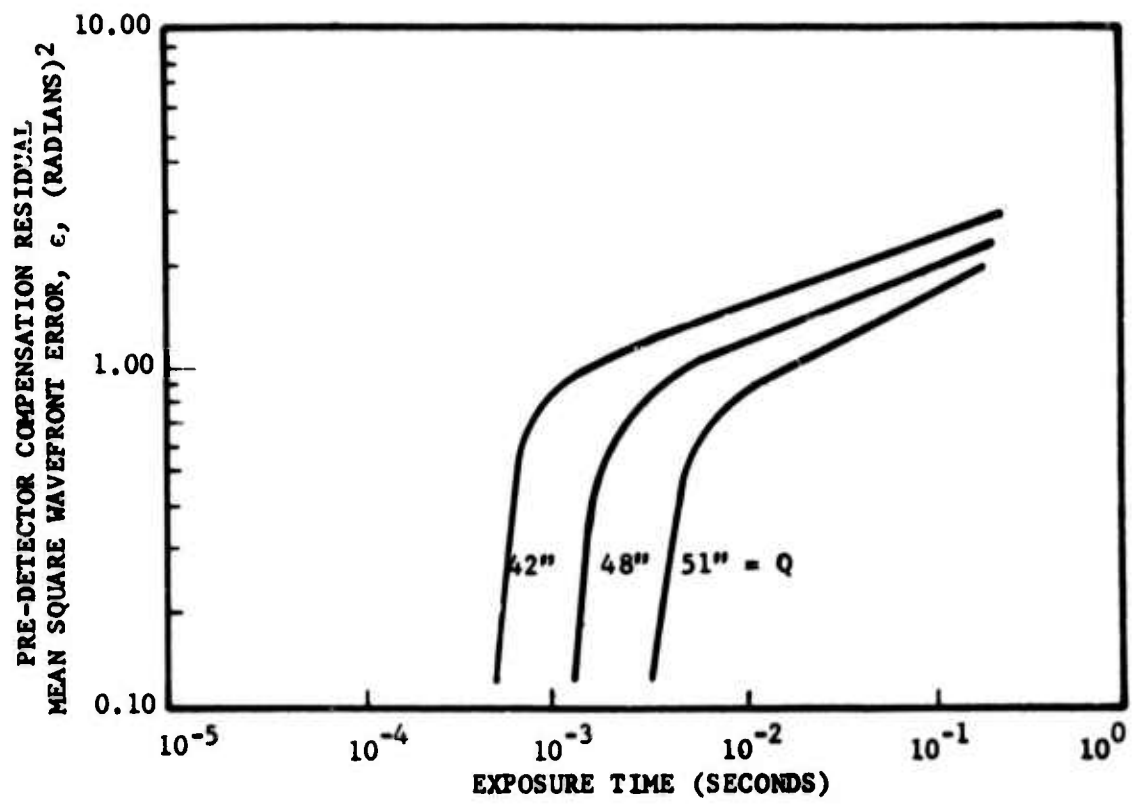


Figure 29. Isoquality Contours for an Object of Arbitrary Brightness



## SECTION V

### CONCLUSIONS, RECOMMENDATIONS AND SUMMARY

#### 5.1 CONCLUSIONS CONCERNING FIT TO SIMPLE MODEL

As a result of the application of the simple summary measure model to the total number of 106 images generated on the study, the simple model was found to predict quite well the observed quality of the images, for a wide range of noise and OTF conditions.

The scale parameter  $\alpha$  was found to be 1800 for the 66 Poisson noise images, and resulted in a 3.5-inch rms difference between the subjective quality (as determined by the viewing and interpretation experiments), and the quality predicted by the model. For the 30 Gaussian images, a value of  $\alpha = 3400$  was found to yield a fit with 3.3-inch rms error; for the 10 noiseless images, a fit of 2.9 inches rms was found.

The simple model was found to have a larger percentage error in the region of poor image quality, and was found to perform far better on a percentage basis for the case of good image quality, which is precisely the region where the tool will be most needed -i.e., for tradeoffs concerning the performance of a compensated imaging system that is producing images not too far from the quality of diffraction limited images.

Thus, it is concluded that the simple model will serve well as a tool for estimating the quality of satellite imagery, for the type of generic degradations simulated in this study.

#### 5.2 CONCLUSIONS CONCERNING FIT TO COMPLETE MODEL

The application of the more complete summary measure model, including the eye magnification optimization step, resulted in a moderate reduction in the rms error of the fit of the model to the results of the V and I experiments. For the Poisson noise, a value of  $\alpha$  of 1125 yielded an rms error of 3.0 inches, while for the Gaussian images, a value of  $\alpha$  of 2000 yielded

an rms error of 3.5 inches. The fit of the noiseless images was reduced from 2.9 inches rms, to 2.0 inches rms.

However, the complete model performed significantly better on a percentage basis, as indicated by the reduction of the scatter of the data shown in Figures 27, 28, and 29, in the region of poor image quality.

Thus it is concluded that the complete model, including the eye transfer function, does provide a more complete description of the relationship between the perceived image quality (as determined by human observers), and various descriptions of system transfer function and noise performance.

### 5.3 RECOMMENDATIONS

As a result of the study described in this report, two recommendations are made, as follows:

- (1) Repeat some of the experiments performed during the study for several different satellite images.
- (2) Examine the question of optimum post-processing by generating images that have been post-compensated by Weiner filters, geometric mean filters, and any other algorithms that appear to have applications to the post-compensation function.

### 5.4 SUMMARY

In summary, it is concluded that a useful model exists relating the subjective image quality of satellite imagery to various quantitative measures of system performance; the quantitative measures that are required include the system optical transfer function, and the spectrum and strength of the noise degrading the imagery.

With this model in hand, it is now possible to perform system tradeoffs to determine the optimum split between the performance of the pre-compensation function and the post-compensation function for a compensated imaging system; in addition, it is possible to perform tradeoffs concerning the form and nature of the post-processing algorithms to be used on the post-compensation function.

## REFERENCES

1. D.L. Fried, "Optical Resolution Through a Randomly Inhomogeneous Medium for Very Long and Very Short Exposures", J. Opt. Soc. Amer., Vol. 56, No. 11, 1372 (1966).
2. R.E. Hufnagel, "On the Mean Short-Term Blue", Woods Hole Summer Study on Restoration of Atmospherically Degraded Images, Vol. 2, Appendix 4 (July 1966).
3. D. Korff, "Analysis of a Method for Obtaining Near-Diffraction Limited Information in the Presence of Atmospheric Turbulence", J. Opt. Soc. Amer., Vol. 63, No. 8, 971 (1973).
4. R.E. Hufnagel and E.L. Kerr, "A Simple Algorithm for Fast Real-Time Generation of Pseudorandom Poisson Integers with Rapidly Varying Means", Proc. IEEE, Vol. 57, No. 11, 2088 (1969).
5. F. Scott, "The Search for a Summary Measure of Image Quality", Photo. Sc. & Eng., Vol. 12, 154 (1968).
6. E.H. Linfoot, J. Opt. Soc. Amer., 46, 740 (1956).
7. E. O'Neill, Introduction to Statistical Optics, Addison Wesley, 1963, p. 106.

**APPENDIX A**

**RANDOM WAVEFRONT GENERATION  
USING ZERNIKE POLYNOMIALS**

## SECTION A-I

### INTRODUCTION

This appendix describes a technique for generating random wavefronts that simulate the statistics of an atmospherically distorted wavefront. The atmosphere is described by a Kolmogoroff spectrum and the wavefront is treated as an expansion in Zernike polynomials.

Section A-II describes the mathematical preliminaries, Section A-III states the procedure for generating wavefronts, and Section A-IV contains the evaluation of an integral used in Section A-II.

SECTION A-II

ATMOSPHERIC STATISTICS FOR A MODAL REPRESENTATION

The aberration function  $\phi$  will be expanded in terms of a complete set of functions  $\{f_j(\rho\theta)\}$ .

$$\phi(\rho\theta) = \sum_j^{\infty} \alpha_j f_j(\rho\theta) \quad (\text{A-1})$$

The functions  $f_j$  are orthonormal so that

$$\int_0^1 \int_0^{2\pi} \rho d\rho d\theta f_j^*(\rho\theta) f_{j'}(\rho\theta) = \delta_{jj'} \quad (\text{A-2a})$$

or

$$\int d^2r f_j^*(r) f_{j'}(r) = \delta_{jj'} \quad (\text{A-2b})$$

The mean square error  $E$  produced by such an expansion is defined as

$$E = \int d^2r [\phi(r) - \phi_n(r)]^2 \quad (\text{A-3})$$

where  $\phi_n(\rho\theta)$  is the  $n^{\text{th}}$  order polynomial expansion in Equation (A-1). Substituting Equation (A-1) into Equation (A-3) for  $\phi_n$  and finding the set of  $\{\alpha_j\}$  that minimizes  $E$  yields

$$E = \int d^2r \phi^2(r) - \sum_{j=1}^n |\alpha_j|^2 \quad (\text{A-4})$$

with

$$\alpha_j = \int d^2r \phi(r) f_j(r) \quad (\text{A-5})$$

The aberration function is taken to be that associated with an atmospherically distorted random wavefront so that an average mean square error can be defined as

$$\langle E \rangle = \int d^2r \langle \phi^2(r) \rangle - \sum_j \langle |\alpha_j|^2 \rangle = \Delta \quad (\text{A-6})$$

Over the aperture the random wavefront is assumed stationary so that Equation (A-6) reduces to

$$\Delta = \pi \sigma_\phi^2 - \sum_j \langle |\alpha_j|^2 \rangle, \quad (\text{A-7})$$

where  $\sigma_\phi^2$  is the variance of the wave fluctuations and can be defined in terms of the power spectral density  $W(k)$  of the fluctuations as

$$\sigma_\phi^2 = \int \frac{d^2k}{(2\pi)^2} W(k) \quad (\text{A-8})$$

where  $k = (k_x, k_y)$

The mean square value of the coefficients  $\{\alpha_j\}$  can now be expressed in terms of  $W(k)$ . The Fourier transform of the functions  $f_j(r)$  is defined as

$$F_j(k) = \int d^2r f_j(r) e^{-ik \cdot r} \quad (\text{A-9})$$

where  $r = (x, y)$

with inverse transform

$$f_j(r) = \int \frac{d^2k}{(2\pi)^2} F_j(k) e^{ik \cdot r} \quad (\text{A-10})$$

From Equation (A-5), the mean square value of the coefficients is

$$\langle |\alpha_j|^2 \rangle = \iint d^2r' d^2r \langle \phi(r) \phi(r') \rangle f_j(r) f_j(r') \quad (\text{A-11})$$

Substituting Equation (A-10) into Equation (A-11) and making the transformation,

$$r' = r + \tau$$

yields

$$\langle |\alpha_j|^2 \rangle = \int \frac{d^2k}{(2\pi)^2} |F_j(k)|^2 \int d^2\tau \langle \phi(r) \phi(r+\tau) \rangle e^{i(k \cdot \tau)} \quad (A-12)$$

Equation (A-12) is thus easily expressed in terms of the fluctuation spectrum as

$$\langle |\alpha_j|^2 \rangle = \int \frac{d^2k}{(2\pi)^2} |F_j(k)|^2 W(k) \quad (A-13)$$

Generalizing Equation (A-13), the quantity  $\langle \alpha_j^* \alpha_j \rangle$  can be written as

$$\langle \alpha_j^* \alpha_{j'} \rangle = \int \frac{d^2k}{(2\pi)^2} F_j^*(k) W(k) F_{j'}(k) \quad (A-14)$$

Equation (A-14) defines a matrix representation of the spectrum  $W(k)$  which is denoted by

$$A = \left[ a_{jj'} \right] = \left[ \langle \alpha_j^* \alpha_{j'} \rangle \right] \quad (A-15)$$

One further item should be mentioned in connection with a generalized modal expansion, and that is closure. Equation (A-7) describes the error resulting from taking a finite number of terms in the expansion. The quantity  $\Delta$  must always be positive and as such provides a good measure for deciding how efficiently the random wavefront has been generated. An alternative form for Equation (A-7) is

$$\Delta = \int \frac{d^2k}{(2\pi)^2} W(k) - \sum_j \int \frac{d^2k}{(2\pi)^2} |F_j(k)|^2 W(k) \quad (A-16)$$



### Zernike Polynomial Expansion

In the following the orthonormal set of functions  $f_j(\rho\theta)$  are taken to be Zernike Polynomials,  $Z_j(\rho\theta)$  where

$$Z_j(\rho\theta) = f_n^{\pm m}(\rho\alpha) = \sqrt{\frac{n+1}{\pi}} R_n^{\pm m}(\rho) e^{\pm im\theta} \quad (0 < \rho < 1) \quad (\text{A-17})$$

The first few polynomials are shown in Table A-1 with  $Z_j = f_j/\sqrt{\pi}$ . The Fourier transform of Equation (A-17) is

$$Q_j(k) = F_n^m(k_1 k_\theta) = 2i^m \sqrt{\pi(n+1)} (-1)^{(n-m)/2} \frac{J_{n+1}(k)}{k} e^{imk\theta} \quad (\text{A-18})$$

The spectrum of turbulence is taken to be a Kolmogoroff spectrum, which can be written as

$$W(k) = 19.29 \left(\frac{a}{r_0}\right)^{5/3} k^{-11/3} \quad (\text{A-19})$$

Equation (A-19) is different from the usual Kolmogoroff spectrum in that the radius,  $a$ , of the telescope aperture is included. This definition is convenient because it allows all equations and computer calculations to be performed for a unit radius aperture. Thus, the spatial frequency  $k$  has units of radians/unit radius.

The matrix representation defined in Equation (A-15) yields a Zernike representation of the Kolmogoroff spectrum written as

$$a_{jj'} = 2 \left[ 19.29 \left(\frac{a}{r_0}\right)^{5/3} \right] \left[ \binom{n+1}{n'+1} \right]^{1/2} (-1)^{(n+n'-2m)/2} \cdot \int_0^\infty dk \frac{J_{n+1}(k) J_{n'+1}(k)}{k^{14/3}} \quad (\text{A-20})$$

Because of the relationship between the  $j$  indices and the  $n, m$  indices implied in Table A-1, the matrix elements  $a_{jj'}$ , with even-odd subscripts are zero (i.e.,  $a_{23} = a_{54} = 0$ , etc.). This is a consequence of the circular symmetry

TABLE A-1. ZERNIKE POLYNOMIALS

AZIMUTHAL FREQUENCY - M						
RADIAL DEGREE N	0	1	2	3	4	5
0	$P_1 = 1$ CONSTANT					
1		$P_2 = 2 r \cos \theta$ $P_3 = 2 r \sin \theta$ TILTS (LATERAL POSITION)				
2	$P_4 = \sqrt{3} (2r^2 - 1)$ DEFOCUS (LONGITUDINAL POSITION)		$P_5 = \sqrt{6} r^2 \sin 2\theta$ $P_6 = \sqrt{6} r^2 \cos 2\theta$ ASTIGMATISM (3rd ORDER)			
3		$P_7 = \sqrt{8} (3r^3 - 2r) \sin \theta$ $P_8 = \sqrt{8} (3r^3 - 2r) \cos \theta$ COMA (3rd ORDER)		$P_9 = \sqrt{8} r^3 \sin 3\theta$ $P_{10} = \sqrt{8} r^3 \cos 3\theta$		
4	$P_{11} = \sqrt{5} (6r^4 - 6r^2 + 1)$ 3rd ORDER SPHERICAL		$P_{12} = \sqrt{10} (4r^4 - 3r^2) \cos 2\theta$ $P_{13} = \sqrt{10} (4r^4 - 3r^2) \sin 2\theta$		$P_{14} = \sqrt{10} r^4 \cos 4\theta$ $P_{15} = \sqrt{10} r^4 \sin 4\theta$	
5		$P_{16} = \sqrt{12} (10r^5 - 12r^3 - 3r) \cos \theta$ $P_{17} = \sqrt{12} (10r^5 - 12r^3 - 3r) \sin \theta$		$P_{18} = \sqrt{12} (5r^5 - 4r^2) \cos 3\theta$ $P_{19} = \sqrt{12} (5r^5 - 4r^2) \sin 3\theta$		$P_{20} = \sqrt{12} r^5 \cos 5\theta$ $P_{21} = \sqrt{12} r^5 \sin 5\theta$
6	$P_{22} = \sqrt{7} (20r^6 - 30r^4 + 12r^2 - 1)$ 5th ORDER SPHERICAL		$P_{23}$ $P_{24}$		$P_{25}$ $P_{26}$	

in  $W(k)$ . The modes associated with odd  $j$  have their angular dependence described by  $\sin m \theta$  while those of even  $j$  are described by  $\cos m \theta$ . Clearly, the angular integrations with mixed sines and cosines are zero. The integral in Equation (A-20) is a tabulated integral and yields a number for all the matrix elements  $a_{jj}$ , except  $a_{11}$  ( $n=n'=0$ ), the piston coefficient. Since the total variance of the Kolmogoroff spectrum is infinite, it is not surprising to find an infinite piston coefficient. Leaving the integral evaluations to Section IV, it is found that the closure relation, Equation (A-16) for the piston corrected spectrum can be written for the Zernike representation of the Kolmogoroff spectrum as

$$\Delta_1 = \lim_{k_0 \rightarrow 0} \left\{ \pi \int_{k_0}^{\infty} W(k) \frac{kdk}{2\pi} - \int_{k_0}^{\infty} |Q_1(k)|^2 W(k) \frac{kdk}{2\pi} \right\} \quad (A-21)$$

$$\Delta_1 = \lim_{k_0 \rightarrow 0} \left\{ 19.29 \left( \frac{a}{r_0} \right)^{5/3} \left[ \frac{3}{10} k_0^{-5/3} - \frac{3}{10} k_0^{-5/3} - \frac{3}{8} k_0^{1/8} + 0.5324 \right] \right\}$$

or that

$$\frac{\Delta_1}{\pi} = 1.03 \left( \frac{D}{r_0} \right)^{5/3} \quad (\text{rad}^2) \quad (A-22)$$

which is the mean-square piston corrected error first derived by Fried<sup>1</sup>. Thus, infinite variance of the spectrum is associated only with the piston and is of no serious physical consequence.

With the value of the integral in Equation (A-20) given in Section IV the exact mean-square error resulting from using  $N$  modes can be evaluated. In the limit of large  $N$ , an asymptotic formula has been extracted,

$$\frac{\Delta_N}{\pi} = 0.2944 N^{-0.866} (D/r_0)^{5/3} \quad (\text{rad}^2) \quad (A-23)$$

<sup>1</sup>D.L. Fried, J. Opt. Soc. Amer., 55 1427 (1965).

The matrix elements given by Equation (A-20) are used in the next section to generate random wavefronts.

## SECTION A-III

### GENERATING RANDOM WAVEFRONTS

In this section the method of generating random wavefronts is discussed. The heart of the method rests upon the matrix A described in Section A-II. Because the Kolmogoroff spectrum is a real symmetric spectrum the matrix A is a real symmetric matrix and as such can be factored into

$$A = L \tilde{L} \quad (\text{A-24})$$

where L is a lower triangular matrix  $\ell_{ij}$

$\tilde{L}$  is the transpose of L

The Cholesky<sup>2</sup> decomposition method of factoring A was used in all random wavefront simulations.

The object of a wavefront simulation is to generate random numbers  $\{\alpha_j\}$  such that

$$\langle \alpha_j \rangle = 0, \quad \langle \alpha_j^* \alpha_j \rangle = a_{jj}, \quad (\text{A-25})$$

This can be achieved if

$$\alpha_j = \sum_i \ell_{ji} q_i \quad (\text{A-26})$$

with

$$\langle q_i \rangle = 0, \quad \langle q_i q_j \rangle = \delta_{ij} \quad (\text{A-27})$$

The desired random wavefront is then from Equation (A-1)

$$\phi(\rho\theta) = \sum_j \alpha_j f_j(\rho\theta) \quad (\text{A-28})$$

<sup>2</sup>See, e.g., J.H. Wilkinson, "The Algebraic Eigenvalue Problem", Oxford, Fairlawn, New Jersey (1965).

A computer generated random wavefront then consists of the procedures, as shown in Figure A-1.

- (1) Calculate the matrix A.
- (2) Factor the matrix A into  $L \tilde{L}$ .
- (3) Generate the random numbers  $q_i$ .
- (4) Calculate random coefficients  $\alpha_j$  from Equation (A-26).
- (5) Calculate random wavefront from Equation (A-28).

MONTE CARLO SIMULATIONS OF  
 PHASE FLUCTUATIONS CAUSED  
 BY ATMOSPHERIC TURBULENCE

PHASE WIENER  
 SPECTRUM

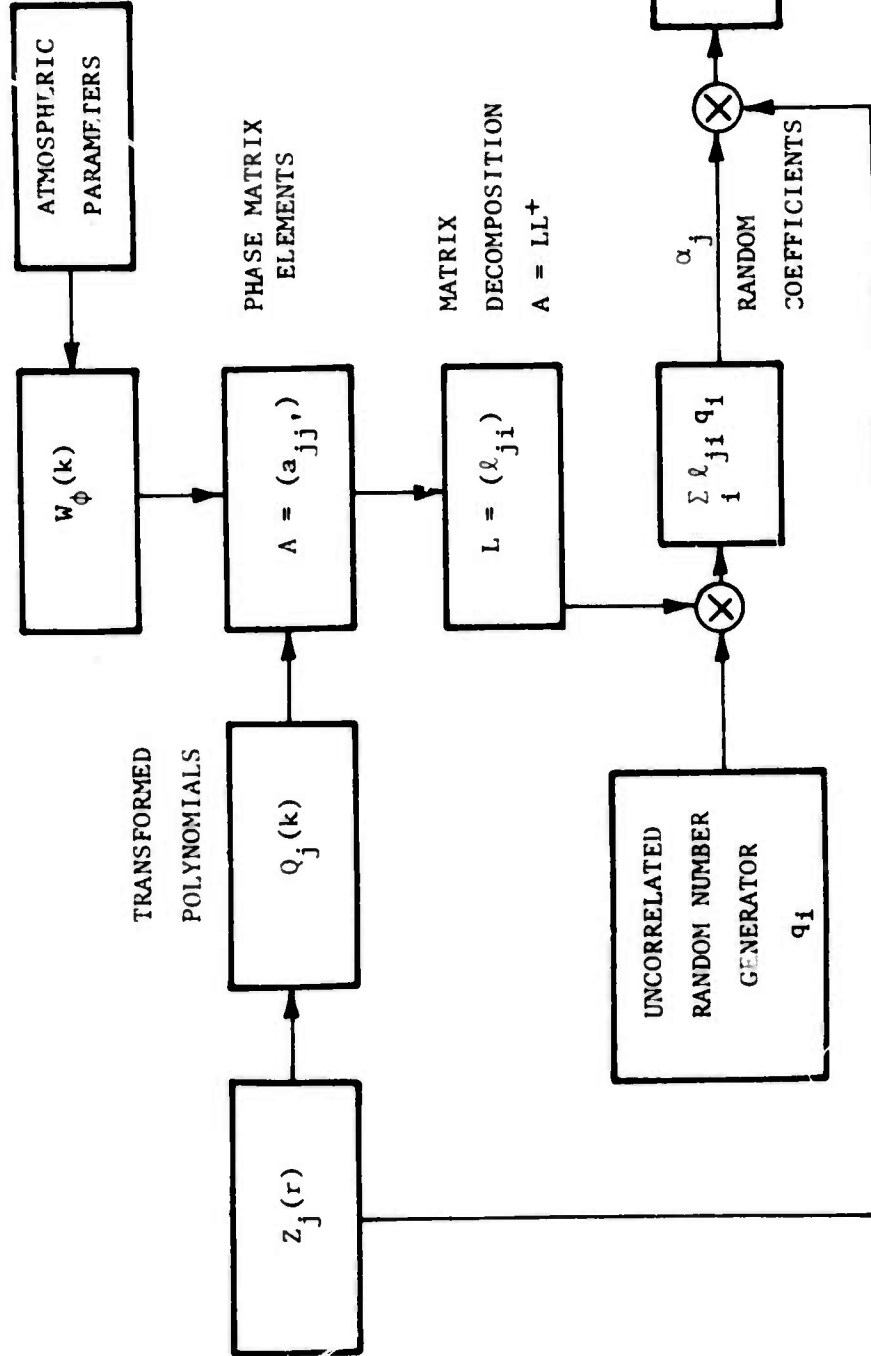


Figure A-1. Random Wavefront Simulation

SECTION A-IV

EVALUATION OF THE INTEGRAL  $I_{nn'}$

In this section the integral in Equation (A-20)  $I_{nn'}$ , is evaluated.

$$I_{nn'} = \int_0^{\infty} dk \frac{J_{n+1}(k) J_{n'+1}(k)}{k^{14/3}} \quad (A-29)$$

This integral is tabulated in most standard integral table handbooks of Bessel function integrals.

$$I_{nn'} = \frac{\Gamma(14/3) \Gamma\left(\frac{n+n' - 14/3 + 3}{2}\right)}{2^{14/3} \Gamma\left(\frac{-n+n' + 14/3 + 1}{2}\right) \Gamma\left(\frac{n-n' + 14/3 + 1}{2}\right) \Gamma\left(\frac{n+n' + 14/3 + 3}{2}\right)} \quad (A-30)$$

for  $n, n' \neq 0$

where  $\Gamma(x)$  is the gamma function.

The piston integral  $I_{00}$ , as indicated in the text, needs special attention. Let us write

$$I_{00} = \int_{k_0}^{\infty} \frac{|J_1(k)|^2 dk}{k^{14/3}} \quad (A-31)$$

Equation (A-31) can be integrated by using the identity

$$\pi \left[ \frac{2J_1(k)}{k} \right]^2 = \int d^2 r g(r) e^{-ik \cdot r} \quad (A-32)$$



with

$$g(r) = \frac{2}{\pi} \left[ \cos^{-1}(r/2) - \frac{r}{2} \sqrt{1 - (r/2)^2} \right] \quad r \leq 2 \quad (\text{A-33})$$

$$= 0 \quad r > 2$$

Equation (A-31) then can be written as

$$I_{\infty} = \frac{1}{4\pi} \int_0^{\infty} r dr q(r) \int_0^{2\pi} d\theta \int_{k_0}^{\infty} dk k^{-8/3} e^{-ikr \cos\theta} \quad (\text{A-34})$$

The  $k$  integration is recognized as an incomplete gamma function so that

$$\int_{k_0}^{\infty} dk k^{-8/3} e^{-ikr \cos\theta} = (ir \cos\theta)^{5/3} \left[ \Gamma(-5/3) - \sum_{n=0}^{\infty} \frac{(-1)^n (ik_0 r \cos\theta)^{-5/3+n}}{(n - 5/3) n!} \right] \quad (\text{A-35})$$

The first term on the right of Equation (A-35) can be written as

$$(ir \cos\theta)^{5/3} \Gamma(-5/3) = \frac{27}{10} i^3 (r \cos\theta)^3 \int_0^{\infty} t^{4/3-1} e^{-irt \cos\theta} dt \quad (\text{A-36})$$

Substituting Equations (A-35) and (A-36) into Equation (A-34) and performing the angular integration yields

$$I_{\infty} = \frac{1}{4\pi} \int_0^{\infty} r dr g(r) \left\{ \frac{6\pi}{5} k_0^{-5/3} - \frac{27\pi}{20} 2^{1/3} r^{5/3} \left[ \frac{8}{5} \frac{\Gamma(7/6)}{\Gamma(5/6)} \right] \right. \\ \left. - 2\pi k_0^{-5/3} \sum_{\ell=1}^{\infty} \frac{(-1)^{2\ell} (rk_0)^{2\ell} \left( \frac{1}{2} \dots \frac{2\ell-1}{2\ell} \right)}{(2\ell - 5/3) (2\ell)!} \right\} \quad (\text{A-37})$$

The integrals over  $r$  are easily expressed in terms of the beta function  $B(x,y)$  by means of

$$\int_0^1 v^n \left[ \cos^{-1} v - v \sqrt{1-v^2} \right] dv = \frac{1}{2} \left[ \frac{1}{n+1} - \frac{1}{n+3} \right] B\left(\frac{n+2}{2}, \frac{1}{2}\right) \quad (\text{A-38})$$

The result is

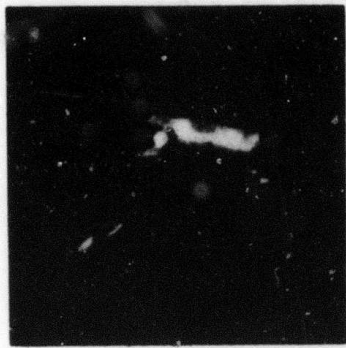
$$I_{\infty} = \frac{3}{20} k_o^{-5/3} - \frac{3888}{4675} \left[ \frac{\Gamma(7/6)}{\Gamma(5/6)} \frac{B(7/3, 1/2)}{\pi} \right] - \text{other terms} \quad (\text{A-39})$$

The other terms in Equation (A-39) vanish when  $K_o$  is zero, and the constant is

$$\frac{3888}{4675} \left[ \frac{\Gamma(7,6)}{\Gamma(5/6)} \frac{B(7/3, 1/2)}{\pi} \right] = \frac{0.5324}{2}$$

APPENDIX B

SIMULATION STUDY IMAGES



60 in.

015



48 in.

019



32 in.

021



24 in.

023



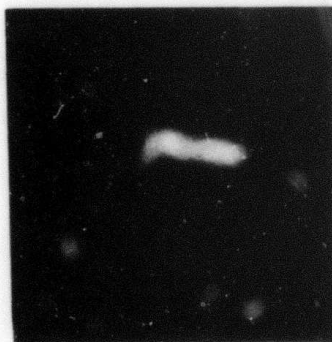
16 in.

025



12 in.

027



8 in.

029



6 in.


030



4 in.

031

Figure B-1. Reference Set Image Examples

Reproduced from  
best available copy. 



48 in.

059



48 in.

060



48 in.

061



32 in.

062



32 in.

063



32 in.

064



16 in.

065



16 in.

066



16 in.

067

Figure B-2. Poisson Noise with Various Diffraction-Limited Apertures (Set B)



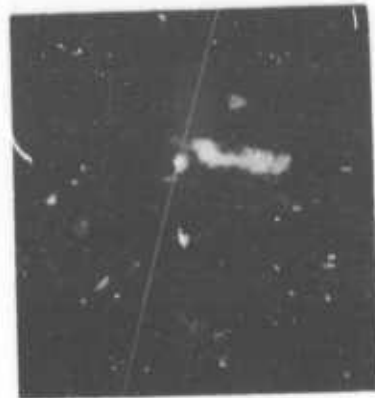
48 in.

117



48 in.

118



48 in.

119



32 in.

120



32 in.

121



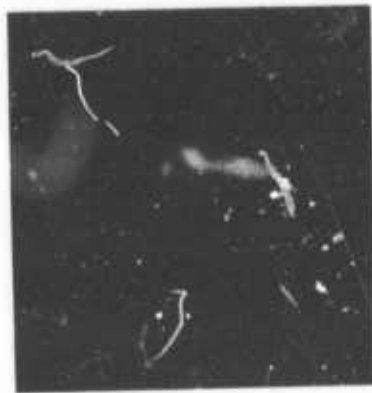
32 in.

122



16 in.

123



16 in.

124



16 in.

125

Figure B-3. Gaussian Noise with Various Diffraction-Limited Apertures (Set H)



071



049



050



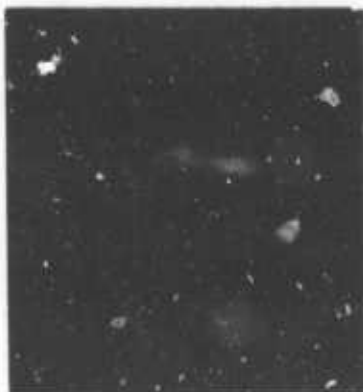
070



045



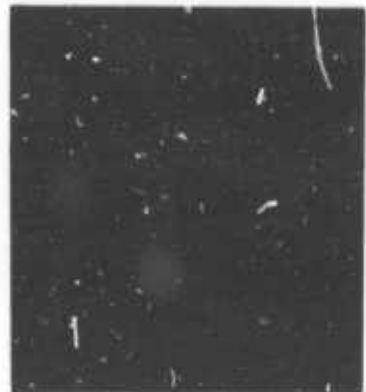
046



069



041



042

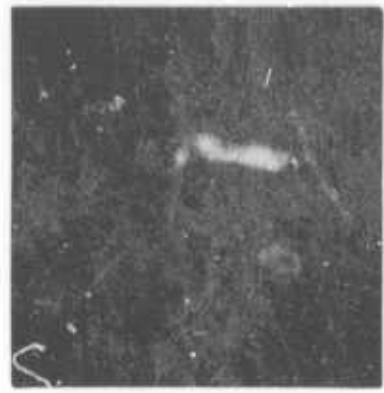
Figure B-4. Short Time Exposure OTF and Poisson Noise (Set C)



126



127



128



129



130



131



132



133



134

Figure B-5. Short Time Exposure OTF and Gaussian Noise (Set I)





098



097



096



101



100



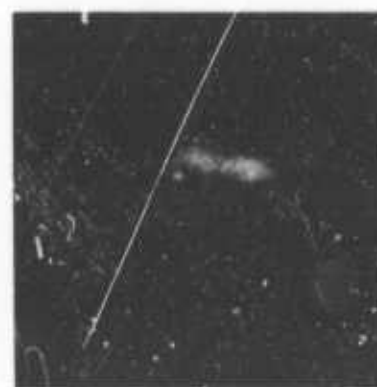
099



104



103



102

Figure B-6. Long Time Exposure OTF and Poisson Noise (Set F)



076



081



082



073



079



080



072



077



078

Figure B-7. Short Time Exposure OTF and Poisson Noise and Post-Processing (Exact) (Set D)



144



145



146



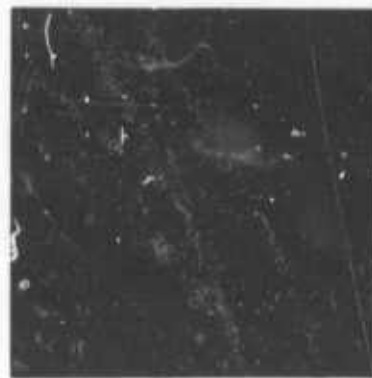
147



148



149



150



151

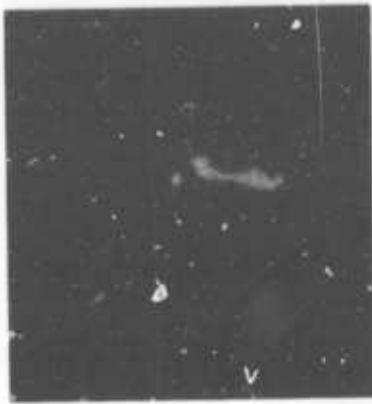


152

Figure B-8. Short Time Exposure OTF and Gaussian Noise and Post-Processing (Exact) (Set K)



107



106



105



110

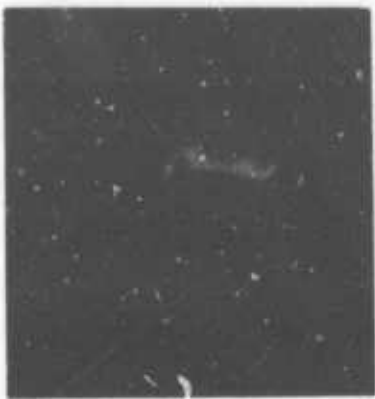


109

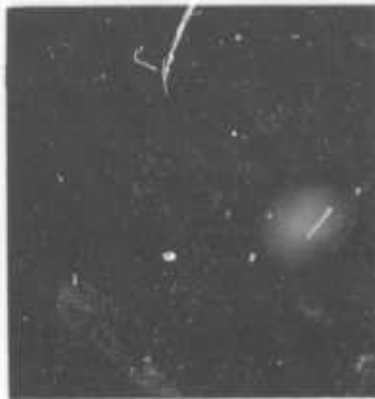


108

Figure B-9. Long Time Exposure OTF and Poisson Noise and Post-Processing (Exact) (Set G)



135



138



141



136



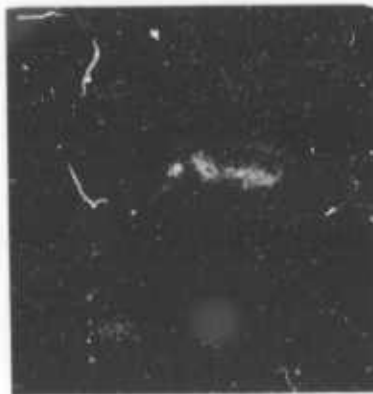
139



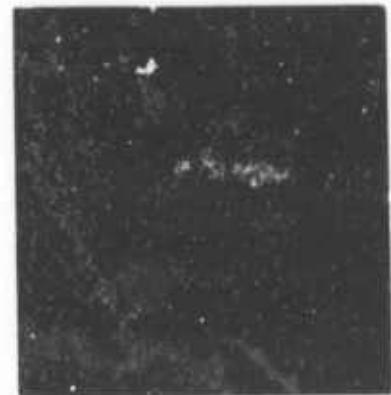
142



137

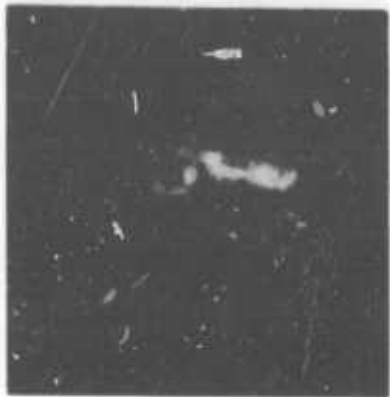


140

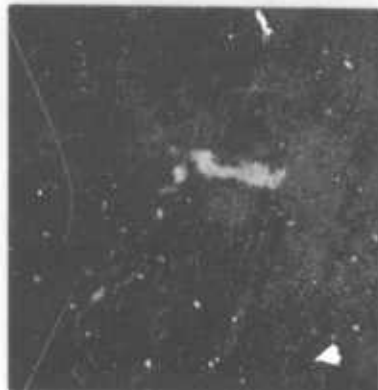


143

Figure B-10. Short Time Exposure OTF and Poisson Noise and Post-Processing (Approximate) (Set J)



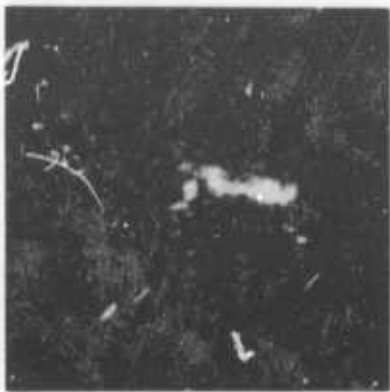
161



160



159



155



154



153



167



166



165

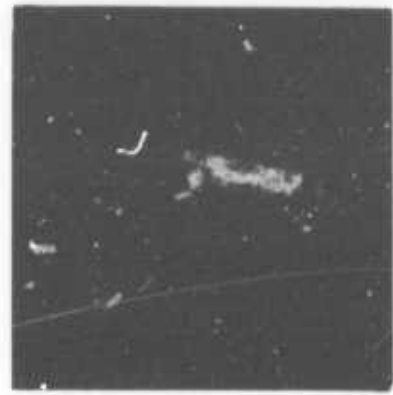
Figure B-11 Long Time Exposure OTF and Poisson Noise and Wiener Filter Restoration (SET L).



164



163



162



158



157



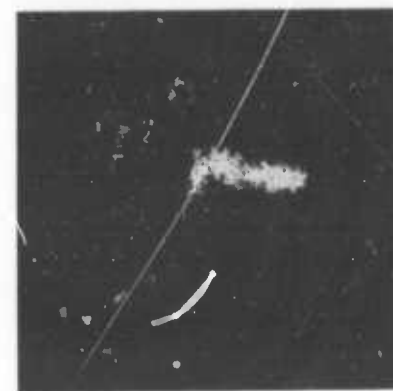
156



170



169



168

Reproduced from  
best available copy.



Figure B-12 Long Time Exposure OTF and Poisson Noise and Geometric Mean Filter Restoration (SET M).

APPENDIX C

SET BY SET SUMMARY OF RESULTS  
OF FITTING SIMPLE MODEL TO SIMULATION  
STUDY IMAGES

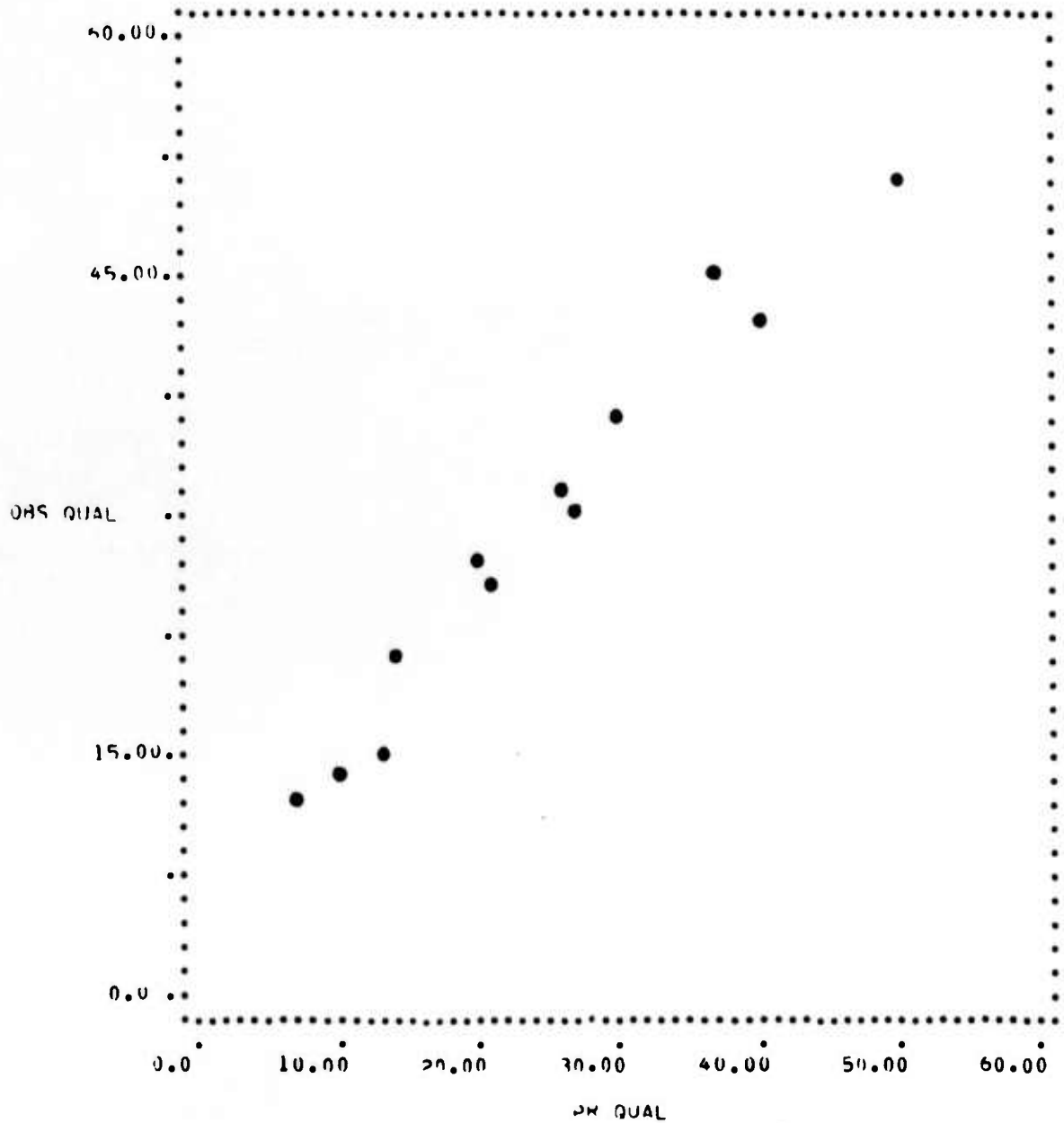


\*\*\* VANDID PROGRAM 11:43:11 05/21/75 \*\*\*

SET R DIFF LIM + POISSON NOISE

P-HAT = SIG\*SNR INPUT ALPHA = 1800. AVERAGE ALPHA = 554.

RMS QUAL ERROR = 4.9



\*\*\* VANDI> PROGRAM 11:45:56 05/21/75 \*\*\*

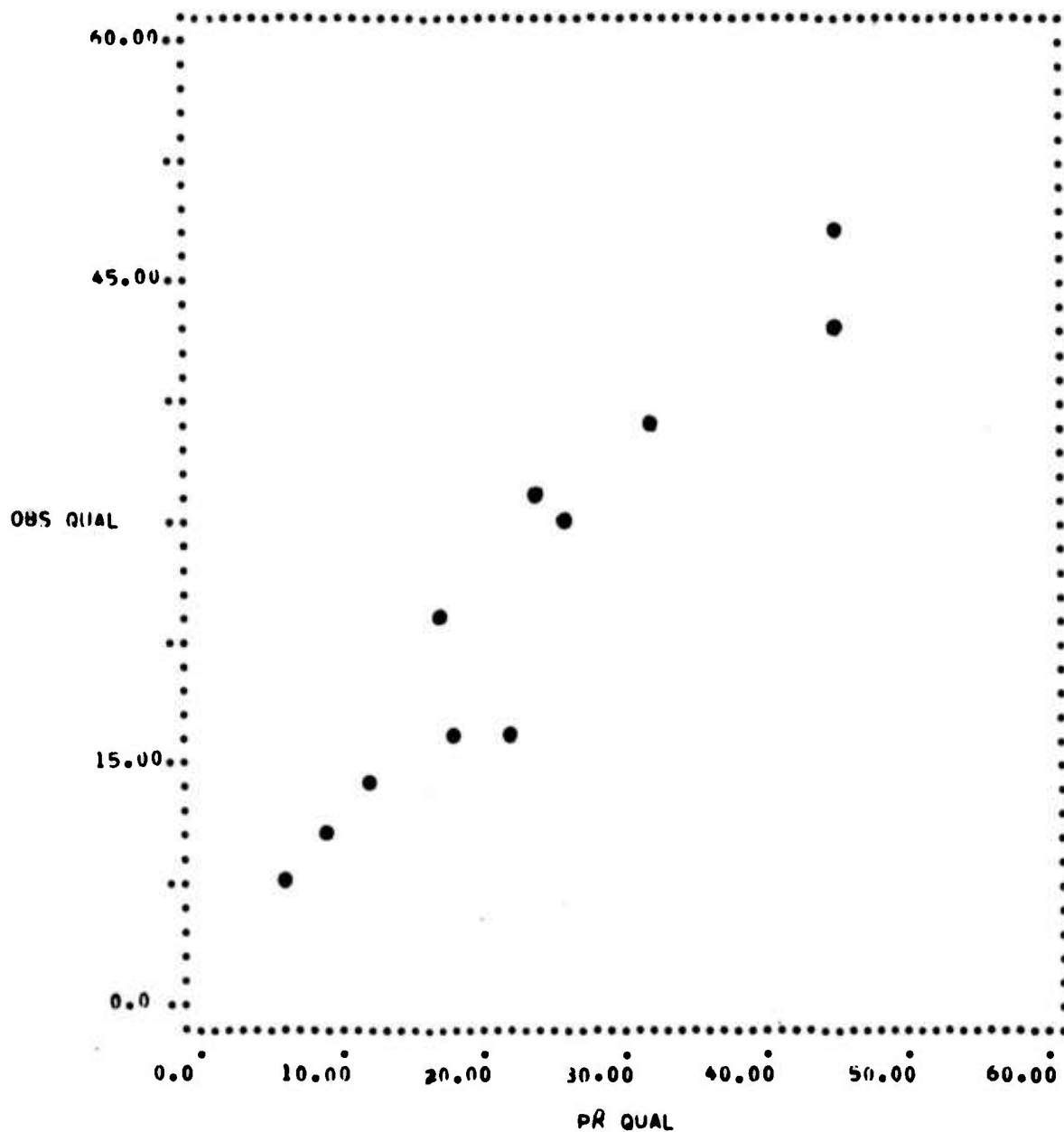
SET M DIFF LIM \* GAUSSIAN NOISE

P-MAT = SIG\*GNI

INPUT ALPHA = 3400.

AVERAGE ALPHA = 2696.

RMS QUAL ERROR = 3.9

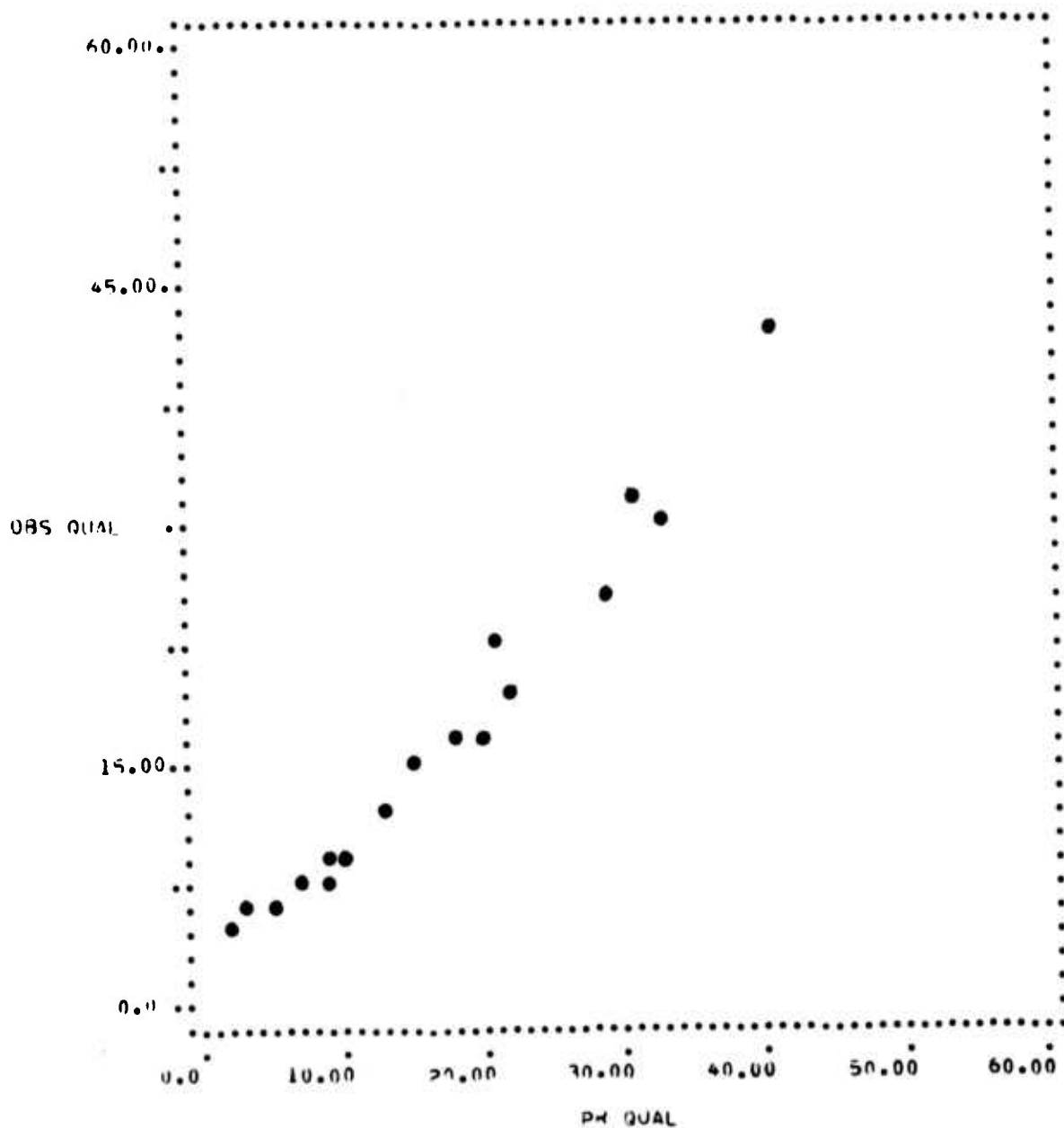


\*\*\* VANDI2 PROGRAM 11:44:16 05/21/75 \*\*\*

SET C SHORT T- OTE + POISSON NOISE

P-HAT = SIG\*GNI INPUT ALPHA = 1400. AVERAGE ALPHA = 3290.

RMS QUAL ERROR = 2.1



\*\*\* VANDI? PROGRAM 11:46:19 05/21/75 \*\*\*

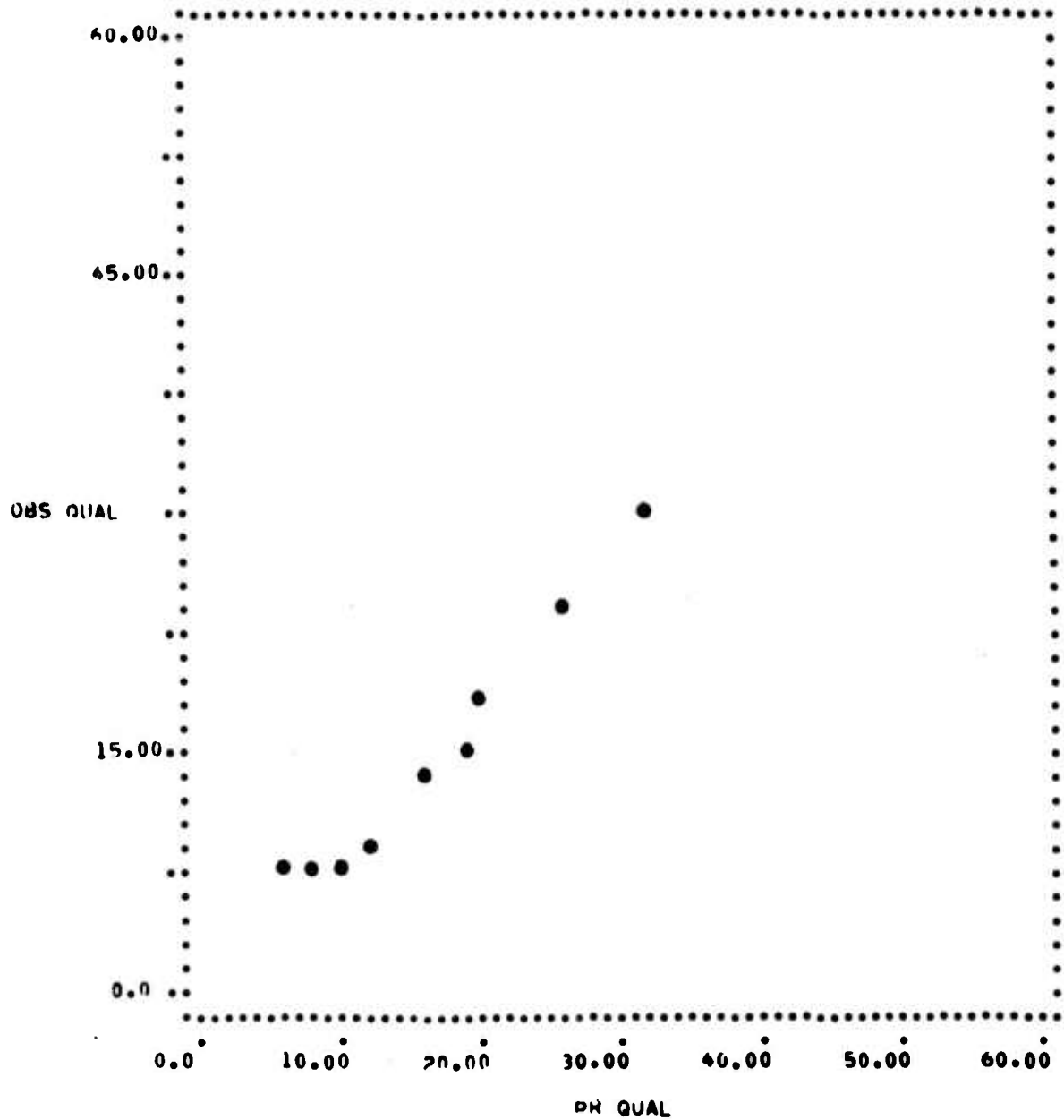
SET I SHORT TF OTF + GAUSSIAN NOISE

P-HAT = SIG\*GNI

INPUT ALPHA = 3400.

AVERAGE ALPHA = 7550.

RMS QUAL ERROR = 2.0



\*\*\* VANDIP PROGRAM 11:45:12 05/21/75 \*\*\*

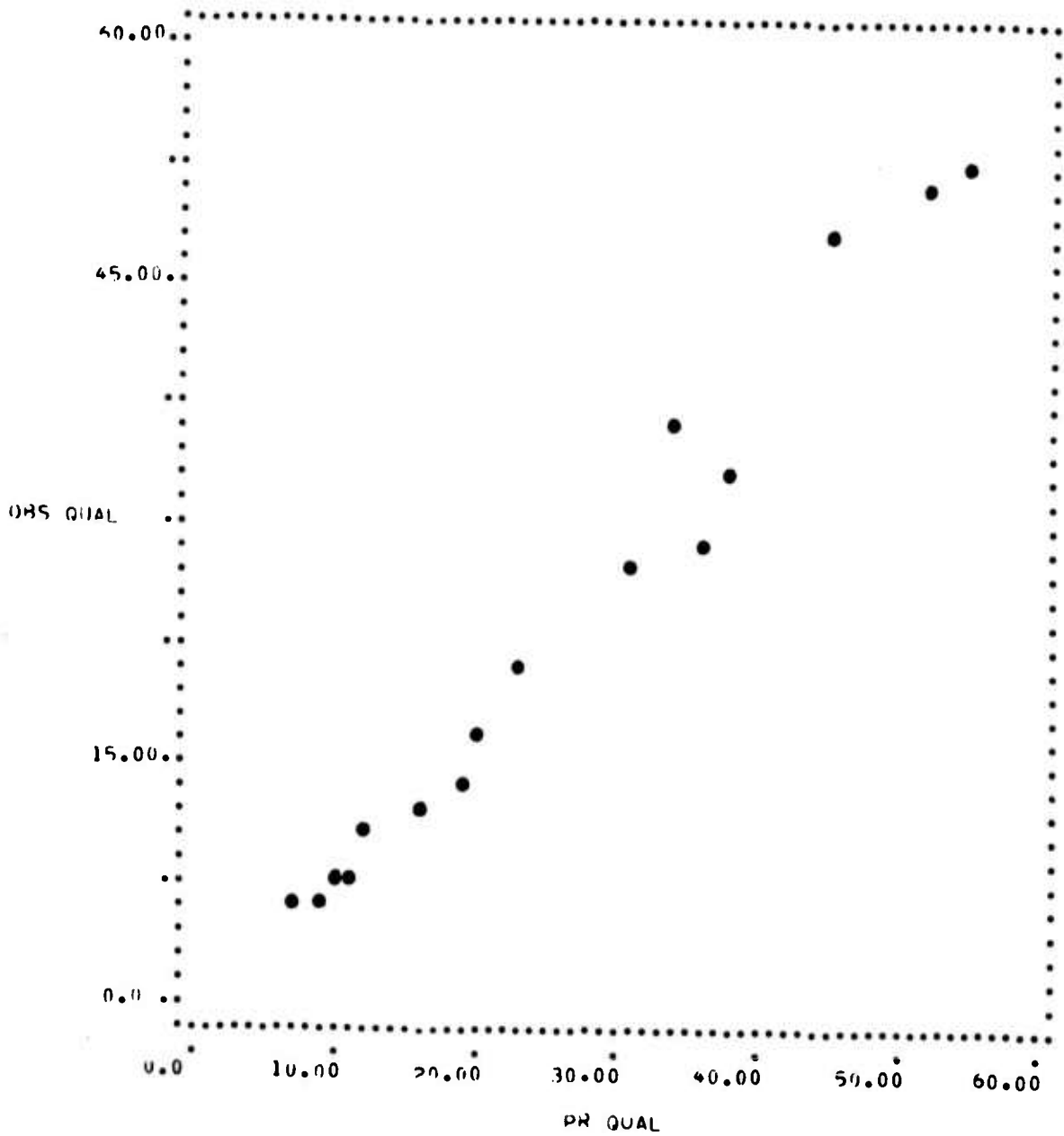
SET F LONG TF OTF + POISSON NOISE

P-HAT = SIG\*GNI

INPUT ALPHA = 1800.

AVERAGE ALPHA = 9103.

RMS QUAL ERROR = 3.5



\*\*\* VANDIP PROGRAM 11:44:51 05/21/75 \*\*\*

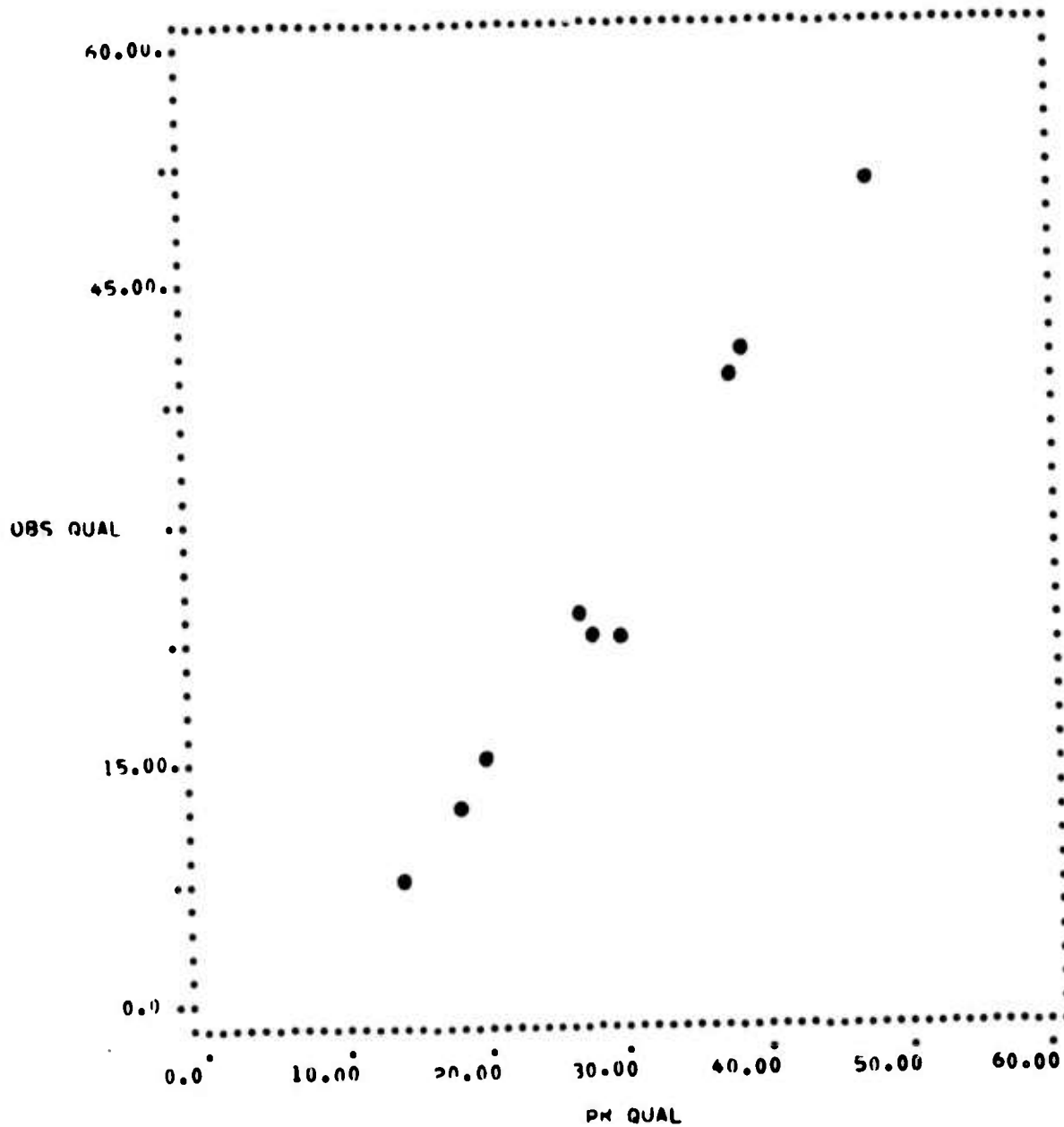
SET D SHORT TE OTF \* P. \* POST PROC (EXACT)

P-HAT = SIG\*IGNI

INPUT ALPHA = 1800.

AVERAGE ALPHA = 5189.

RMS QUAL ERROR = 4.6



\*\*\* VANDI> PROGRAM 11:47:04 05/21/75 \*\*\*

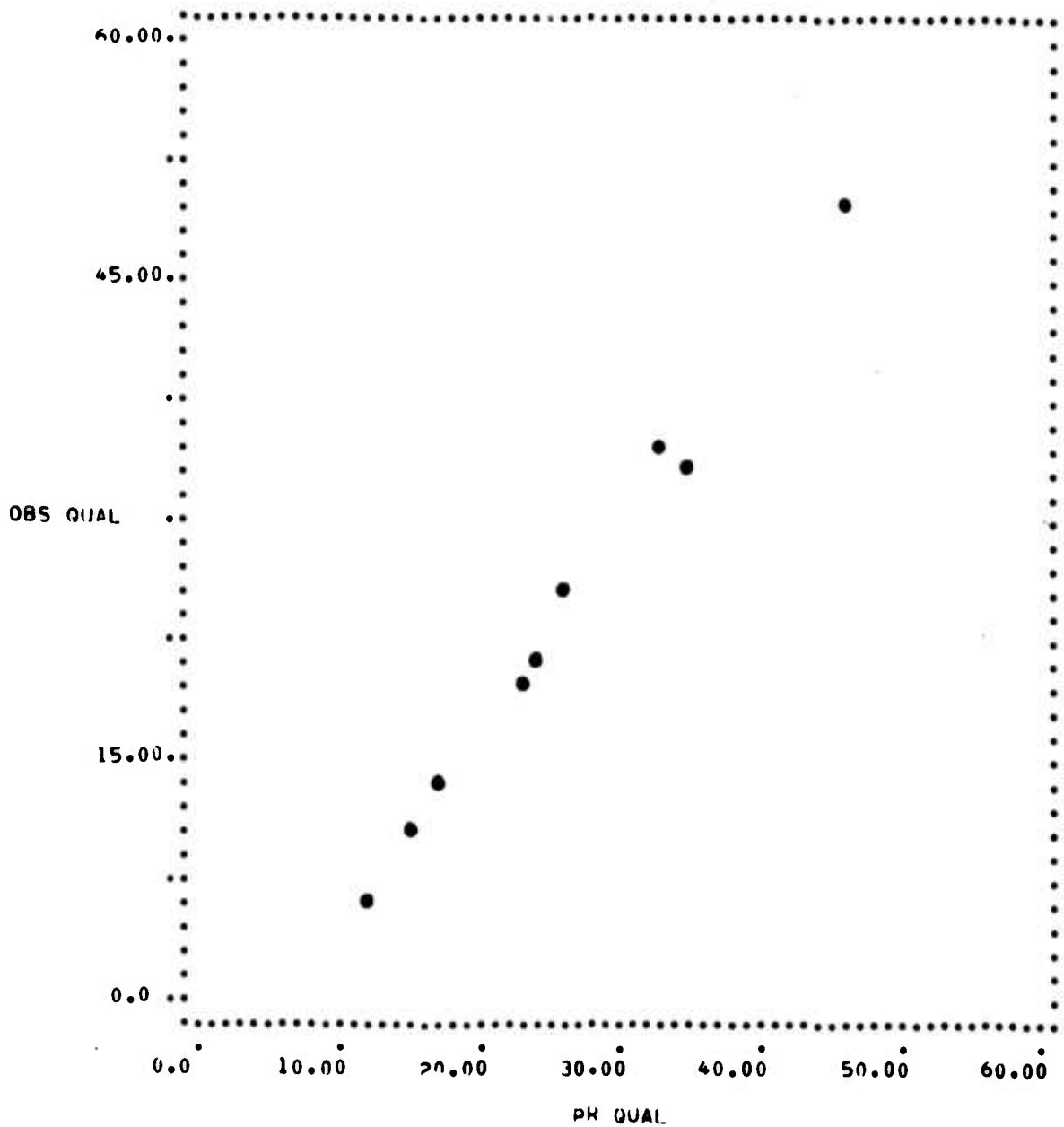
SET K SHORT TE OTF + G.N. +POST PROC (EXACT)

P-HAT = SIG\*GNI

INPUT ALPHA = 3400.

AVERAGE ALPHA = 9865.

RM: QUAL ERROR = 3.5



\*\*\* VANDI? PROGRAM 11:45:34 05/21/75 \*\*\*

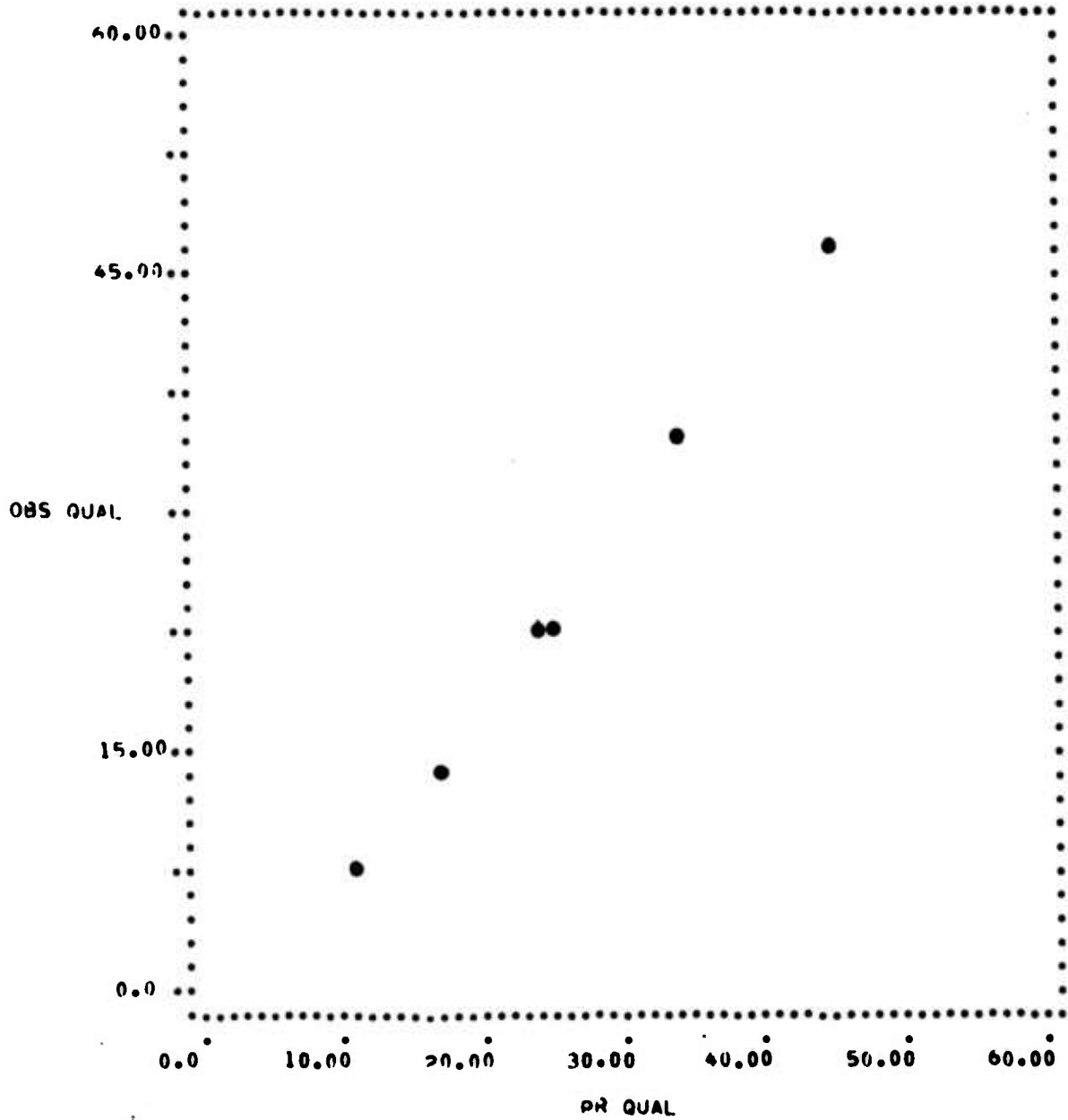
SFT 6 LONG TE UTF \* P.N. \* POST PROC (EXACT)

P-HAT = SIG\*GHI

INPUT ALPHA = 1000.

AVERAGE ALPHA = 4082.

RMS QUAL ERROR = 2.6





\*\*\* VANDI> PROGRAM 11:43:11 05/21/75 \*\*\*

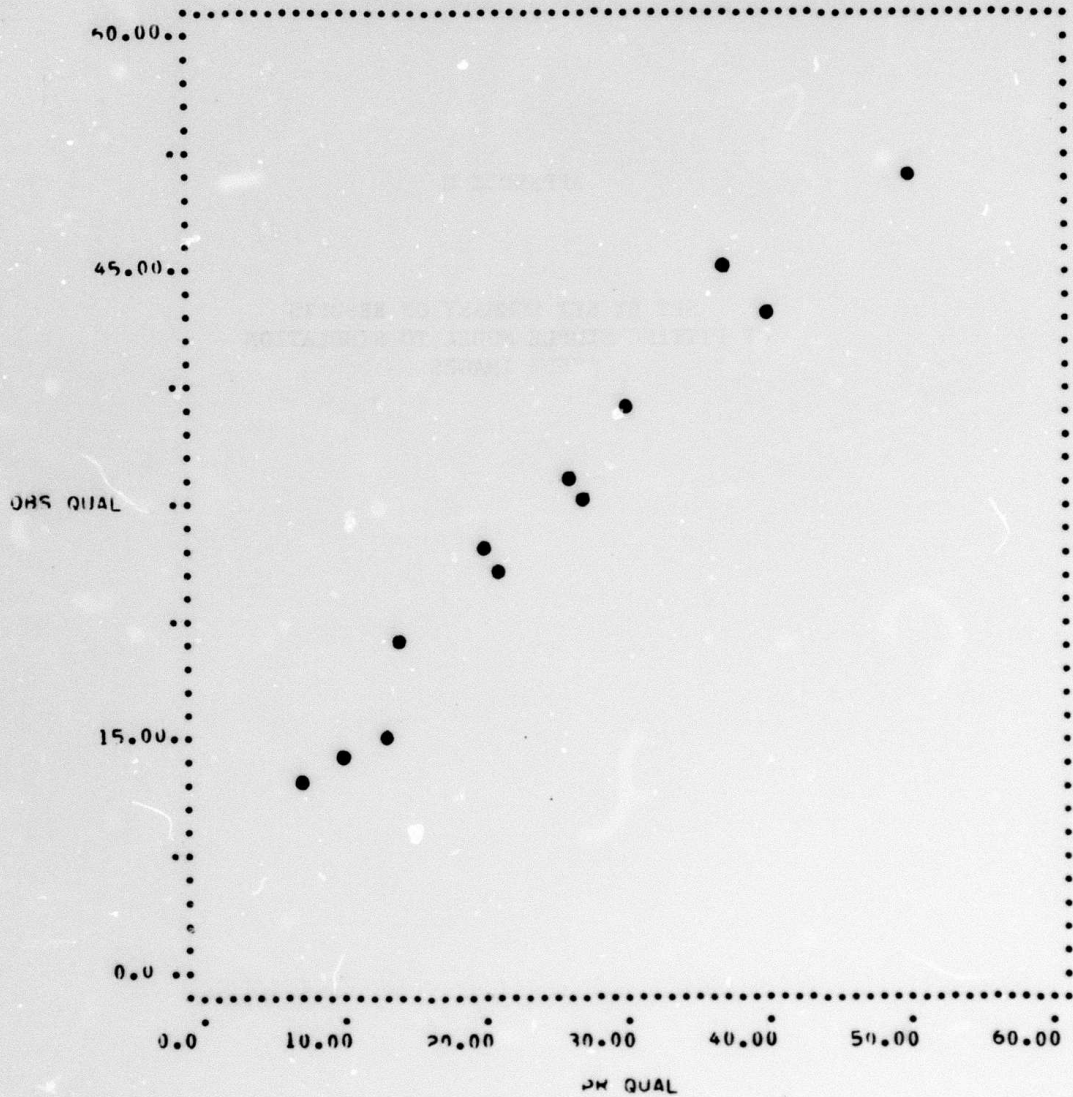
SET 9 DIFF LIM + POISSON NOISE

P-HAT = SIG\*5NI

INPUT ALPHA = 1800.

AVERAGE ALPHA = 654.

RMS QUAL ERROR = 4.9

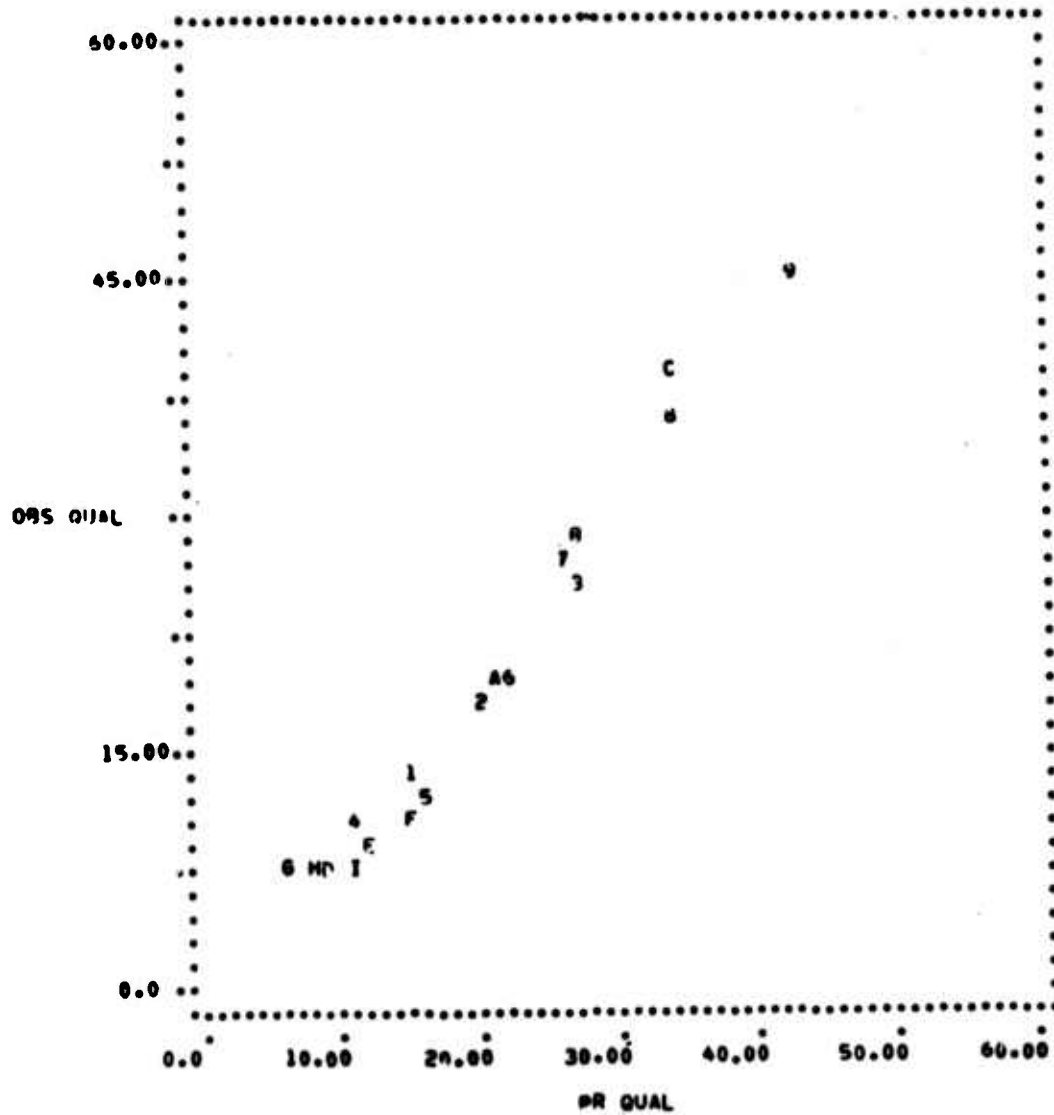


\*\*\* VAND12 PROGRAM 15:55:00 06/18/75 \*\*\*

SET L WIENER AND GEOMETRIC MEAN FILTERED POISSON NOISE

P-MAT = SIG\*GNI INPUT ALPHA = 1000. AVERAGE ALPHA = 3355.

RMS QUAL ERROR = 2.5



APPENDIX D

EYE TRANSFER FUNCTION

The eye modulation transfer function used in the full summary measure model is an analytical approximation of published data<sup>1,2</sup> given by

$$T_{\text{eye}}(k) = \frac{1 + 0.8 k}{1 + 0.025 k^4}$$

where  $k$  = spatial frequency (cy/mm)

Figure D-1 illustrates this function.

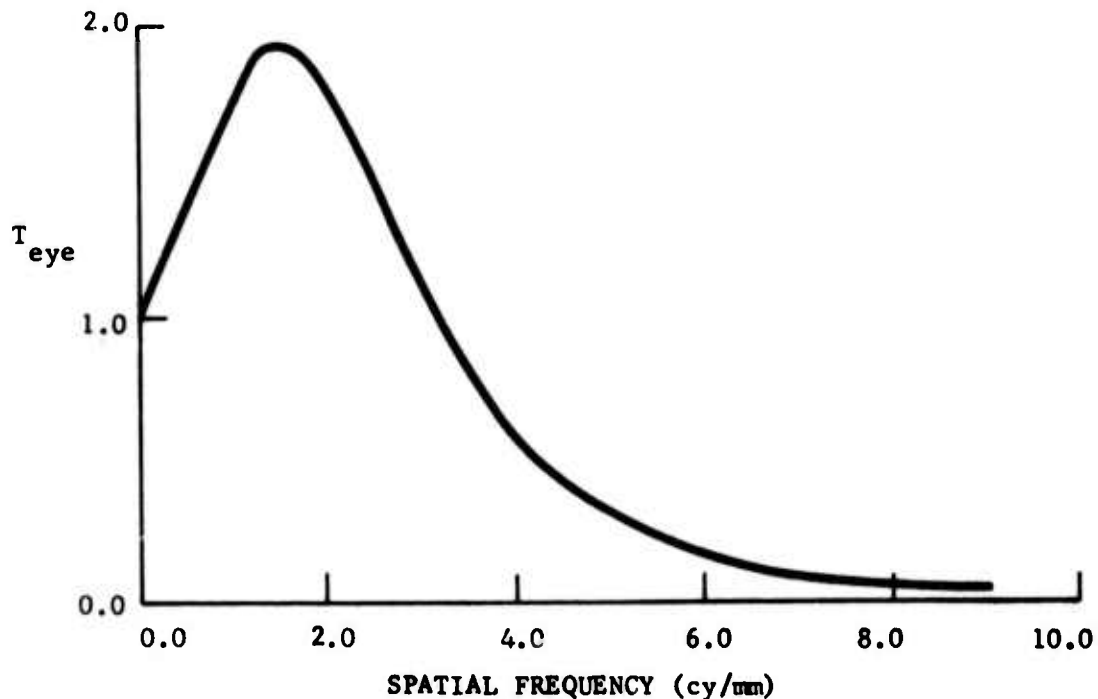


Figure D-1. Eye Transfer Function

1 - O. Bryngdahl, *Optika Acta*, 12, Jan. 65

2 - J.J. DePalma, E.M. Lowry, *JOSA*, 52, Mar. 62, p 328

APPENDIX E

ESTIMATIVE FILTER RESULTS

An important consideration is the application of the Summary Image Quality (SIQ) model to generalized restoration filters. In order to qualify the performance of the SIQ model two generalized filters were used to restore long time exposure images. These two filters were the Wiener and Geometric Mean filter.

The Wiener filter is the best generalized filter in a mean-square-error sense.<sup>1</sup> This filter takes the form:

$$F(k) = \frac{T_{le}^*(k)}{|T_{le}(k)|^2 + \phi_n(k)/\phi_o(k)} \quad E-1$$

where

$\phi_n(k)$  is the estimate of the noise power spectrum

$\phi_o(k)$  is the estimate of the object power spectrum.

The Geometric Mean filter is a geometrical mean between the inverse filter and the Wiener filter. This filter as suggested by Stockham, Cole,<sup>2</sup> and Cannor<sup>3</sup> is, in its general form:

$$F(k) = \left[ \frac{1}{T_{le}(k)} \right]^S \left[ \frac{T_{le}^*(k)}{|T_{le}(k)|^2 + \phi_n(k)/\phi_o(k)} \right]^{1-S} \quad E-2$$

<sup>1</sup>C. W. Helstrom, "Image Restoration by the Method of Least Squares," JOSA, Vol. 57, No. 3, pp 297-303, (Mar 1967).

<sup>2</sup>E. R. Cole, "The Removal of Unknown Image Blurs by Homomorphic Filtering," Ph. D. Dissertation, Dept. of E. E., Univ. of Utah, Salt Lake City, (Jun 1973).

<sup>3</sup>T. M. Cannor, "Digital Image Deblurring by Nonlinear Homomorphic Filtering," Ph. D. Dissertation, Dept. of E. E., Univ. of Utah, Salt Lake City, (Aug 1974).

where  $0 \leq S \leq 1$ . For the isotropic phaseless filter,  $H=H^*$  and  $S=1/2$ , equation E-2 reduces to:

$$F(k) = \left[ \frac{\phi_0(k)}{\phi_0(k) |T_{1e}(k)|^2 + \phi_n(k)} \right]^{1/2} \quad \text{E-3}$$

again for the long time exposure case. Figures E-1 and E-2 represent various degrees of wavefront error and noise variance for the Wiener and Geometric Mean cases respectively.

When the data from V and I experiments were reduced, agreement of the SIQ model to observed image quality was within 2.5 inches standard deviation.

$\epsilon = 1.20 \text{ rad}^2$	161	160	159
$\epsilon = 2.74 \text{ rad}^2$	155	154	153
$\epsilon = 4.36 \text{ rad}^2$	167	166	165
$\sigma_f =$	.0112	.025	.056

Figure E-1 SET L. Long Time Exposure Atmospheric OTF and Poisson Noise and Wiener Filter Restoration to Strehl Ratio = 0.8.



$\epsilon = 1.20 \text{ rad}^2$	164	163	162
$\epsilon = 2.74 \text{ rad}^2$	158	157	156
$\epsilon = 4.36 \text{ rad}^2$	170	169	168
$\sigma_f =$	.0112	.025	.054

Figure E-2 SET M. Long Time Exposure Atmospheric OTF and Poisson Noise and Geometric Mean Filter Restoration Strehl Ratio = 0.8.

## GLOSSARY

- a = photoelectrons per pixel per unit reflectivity
- $A_n$  = coefficient of nth Zernike polynomial
- c = dimensionless scale factor
- $C(r)$  = two-dimensional autocorrelation function of wavefront
- DQRF = dimensionless quality reduction factor
- $D_{mse}$  = mean square error image quality criterion
- $D_o$  = aperture diameter (inches or meters)
- $D(r)$  = phase structure function
- E = edge response
- $E_{max}$  = maximum value of filter function
- F = focal length (meters)
- $F_s(k)$  = approximate transfer function restoration filter
- $F_c$  = fidelity criterion
- $F_e(k)$  = exact transfer function restoration filter
- f = relative fidelity criterion
- $i(r)$  = image
- $J_1(2\pi Rk)$  = Bessel function
- $k = (k_x, k_y)$ , two-dimensional spatial frequency (cycles/millimeter)
- $\tilde{k}$  = normalized spatial frequency
- $k_{nyq}$  = Nyquist frequency
- $\lambda(x)$  = line spread function
- m = viewing magnification
- $m_{opt}$  = optimum viewing magnification
- M = pre-noise image modulation factor
- $M_D$  = post-noise image modulation factor

GLOSSARY (Continued)

- $n(x)$  = noise random variable  
 $N_I$  = additive Gaussian noise standard deviation increase factor  
 $N(k)$  = noise power spectral density  
 $NRE$  = normalized relative energy  
  
 $o(r)$  = object  
  
 $p$  = point spread function  
  
 $Q$  = image quality (inches)  
 $Q_{ioc}$  = image-object correlation criterion  
 $Q_o$  = image quality for no noise  
  
 $r$  = (u,v) two-dimensional coordinate on aperture plane (meters)  
 $r_o$  = coherence length  
 $r_s$  = reflectivity of satellite  
 $R$  = aperture radius (inches)  
  
 $S$  = Strehl ratio  
  
 $t$  = relative image sharpness  
 $t_e$  = exposure time  
 $T_D(k)$  = display transfer function  
 $T_{dl}(k)$  = desired diffraction-limited transfer function  
 $T_{eye}(k)$  = eye modulation transfer function  
 $T_{is}$  = image sharpness criterion  
 $T_{kn}(k)$  = known degrading transfer function  
 $T_{le}(k)$  = long time exposure atmospheric transfer function  
 $T_o(k)$  = diffraction-limited transfer function  
 $T_{se}(k)$  = short time exposure atmospheric transfer function  
  
 $U_s(x)$  = value of sampled image point (pixel) (photoelectrons)  
  
 $W_\phi(k)$  = power spectrum of atmospheric turbulence ( $\text{rad}^2/(\text{cy}/\text{m})^2$ )

GLOSSARY (Continued)

$Z_n(u,v)$  = nth Zernike polynomial

$\alpha$  = noise scaling factor

$\beta$  = filter parameter

$\epsilon$  = mean square wavefront error (radian<sup>2</sup>)

$\eta$  = fidelity criterion parameter

$\theta_s$  = pixel angular subtense (radians)

$\lambda$  = wavelength (micrometers)

$\sigma_n$  = image noise (photoelectrons)

$\sigma_r$  = image noise (reflectivity)

$\bar{\sigma}_r$  = average image noise

$\phi(r)$  = wavefront phase (radians)

$\Phi(k)$  = object power spectrum

$\Omega_s$  = Nyquist angular sampling rate (samples/radian)

*MISSION*  
*of*  
*Rome Air Development Center*

*RADC is the principal AFSC organization charged with planning and executing the USAF exploratory and advanced development programs for information sciences, intelligence, command, control and communications technology, products and services oriented to the needs of the USAF. Primary RADC mission areas are communications, electromagnetic guidance and control, surveillance of ground and aerospace objects, intelligence data collection and handling, information system technology, and electronic reliability, maintainability and compatibility. RADC has mission responsibility as assigned by AFSC for demonstration and acquisition of selected subsystems and systems in the intelligence, mapping, charting, command, control and communications areas.*